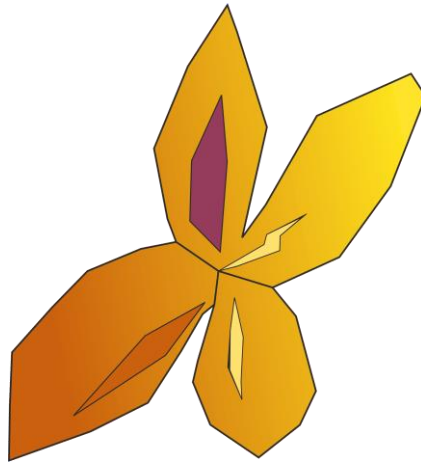


Structure, Formation and Transformation of the Mineral Struvite

A geochemical and mineralogical study with
environmental applications



Dissertation

zur Erlangung des Grades eines Doktors der Naturwissenschaften

Doctor rerum naturalium (Dr. rer. nat.)

am Fachbereich Geowissenschaften

der Freien Universität Berlin

vorgelegt von

Rebecca Volkmann

Berlin, August 2024

First reviewer (Erstgutachterin):

Prof. Dr. Liane G. Benning

Department of Earth Sciences, Freie Universität Berlin

Interface Geochemistry Section, German Research Centre for Geosciences (GFZ) Potsdam

Second reviewer (Zweitgutachter):

Prof. Dr. Max Wilke

Institute of Geosciences, Universität Potsdam

Date of disputation:

29.11.2024

This work was conducted from October 2020 to March 2024 at the German Research Centre for Geosciences (GFZ) Potsdam under the supervision of Prof. Dr. Liane G. Benning. This work was supported by grants from the International Union of Crystallography (IUCr), The European Crystallographic Association (ECA), the Cambridge Crystallographic Data Centre (CCDC) as well as the German Mineralogical Society (DMG).

Eigenständigkeitserklärung

Hiermit versichere ich, dass ich die vorliegende Arbeit selbstständig verfasst und keine anderen als die angegebenen Quellen und Hilfsmittel benutzt habe; alle Ausführungen, die anderen Schriften wörtlich oder sinngemäß entnommen wurden, kenntlich gemacht sind und die Arbeit in gleicher oder ähnlicher Fassung noch nicht Bestandteil einer Studien- oder Prüfungsleistung war.

Berlin, August 2024

Rebecca Volkmann

Declaration

This dissertation is a cumulative work of peer-reviewed scientific papers, either published, submitted for publication or in the final stages of preparation for submission. The candidate confirms that the work submitted is her own. The contribution of the candidate and the other authors to this thesis have been explicitly indicated below. The candidate confirms that appropriate credit has been given within the thesis where reference has been made to the work of others. This dissertation is based on the following papers:

Chapter 1 reproduces a manuscript in preparation for submission to *European Journal of Mineralogy*.

Volkman, R.; Blukis, R.; Benning, L.G. (2024). The temperature-dependence of nucleation and growth kinetics of the Mg phosphate mineral struvite.

RV conceived and designed the study with the help of LGB. RV conducted the synthesis experiments and collected the pH and turbidity data with training by RB. RV conducted SEM imaging. RV and LGB collected the wide-angle X-ray scattering (WAXS) data. RV processed and interpreted the data with the help of RB. The manuscript was written by RV with contributions from all authors.

Chapter 2 reproduces a manuscript published as a preprint on *EarthArXiv*. The corresponding crystallographic information file (CIF) has been published by *GFZ Data Services* as well as *The Cambridge Crystallographic Database* as a data publication.

Volkman, R.; Münchhalfen, M.; Benning, L.G. (2024). A new structure determination of the magnesium phosphate mineral struvite ($\text{MgNH}_4\text{PO}_4 \cdot 6\text{H}_2\text{O}$) at 100 K.

DOI preprint: <https://doi.org/10.31223/X5KQ4F>

DOI data publication: <https://doi.org/10.5880/GFZ.3.5.2024.001>

RV collected the single crystal-diffraction data and conducted the refinement of the data. RV and MH described and interpreted the structural data. RV formatted the manuscript and the CIF file with contributions from all authors.

Chapter 3 reproduces a manuscript submitted to *American Mineralogist*.

Volkman, R.; Blukis, R.; Schmidt, C.; Forjanes, P.; Benning, L.G. (2024). The transformation of magnesium phosphate minerals at atmospheric conditions – A kinetic and mineralogical study with environmental applications.

RV conceived and designed the study with the help of LGB. RV conducted the synthesis and transformation experiments. XRD analyses and data refinements were conducted by RV under the supervision of RB. RV conducted SEM imaging. CS conducted Raman spectroscopy measurements. RV processed and interpreted the XRD data with the help of RB and interpreted the Raman data with the help of CS. RV collected and interpreted the infrared spectroscopy data with the help of PF. Microscopical images and kinetics were interpreted by RV with the help of RB, PF and LGB. The manuscript was prepared by RV with contributions from all authors.

Acknowledgements

Writing a doctoral thesis would not have been possible without supervision and training. My gratitude goes to my first supervisor, Prof. Dr. Liane G. Benning, and my co-supervisors, Dr. Roberts Blukis and Dr. Pablo Forjanés. But this work was not only supported by my official supervisors, but also by many people of the Interface Geochemistry working group at the German Research Centre for Geosciences (GFZ) Potsdam. I want to thank Dr. Jeffrey Perez and Dr. Thaïs Couasnon, who supported me with scientific advice even without being my official supervisors. Also, thanks to all the other members of the group who became my colleagues and friends – Alice Paskin, Elisa Peter, Marc Paje, Marco Ajmar, Rey Mourot, Ruth Delina, Sven Peters – and all the others that I cannot mention here (because the group is too big) - for their mental support.

I received further help to dive into the scientific field of Rietveld analyses from scientists from the GFZ Potsdam, by Prof. Dr. Matthias Gottschalk, as well as from my old place of study, the Ruhr-University Bochum, by Dr. Bernd Marler. I would also like to thank Prof. Dr. Sumit Chakraborty for his input on kinetic theories, as well as Prof. Dr. Jürgen Schreuer (Ruhr-University Bochum) and Dr. Farzaneh Tirani from the École Polytechnique Fédérale de Lausanne, for their support with the crystal structure solution. Furthermore, I would like to say that there are very kind people at the GFZ Potsdam as well as the University of Potsdam, e.g., Dr. Hans-Peter Nabein, Dr. Sergio Speziale, and Prof. Dr. Max Wilke, who supported me with other scientific problems. Last, my thanks go to Dr. Thomas Hartmann, who often rescued us when we had problems with the X-ray diffractometer maintenance.

Thank you to my loved ones, my family, my parents, my partner Constantin, and my closest friends, Christopher, Janina, Jannis, and Marcel, for your mental support, for listening to all my complaints and struggles, and for playing board games with me.

Kurzfassung

Das Magnesiumphosphat-Mineral Struvit ($\text{MgNH}_4\text{PO}_4 \cdot 6\text{H}_2\text{O}$) hat im Bereich der Rückgewinnung von Phosphor (P) und Stickstoff (N) aus Abwässern wissenschaftliche Bedeutung erlangt. Die Rückgewinnung dieser Elemente ist nicht nur wegen der begrenzten Verfügbarkeit natürlicher P-Ressourcen, wie z.B. von Phosphoriten, von entscheidender Bedeutung, sondern auch als Mittel zur Verringerung der mit dem Abbau solcher Vorkommen verbundenen Umweltschäden. Darüber hinaus wird der zurückgewonnene Struvit als Langzeitdünger in der Landwirtschaft eingesetzt.

Düngemittel aus Struvit aus Abwässern werden durch gezielte Ausfällung in Kläranlagen gewonnen. Um diesen Prozess möglichst effizient zu gestalten, ist es von grundlegender Bedeutung, die erforderlichen Bedingungen für die Bildung von Struvit genau zu verstehen. Dazu gehören nicht nur die Ausfällungsbedingungen von Struvit, sondern auch die Kinetik von Keimbildung und Wachstum. Während die Bildungsbedingungen von Struvit in Abwässern weitgehend untersucht worden sind, besteht noch eine erhebliche Wissenslücke hinsichtlich der Bildung von Struvit aus reinen Salzlösungen sowie der kinetischen Parameter von Keimbildung und Wachstum. Die Mechanismen der Struvitkeimbildung und des Struvitwachstums sowie die Rolle der Temperatur für die Bildung von Struvit sind nach wie vor kaum bekannt. Ein besseres Verständnis dieser Parameter ist von entscheidender Bedeutung für die Vorhersage der Struvit ausfällung aus komplexen Lösungen, wie sie in Abwässern vorkommen. Mein erstes Ziel für diese Arbeit war daher die Untersuchung der Keimbildungs- und der Wachstumskinetik von Struvit aus reinen Salzlösungen bei verschiedenen Temperaturen.

Die Verwendung von Struvitdünger wird dadurch eingeschränkt, dass Struvit unter Atmosphärenbedingungen nicht stabil ist. Die genauen Bedingungen, die den Zerfall von Struvit auslösen, sind nicht vollständig geklärt, was seine breite Verwendung als Düngemittel einschränkt. Der sichere Transport und die Lagerung von Struvitdünger für die spätere industrielle Verwendung erfordert ein vollständiges Verständnis der Bedingungen, unter denen sich Struvit in sekundäre Phasen umwandelt. Demzufolge war das zweite Ziel meiner Arbeit, die Umwandlung von Struvit an der Luft in Abhängigkeit von der Temperatur zu untersuchen.

Um diesen Fragen nachzugehen, habe ich einen experimentellen Ansatz mit synthetischen Struvitlösungen und -kristallen gewählt. Zur Bestimmung der kinetischen Parameter für die Struvitbildung führte ich Keimbildungs- und Wachstumsexperimente bei verschiedenen Lösungskonzentrationen und -temperaturen durch und setzte dabei *in-situ* Spektroskopie und Röntgenbeugungsmethoden (RDA) ein. Für ein besseres Verständnis der Stabilität von Struvit verwendete ich Einkristall-Röntgenbeugung und löste die Kristallstruktur von Struvit bei niedrigen Temperaturen (100 K), wodurch die Atombindungen geringer durch die Temperatur beeinflusst

werden, und die Struktur genauer beschrieben werden kann. Außerdem untersuchte ich die Bedingungen und den Mechanismus des Zerfalls von Struvit in sekundäre Phasen durch Umwandlungsexperimente an der Luft bei verschiedenen Temperaturen. Mit Hilfe von RDA, Infrarot-(IR) und Raman-Spektroskopie sowie Rasterelektronenmikroskopie (REM) bestimmte ich die kinetischen Parameter des Zerfalls und charakterisierte die entstehenden Produkte, um die Mechanismen der Struvit-Umwandlung zu verstehen.

Die Untersuchung der Keimbildungs- und Wachstumskinetik von Struvit in Abhängigkeit von der Temperatur ergab eine Reaktionsordnung (n) von ~ 0.4 – 0.8 , was auf einen diffusionsdominierten Keimbildungsmechanismus hindeutet, und Geschwindigkeitskonstanten (k) von ~ 0.3 – 0.8 s^{-1} , ohne signifikante Änderungen bei den unterschiedlichen Temperaturen. Die Aktivierungsenergie für die Kristallisation wurde mit $\sim 17 \text{ kJ/mol}$ berechnet. Die Induktionszeit der Struvit-Keimbildung nahm jedoch bis zu einer Temperatur von 25 °C ab und stieg über diese Temperatur hinaus wieder an, was frühere Annahmen über die umgekehrte Temperaturabhängigkeit der Struvit-Löslichkeit unterstützt.

Die verbesserte Kristallstruktur von Struvit zeigte, dass Ammoniak (NH_3) eine Schlüsselrolle für die Stabilität spielt. Bei niedrigen Temperaturen wird NH_3 in der Struvitstruktur als Ammoniumion (NH_4^+) festgehalten, welches durch drei Wasserstoff- (H-) brückenbindungen mit Phosphatanionen (PO_4^{3-}) und Magnesiumkationen (Mg^{2+}) stabilisiert wird. Diese Konfiguration ist entscheidend für die strukturelle Stabilität von Struvit bei niedrigen Temperaturen. Im Gegensatz dazu bildet NH_4^+ bei Raumtemperatur weniger Wasserstoffbrücken und zeigt Rotationsverhalten, was die Struvitstruktur weniger stabil macht.

Außerdem war ich in der Lage, die kinetischen Parameter für den Zerfall und die Umwandlung von Struvit in Abhängigkeit von der Temperatur experimentell zu bestimmen. Struvit wandelte sich, abhängig von der Reaktionstemperatur, in zwei verschiedene Minerale um: Newberyit ($\text{MgHPO}_4 \cdot 3\text{H}_2\text{O}$) und Dittmarit ($\text{MgNH}_4\text{PO}_4 \cdot \text{H}_2\text{O}$), sowie eine amorphe Phase. Die Umwandlungsreaktionen weisen ähnliche Reaktionsordnungen n von ~ 0.5 und Geschwindigkeitskonstanten k von ~ 0.5 – $8.1 \cdot 10^{-4} \text{ s}^{-1}$ für die Reaktion zu Newberyit und $2.9 \cdot 10^{-3} \text{ s}^{-1}$ für die Reaktion zu Dittmarit auf, was auf einen diffusionsdominierten Umwandlungsmechanismus hindeutet. Ein diffusionsdominierter Mechanismus wurde hier als Transport von NH_3 und Wasser (H_2O) aus der Struvitstruktur heraus interpretiert. Ergänzende REM und Raman-Spektroskopie ergaben, dass die anschließende Keimbildung und das Wachstum der neuen Phasen über eine gekoppelte Lösungs-Fällungsreaktion erfolgt.

Zusammenfassend konnte ich mit meiner Arbeit neue Kenntnisse zur Keimbildungs- und Wachstumskinetik von Struvit aus wässriger Lösung liefern, sowie neue Informationen über den Zerfall und die Umwandlung dieses Minerals. In meiner Arbeit stellte sich die Temperatur als wichtiger Faktor sowohl für die Bildung als auch für den Zerfall von Struvit heraus. Diese Ergebnisse tragen dazu bei,

Struvit-Fällungsprozesse in Kläranlagen zur P-Rückgewinnung zu verbessern. Darüber hinaus haben die neuen Erkenntnisse über die Zerfalls- und Umwandlungsparameter von Struvit an der Luft erhebliche Indikationen für die Lagerung und den Transport von Struvitdünger, da das Verständnis über den Umwandlungsprozess in sekundäre Phasen dazu beiträgt, die Eigenschaften und die Qualität des Düngers gewährleisten.

Abstract

The magnesium phosphate mineral struvite ($\text{MgNH}_4\text{PO}_4 \cdot 6\text{H}_2\text{O}$) has gained scientific significance in the field of phosphorous (P) and nitrogen (N) recovery from wastewater. The recovery of these elements has become critical due to the limited availability of natural P resources like phosphorites and as a tool to reduce the environmental harm linked to mining such deposits. Furthermore, recovered struvite is employed as a slow-release fertiliser for agriculture.

Fertilisers from wastewater-derived struvite are produced through intentional precipitation in wastewater treatment plants. However, it is fundamental to gain an in-depth understanding of the conditions necessary for the formation of struvite to maximise the efficiency of this process. This includes the formation conditions of struvite and the kinetics involved in its nucleation and growth. While the formation conditions of struvite-forming wastewater have been widely examined, a significant scientific knowledge gap still exists regarding the formation of struvite from pure salt solutions and the kinetic parameters of nucleation and growth. Aspects such as the nucleation and growth mechanisms of struvite and the role of temperature in the formation of struvite remain poorly understood. Better understanding these parameters is paramount to predicting struvite nucleation in complex solutions like the ones found in residual wastewater. As a result, my first aim for this study was to investigate the nucleation and growth kinetics of struvite from pure salt solutions at different temperatures.

The use of struvite fertiliser is limited by the fact that struvite is unstable under atmospheric conditions. The precise conditions that trigger the breakdown of struvite are not fully understood, which limits its widespread use as a fertiliser. The secure transport and storage of struvite for its later industrial use requires fully comprehending the conditions in which it transforms into secondary phases. This constitutes the second objective of my thesis, where I addressed the stability of struvite by looking at its crystal structure and the transformation of struvite in air as a function of temperature.

I used an experimental approach to address these knowledge gaps, including synthetic struvite solutions and crystals. To evaluate kinetic parameters governing the formation of struvite, I conducted nucleation and growth experiments at different solution concentrations and temperatures, employing in-situ spectroscopy and X-ray diffraction (XRD) techniques. To provide a more fundamental understanding of the stability of struvite, I used single-crystal X-ray diffraction and evaluated a more accurate crystal structure of struvite by analysis at low temperatures (100 K), providing less temperature-induced influence on the atomic bonds. Furthermore, I evaluated the conditions and the mechanism of struvite decomposition into secondary phases through dry transformation experiments at different temperatures. I used powder XRD, Infrared (IR) and Raman spectroscopy, and scanning electron

microscopy (SEM) to follow the decomposition kinetics and characterise the resulting products to elucidate the mechanisms of struvite decomposition.

The investigation of struvite nucleation and growth kinetics as a function of temperature revealed a reaction order (n) of ~ 0.4 – 0.8 , indicating a diffusion-controlled nucleation mechanism and rate constants (k) of ~ 0.3 – 0.8 s^{-1} . The activation energy of crystallisation was calculated as $\sim 17 \text{ kJ/mol}$. No significant changes in n and k values across temperatures were observed. However, the induction period of struvite nucleation decreased up to $25 \text{ }^\circ\text{C}$ and increased beyond this temperature, supporting previous assumptions about the reverse temperature-dependence of struvite solubility.

The improved crystal structure of struvite revealed that ammonia (NH_3) plays a key role in its stability. At low temperatures, NH_3 is retained within the structure of struvite as ammonium (NH_4^+), stabilised by three hydrogen (H) bonds connected to phosphate (PO_4^{3-}) anions and magnesium (Mg^{2+}) cations. This configuration is critical for the structural stability of struvite at low temperatures. In contrast, at room temperature, NH_4^+ forms fewer hydrogen bonds and exhibits rotational behaviour, which leads to a decrease in the stability of struvite.

Finally, I evaluated kinetic parameters for the decomposition and transformation of struvite with temperature during the struvite transformation experiments. Struvite transformed into two different minerals: newberyite ($\text{MgHPO}_4 \cdot 3\text{H}_2\text{O}$) and dittmarite ($\text{MgNH}_4\text{PO}_4 \cdot \text{H}_2\text{O}$), and one amorphous product, depending on the reaction temperature. The transformation reactions comprise similar reaction orders n of ~ 0.5 and rate constants k of 0.5 – $8.1 \cdot 10^{-4} \text{ s}^{-1}$ for the reaction to newberyite, and $2.9 \cdot 10^{-3} \text{ s}^{-1}$ for the reaction to dittmarite, indicative of a diffusion-dominated mechanism that was interpreted as the transport of NH_3 and water (H_2O) out of the struvite structure. Electron microscopy and Raman spectroscopy revealed that the following nucleation and growth of the new phases occur via a coupled dissolution-precipitation reaction.

In summary, through my thesis, I could extend the knowledge of struvite nucleation and growth kinetics from aqueous solution and give new information on this mineral's decomposition and transformation pathways. This work probed the critical role played by temperature in the formation and decomposition of struvite. My findings contribute to improving struvite precipitation processes in wastewater treatment plants for P recovery. Furthermore, the new insights into the decomposition and transformation parameters of struvite in air have significant implications for struvite fertiliser storage and transportation, as understanding the transformation to secondary phases helps ensure the fertiliser properties and quality.

Thesis outline

| | |
|---|------|
| Eigenständigkeitserklärung | ii |
| Declaration | iii |
| Acknowledgements | v |
| Kurzfassung | vi |
| Abstract | ix |
| List of abbreviations | xiv |
| List of mineral abbreviations | xv |
| List of equations | xvi |
| List of figures | xvii |
| List of tables | xix |
| 1 Introduction | 1 |
| 1.1 Background | 1 |
| 1.2 Research hypotheses | 2 |
| 1.3 Thesis outline | 2 |
| 2 Literature review | 4 |
| 2.1 Phosphorous as a critical resource | 4 |
| 2.2 Kinetics of ambient geochemical processes | 5 |
| 2.2.1 Basics of nucleation and growth | 5 |
| 2.2.2 Kinetics of mineral transformation | 10 |
| 2.2.3 Methods to follow kinetic processes | 12 |
| 2.2 On struvite | 14 |
| 2.4 Kinetics of struvite nucleation and growth | 16 |
| 2.5 Struvite stability, breakdown and transformation in the Mg-phosphate mineral system | 23 |
| 2.6 Scientific and societal relevance of research on struvite | 25 |
| 3 The temperature-dependence of nucleation and growth kinetics of the Mg phosphate mineral struvite | 28 |
| 3.1 Abstract | 28 |
| | xi |

| | |
|---|----|
| 3.2 Introduction | 28 |
| 3.3 Methodology | 30 |
| 3.3.1 Struvite synthesis | 30 |
| 3.3.2 In-situ turbidity and pH monitoring | 30 |
| 3.3.3 XRD characterisation and in-situ XRD experiments | 30 |
| 3.3.4 Kinetic and energetic parameters evaluation | 31 |
| 3.4 Results | 32 |
| 3.4.1 Development of the pH and turbidity profiles | 33 |
| 3.4.2 Struvite crystallisation kinetics from in-situ diffraction analysis | 35 |
| 3.5 Discussion | 38 |
| 3.5.1 Struvite formation behaviour | 38 |
| 3.5.2 Evaluation of kinetic parameters | 39 |
| 3.5.3 Influence of concentration and temperature | 39 |
| 3.5.4 Future indications | 40 |
| 4 A new structure determination of the magnesium phosphate mineral struvite ($\text{MgNH}_4\text{PO}_4 \cdot 6\text{H}_2\text{O}$) at 100 K | 42 |
| 4.1 Abstract | 42 |
| 4.2 Chemical context | 42 |
| 4.3 Structural commentary | 43 |
| 4.4 Database survey | 43 |
| 4.5 Synthesis and crystallisation | 44 |
| 4.6 Refinement | 44 |
| 5 The transformation of magnesium phosphate minerals at atmospheric conditions – A kinetic and mineralogical study with environmental applications | 51 |
| 5.1 Abstract | 51 |
| 5.2 Introduction | 51 |
| 5.3 Methodology | 53 |
| 5.3.1 Starting materials and experiments | 53 |
| 5.3.2 Sample characterisation | 54 |

| | |
|--|-----|
| 5.4 Results | 55 |
| 5.4.1 XRD-derived solid-phase quantification and transformation kinetics | 55 |
| 5.4.2 Microscopic features documenting the phase transformations | 58 |
| 5.5 Discussion | 62 |
| 5.5.1 Struvite transformation products | 62 |
| 5.5.2 Reaction kinetics and replacement mechanism | 63 |
| 5.5.3 Coupled dissolution-precipitation transformation reactions | 64 |
| 5.5.4 Reaction pathways | 66 |
| 5.6 Conclusions and implications | 66 |
| 6 Discussion and concluding remarks | 68 |
| 6.1 Summary of the most important findings | 68 |
| 6.1.1 Struvite nucleation and growth in aqueous solution | 68 |
| 6.1.2 The crystal structure of struvite | 69 |
| 6.1.3 Stability of struvite under different conditions | 69 |
| 6.1.4 Struvite decomposition and transformation | 70 |
| 6.2 Conclusions and impact | 70 |
| 6.3 Future outlook | 72 |
| References | 75 |
| Appendix A Supplementary information to Chapter 3 | 92 |
| Appendix B Supplementary information to Chapter 5 | 97 |
| Appendix C List of publications and presentations | 106 |
| Appendix D List of awards and grants | 107 |
| Appendix E Curriculum vitae | 108 |

List of abbreviations

| Abbreviation | Term |
|---------------------|---|
| AFM | Atomic force microscopy |
| BSE | Back-scattered electrons |
| CIF | Crystallographic information file |
| CNT | Classical nucleation theory |
| DNA | Deoxyribonucleic acid |
| KNT | Kinetic nucleation theory |
| (FT)IR | (Fourier-Transformation) Infrared spectroscopy/Infrarot-Spektroskopie |
| NMR | Nuclear magnetic resonance spectroscopy |
| PCS | Photon correlation spectroscopy |
| RDA | Röntgendiffraktometrie-Analyse |
| REM | Rasterelektronenmikroskopie |
| RNA | Ribonucleic acid |
| SAXS | Small-angle X-ray scattering |
| SEM | Scanning electron microscopy |
| TEM | Transmission electron microscopy |
| UV-Vis | Ultraviolet-visible spectroscopy |
| WAXS | Wide-angle X-ray scattering |
| XRD | X-ray powder diffractometry |

List of mineral abbreviations

| Abbreviation* | Mineral | Mineralogical formula |
|----------------------|------------------------|---|
| Ap | Apatite | $\text{Ca}_5(\text{PO}_4)_3$ |
| Bob | Bobierite | $\text{Mg}_3(\text{PO}_4)_2 \cdot 8\text{H}_2\text{O}$ |
| Bsh | Brushite | $\text{CaPO}_3(\text{OH}) \cdot 2\text{H}_2\text{O}$ |
| Cal | Calcite | CaCO_3 |
| - | Carbonate-fluorapatite | $\text{Ca}_5(\text{PO}_4, \text{CO}_3, \text{OH})_3(\text{OH}, \text{F})$ |
| Ctt | Cattiite | $\text{Mg}_3(\text{PO}_4)_2 \cdot 22\text{H}_2\text{O}$ |
| Dmr | Dittmarite | $\text{MgNH}_4\text{PO}_4 \cdot \text{H}_2\text{O}$ |
| Hap | Hydroxyapatite | $\text{Ca}_5(\text{PO}_4)_3\text{OH}$ |
| - | Hydroxyl-fluorapatite | $\text{Ca}_5(\text{PO}_4)_3(\text{OH}, \text{F})$ |
| Mnti | Monetite | CaHPO_4 |
| New | Newberyite | $\text{MgHPO}_4 \cdot 3\text{H}_2\text{O}$ |
| Suv | Struvite | $\text{MgNH}_4\text{PO}_4 \cdot 6\text{H}_2\text{O}$ |
| Vtr | Vaterite | CaCO_3 |
| Viv | Vivianite | $\text{Fe}^{2+}_3(\text{PO}_4)_2 \cdot 8\text{H}_2\text{O}$ |

*As approved by the International Mineralogical Association (Warr, 2021).

List of equations

| | |
|--|----|
| Equation 2.1 Free energy of a bulk system | 5 |
| Equation 2.2 Value of the free energy barrier | 6 |
| Equation 2.3 Volume of a molecule cluster | 6 |
| Equation 2.4 General form of the rate law | 7 |
| Equation 2.5 Arrhenius equation | 7 |
| Equation 2.6 Free energy of crystal growth | 9 |
| Equation 2.7 General growth rate law | 9 |
| Equation 2.8 Avrami-Erofe'ev equation | 10 |
| Equation 2.9 Biological struvite precipitation in urine | 15 |
| Equation 2.10 General reaction equation of struvite formation | 17 |
| Equation 3.1 General struvite formation equation | 29 |
| Equation 3.2 Avrami equation used for WAXS data fitting | 31 |
| Equation 3.3 General form of the Arrhenius equation | 32 |
| Equation 3.4 Logarithmic form of the Arrhenius equation | 32 |
| Equation 5.1 Decomposition reaction of struvite to newberyite | 52 |
| Equation 5.2 Decomposition reaction of struvite to dittmarite | 52 |
| Equation 5.3 Avrami equation used for XRD data fitting | 55 |
| Equation 5.4 Avrami equation in linear form | 55 |

List of figures

| | |
|--|----|
| Figure 2.1 Change in total free energy during the formation of a molecule cluster | 6 |
| Figure 2.2 Scheme showing the different crystallisation processes according to CNT and KNT | 8 |
| Figure 2.3 Single struvite crystals and crystal morphology | 14 |
| Figure 2.4 Phosphate minerals found in the Skipton Lava Tube Caves | 16 |
| Figure 2.5 Solubility products of struvite | 23 |
| Figure 2.6 Overview of different decomposition and transformation pathways of struvite | 25 |
| Figure 3.1 SEM image of struvite precipitates and powder XRD pattern | 32 |
| Figure 3.2 pH and turbidity curves at different solution concentrations | 34 |
| Figure 3.3 Modelled reaction progress curves for the formation of struvite | 35 |
| Figure 3.4 Development and reaction progress of struvite as obtained from WAXS, Avrami plot, and comparison to pH and turbidity versus time | 36 |
| Figure 3.5 Arrhenius plot to determine the struvite nucleation activation energy | 37 |
| Figure 3.6 Chemical reactions taking place during struvite formation and phosphoric acid speciation in aqueous solutions | 38 |
| Figure 4.1 Polyhedral model of the struvite crystal structure approximately along b | 49 |
| Figure 4.2 Ellipsoidal models and coordination environment of single structural components of the struvite structure at 100 K | 50 |
| Figure 4.3 Network of hydrogen bonds in struvite | 50 |
| Figure 5.1 XRD patterns of powder samples transformed at different temperatures | 56 |
| Figure 5.2 Development of struvite, newberyite and dittmarite weight fractions with time | 57 |
| Figure 5.3 SEM images of struvite crystals after alteration at 22 °C | 59 |
| Figure 5.4 SEM images of struvite crystals after alteration at 37 and 60 °C | 60 |
| Figure 5.5 Raman spectra of struvite, newberyite and dittmarite from single crystals | 61 |
| Figure 5.6 IR spectra of a struvite reference and a struvite sample altered at 60 °C | 62 |
| Figure 6.1 Light microscopy images of struvite altered at 22 °C | 71 |

| | |
|---|-----|
| Figure A1 pH and turbidity curves at solution concentrations of 6 and 8 mM | 92 |
| Figure A2 Reaction progress plot for crystallisation of struvite at 50 °C | 96 |
| Figure B1 Development of newberyite peaks in XRD patterns at 37 °C | 103 |
| Figure B2 Development of newberyite peaks in XRD patterns at 60 °C | 103 |
| Figure B3 Development of dittmarite peaks in XRD patterns at 60 °C | 104 |
| Figure B4 Additional light microscopy images of struvite crystals altered at 22 °C | 104 |
| Figure B5 Additional light microscopy images of struvite crystals altered at 37 °C | 104 |
| Figure B6 Additional SEM images of struvite crystals altered at 37 °C | 105 |
| Figure B7 Crystal-structural models of struvite, newberyite and dittmarite | 105 |

List of tables

| | |
|--|-----|
| Table 2.1 Values of the rate order n derived from the Avrami equation | 11 |
| Table 2.2 Overview of evaluated kinetic parameters of struvite formation | 19 |
| Table 3.1 Induction times, n values and rate constants k for every reaction temperature | 37 |
| Table 4.1 Experimental details | 45 |
| Table 4.2 Bond lengths and angles of non-hydrogen bonds | 46 |
| Table 4.3 Hydrogen-bond geometry | 47 |
| Table 4.4 Fractional atomic coordinates and equivalent isotropic displacement parameters | 48 |
| Table 4.1 Anisotropic thermal displacement parameters | 48 |
| Table 5.1 Reaction orders and rate constants calculated for single-phase transformation | 58 |
| Table A1 Induction times and rate constants k for the crystallisation of struvite at different temperatures from the literature | 93 |
| Table B1 All transformation experiments including reaction temperatures and durations | 97 |
| Table B2 XRD instrument parameters and statistic indicators for Rietveld refinements | 99 |
| Table B3 FT-IR and Raman spectroscopy instrument and measurement parameters | 99 |
| Table B4 List of atom bands detected and assigned using Raman spectroscopy | 100 |
| Table B5 List of atom bands detected and assigned using IR spectroscopy | 101 |
| Table B6 Results of Rietveld refinements of powder samples transformed at 22 °C | 101 |
| Table B7 Results of Rietveld refinements of powder samples transformed at 37 °C | 102 |
| Table B8 Results of Rietveld refinements of powder samples transformed at 60 °C | 102 |

1 Introduction

1.1 Background

Phosphorous (P) is a limited but crucial component for all living beings. It is one of the main compounds of fertilisers used for agricultural food production. On Earth, P resources are limited due to the element's low abundance, mainly in phosphorite rocks and apatite group minerals. Phosphorite deposits are rare on Earth, and mining of phosphorites is a non-sustainable way of gaining P as a resource. There are no P deposits in Europe; therefore, Europe's P supply depends on the supplying countries' economic and political factors (Oelkers and Valsami-Jones, 2008). P is also abundant in high concentrations in human sewage sludges and wastes, so current research focuses on P recovery from wastewater systems. One way of P recovery is by removal of P-containing mineral precipitates such as iron- (Fe-) and Mg phosphate minerals. One of the most important ways to recover P from wastewater is by the precipitation of the magnesium-ammonium phosphate mineral struvite ($\text{MgNH}_4\text{PO}_4 \cdot 6\text{H}_2\text{O}$). Struvite was first described in the 19th century from soils in a former dung pit in Hamburg, Germany (Ulex, 1845-1847). Today, struvite, besides its intentional precipitation and recovery, is often found in the form of scales blocking the pipelines inside wastewater treatment plants. This process further encouraged research on its formation as such scales are an alternate high-yield method for the recovery of P. Struvite obtained from wastewater and pipeline scales have been found to provide a sustainable resource for the recovery of P as well as N to be used as a slow-release fertiliser (Azam et al., 2019; Katakai et al., 2016a; Le Corre et al., 2009). Another interesting reaction that leads to struvite formation occurs in the animal and human body, where it forms as a compound of infection stones, a particular type of kidney stones (Manzoor et al., 2018b). Despite this, relatively little is known about how struvite nucleates or forms from aqueous ions, how stable it is under various chemical or environmental conditions (e.g., fertilisers, human kidney stones, etc.), and even aspects of its crystal structure are still debated.

Many studies have addressed the nucleation and growth of struvite from aqueous solution, including investigation of formation parameters, such as solute concentrations and supersaturations, ratios of Mg, N and P, pH, and sources of P and Mg (Galbraith and Schneider, 2009; Doyle and Parsons, 2002). Laboratory experiments synthesising struvite mimicked different formation environments, such as wastewater and urine (e.g., Le Corre et al., 2009; Ronteltap, 2009). Overall, these studies aimed to produce a bulk struvite material for various applications. However, little research has addressed the mechanisms and kinetic parameters of nucleation and growth of struvite from aqueous solutions. There is a lack of knowledge, especially on the influence of temperature on the kinetics of struvite formation.

Thus, one of my aims was to evaluate the effect of temperature on the nucleation and growth of struvite from aqueous solution, as this is important to understand the influence of process temperatures during precipitation of struvite in different systems (e.g., pipe scaling or intentional precipitation from wastewater streams).

The crystal structure of struvite has been determined several times at room temperature (Ferraris et al., 1986; Abbona et al., 1984; Whitaker and Jeffery, 1970b), yet in particular, the hydrogen bonding network, which is important for the structural stability, has been evaluated with different findings; the newest results about its nature from 2019 (Prywer et al., 2019). Therefore, I aimed to determine the struvite H bonding network at low temperatures and compare it to the previous studies.

Once formed, struvite is unstable in air. As it is used as a fertiliser for agricultural purposes, it is essential to know how it behaves under environmental conditions and what parameters affect its stability and breakdown. It is widely accepted that struvite is thermodynamically unstable at ambient conditions and that it decomposes into other Mg phosphates (Tansel et al., 2018; Bhuiyan et al., 2008). Although the resultant phases are known, a mechanistic understanding of struvite's decomposition in air and the parameters that control the various resultant products, especially under different temperatures, is lacking. This is despite the fact that, for use as a fertiliser, it is crucial to plan the rates at which struvite decomposes so that the fertiliser efficiency is maximised. Following this, I aimed to quantify the kinetics of struvite decomposition and determine the mechanisms of transformation in air as a function of temperature.

1.2 Research hypotheses

Considering the knowledge gaps presented above, this thesis was designed to

- a) Investigate the effects of temperature on the formation kinetics and mechanisms of struvite from aqueous solution as a function of temperature
- b) Evaluate the factors that control the stability of struvite by determining a new struvite crystal structure but at low temperatures
- c) Investigate the effects of temperature on the stability of struvite under atmospheric conditions and determine the mechanisms of its decomposition.

1.3 Thesis outline

This thesis consists of six chapters. Chapter 1 is a brief introduction to the topic and my research objectives. This is followed by a detailed literature review in Chapter 2 and three results chapters,

including two manuscripts in preparation for submission and one data publication together with a preprint. The final chapter, Chapter 6, comprises a summary of the results and an outlook for future possible research avenues. The remainder of the thesis document contains appendixes and the cited references.

2 Literature review

2.1 Phosphorous as a critical resource

P is the 11th most abundant element in the Earth's lithosphere. It is a crucial component for all living beings, as it is part of, e.g., deoxyribonucleic acid (DNA) and ribonucleic acid (RNA) (Fernández-García et al., 2017; Oelkers and Valsami-Jones, 2008). To unravel the origins of life, researchers have been studying possible sources for P to be incorporated into the first forms of living beings (Burcar et al., 2019; Fernández-García et al., 2017; Gull, 2014). Bones and teeth of mammals are most often made of hydroxyapatite [$\text{Ca}_5(\text{PO}_4)_3\text{OH}$] (Pasteris et al., 2008), and besides N, P is the most important component of fertilisers used in agriculture (Azam et al., 2019; Manning, 2008). To provide the required amount of P for the production of industrial fertilisers, the exploitation of geologic P deposits is required.

The primary economically feasible P deposits are sedimentary marine phosphate rocks, igneous rocks and guano deposits (Oelkers and Valsami-Jones, 2008), in which P is found most often as “carbonate-fluorapatite [$\text{Ca}_5(\text{PO}_4\text{CO}_3\text{OH})_3(\text{OH},\text{F})$] in sedimentary rocks as well as hydroxyl-fluorapatite [$\text{Ca}_5(\text{PO}_4)_3(\text{OH},\text{F})$] in igneous rocks” (Filippelli, 2008; Manning, 2008). Important phosphate rock deposits are found in Morocco, China, the USA, and South Africa, among others (Azam et al., 2019; Cordell et al., 2009). Thus, geological deposits are limited. Phosphate rock has been included in the EU Critical Raw Materials list from 2014 to 2020 (European Commission. Directorate General for Internal Market, Industry, Entrepreneurship and SMEs., 2020), and P has been considered a critical raw material by the EU since 2023 (European Commission. Directorate General for Internal Market, Industry, Entrepreneurship and SMEs., 2023). This stresses the importance of finding new, sustainable P sources.

Because of overuse in agriculture, P becomes a common pollutant, often leading to eutrophication. However, an essential part of the P cycle in modern times is controlled by handling municipal wastewater, where P recovery from such systems provides a new, feasible P source (Azam et al., 2019; Wilsenach et al., 2003). Most often, when sewage sludges are supersaturated in specific components, PO_4^{3-} - or N-containing minerals may precipitate and form scales on pipes and wastewater components. This phenomenon led to the intentional precipitation of minerals from wastewater as a P recovery method (Azam et al., 2019). Other elements (e.g., precious metals) or other nutrients may also be recovered depending on the wastewater source and the specific induced precipitation process. For example, when N and P are recovered, they can be used for fertilisers, whereas components such as heavy metals may cause unintentional contamination of the recovered minerals. Typical mineral phases recovered from wastewater are hydroxyapatite, struvite, and vivianite ($\text{Fe}^{2+}_3(\text{PO}_4)_2 \cdot 8\text{H}_2\text{O}$) (Azam et al., 2019; de-Bashan and Bashan, 2004). Struvite has become an important phase in P recovery from wastewater systems, especially. On the one hand, struvite was described as (...) “the main mineral scale

causing problems” (MacAdam and Jarvis, 2015), whereas on the other hand, struvite is the most promising source of sustainable and economically feasible P (Chandrasekaran et al., 2024; Yetilmezsoy et al., 2017). In the scope of P recovery research, precipitation mechanisms of struvite and its potential as a fertiliser have been studied intensively. It is essential to know the kinetics of nucleation and growth of struvite from solution to understand the conditions leading to struvite formation and influencing parameters. To efficiently use the struvite fertiliser product, it is crucial to understand the stability of struvite at ambient conditions and the kinetics of eventual breakdown processes. This is the focus of this thesis.

2.2 Kinetics of ambient geochemical processes

In geochemistry, kinetics describes a process as a function of time where particular parameters change the reaction under observation. Contrary to thermodynamics, where equilibrium is inherent, kinetics is dependent on the path of a process. It is essential to study the kinetics of natural processes to understand how phases – in the case of mineralogy and geochemistry, minerals and crystalline materials – form and which parameters influence their formation, stability or breakdown. In the research presented in this thesis, the kinetics of formation, as well as the breakdown and transformation of struvite, were studied. To do this, it was imperative to thoroughly understand the different theories on crystal nucleation and growth, crystal structure and stability knowledge, and various analytical methods were needed to quantify these processes.

2.2.1 Basics of nucleation and growth

Nucleation is described as an atomistic process by which atoms overcome an energy barrier, and to form a phase, they rearrange themselves into a cluster of a product phase that is large enough to be thermodynamically stable (Benning and Waychunas, 2008; Lasaga, 1998). The theory of nucleation was developed under contributions from Gibbs (1948), Volmer (1939; 1926), and others. This term is commonly used to describe the formation of minerals and crystalline phases from melts and solutions. Nucleation will occur as soon as it overcomes a specific energy barrier, called free the energy barrier ΔG^* (usually, the Gibbs free energy is given in units of kJ/mol, which will be the case throughout this literature review) (Erdemir et al., 2019; Lasaga, 1998). The free energy of the whole system V_{total} is defined by an equation consisting of a term that describes the change in the bulk Gibbs energy and the surface energy of the ions (Lasaga, 1998):

$$\text{Eq. 2.1 } V_{total} = N\Delta G_b + 6((2N)^{\frac{1}{3}} - 1)^2 L^2 \sigma$$

With N being the number of ions forming a cluster, ΔG_b the free energy, L the cation-anion distance in Å and σ being the excess surface free energy in J/cm².

As long as a melt or solution is undersaturated, there is no change in the system's free energy, and reactant molecules will not bind to form clusters without external action. In supersaturated systems, the number of molecular units n increases until it reaches a maximum value, called the critical size n^* (Fig. 2.1). By adding more units n to the cluster after reaching a critical-sized nucleus with a value of n^* , the molecule's surface energy reduces, and the bulk Gibbs energy term of the total free energy increases. Overall, the total free energy V_{total} decreases, allowing the formation of nuclei. Only if the value of n exceeds the value of n^* will the formed clusters be stable and called nuclei (Lasaga, 1998).

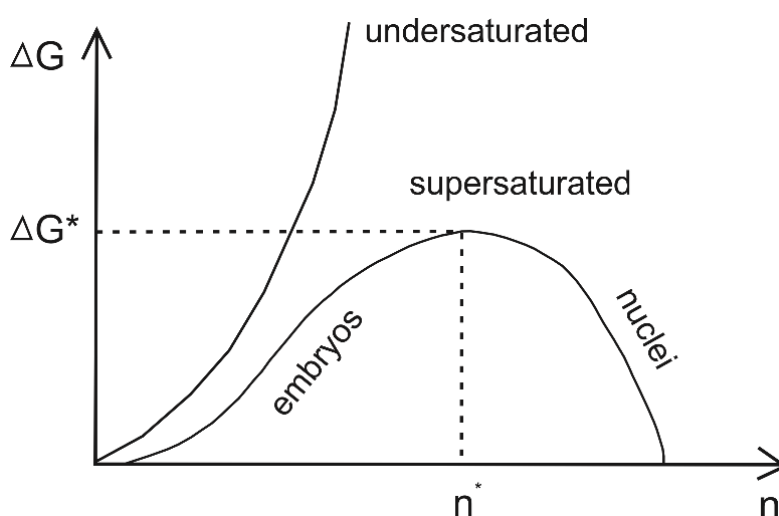


Fig. 2.1 Change in total free energy during a molecule or cluster formation. ΔG^* marks the free energy barrier that has to be overcome to form nuclei. Modified after Lasaga (1998).

The value of the free energy barrier, ΔG^* , can be expressed mathematically by the term (Lasaga, 1998):

$$\text{Eq. 2.2 } \Delta G^* = \frac{16 \cdot \pi \cdot v^2 \cdot \sigma^3}{3 \cdot \Delta G_r^2}$$

With v being the volume of each atom or molecule that binds together as a cluster and ΔG_r the change in free energy of the bulk reaction. It is overall assumed that the forming cluster has a spherical shape as an approximation, implying the relation (Lasaga, 1998):

$$\text{Eq. 2.3 } V = \frac{4}{3} \cdot \pi \cdot r^3 = n \cdot v$$

for the determination of the atom or molecule volume v with r being the radius of the molecule.

It further distinguishes between homogeneous and heterogeneous nucleation. Homogeneous nucleation implies a phase formation from melt or solution by the arrangement of atoms caused by reaching supersaturation of the melt or solution with respect to a reactant phase. In contrast,

heterogeneous nucleation describes the arrangement of molecules to form a product phase by attaching to another solid suspended in the melt or the solution, which acts as a reductant of the free surface energy, leading to a higher nucleation rate (Erdemir et al., 2019; Mullin, 2001; Lasaga, 1998).

Supersaturation describes the state of a solution in which it contains an amount of solute higher than it would have in chemical equilibrium so that the solution is not in equilibrium anymore. During this state, the product phase will precipitate out of the solution until the solutes are in equilibrium again. The state of equilibrium depends on reactant concentrations, pressure, and temperature conditions (Lasaga, 1998). The grade of supersaturation further influences if the processes of crystal nucleation or crystal growth dominate. At low supersaturation, already-formed crystals grow faster than new crystals can nucleate. At high supersaturation, nucleation is preferred over crystal growth, which leads to smaller crystals (Lee et al., 2019; Lasaga, 1998).

The parameters of the rate constant k and reaction rate K are commonly used to describe the kinetics of nucleation and growth. K is expressed by a rate law usually consisting of reactant concentrations C , any real number p , and the rate constant k , in the form of the product of concentration terms (Lasaga, 1998):

$$\text{Eq. 2.4 } K = k * C_A^p * C_B^p * C_C^p * C_D^p$$

Here, the real number is referred to as “ p ” instead of “ n ” to avoid confusion with the number of cluster molecules n that was mentioned before. Depending on the applied model to describe the kinetics and the form of the overall reaction described, the rate law takes different forms. The rate of an overall reaction is determined by the so-called rate-limiting step. In linear processes, this step is usually the slowest step of the reaction that determines the overall reaction rate (Lasaga, 1998). The rate constant k is often strongly dependent on the reaction temperature. This is expressed by the commonly known Arrhenius equation (Lasaga, 1998; Arrhenius, 1889a; Arrhenius, 1889b):

$$\text{Eq. 2.5 } k = A * e^{\frac{-E_a}{R*T}}$$

With A as a pre-exponential factor, E_a as the activation energy of the reaction (usually in kJ/mol), R as the ideal gas constant in J/mol·K, and T as the temperature in K. For example, for the well-studied formation of calcite from aqueous solution under ambient conditions, activation energies of 46–73 kJ/mol were obtained (Rodríguez-Blanco et al., 2011; House, 1984).

The description of nucleation processes solely by the description of the Gibbs free energy of different system components is an approach used by the classical nucleation theory (CNT). CNT was initially developed to describe vapour condensation into a liquid but has also been adapted to crystallisation

from liquids (Mullin, 2001; Gibbs, 1948). It describes nucleation processes based on the assumption that nucleation happens by reducing the free energy of components in the melt or the solution by precipitation. It assumes that nucleating particles bind together by particle-attachment. Various researchers have pointed out that this theory does not consider the influence of nuclei characteristics such as their shape, density, and grade of crystallinity (e.g., Erdemir et al., 2019; Benning and Waychunas, 2008). Furthermore, it has been observed in various kinetic studies that nucleation from a melt or a solution does not take place instantaneously. Instead, specific systems show different stages, from the initial mixing of two solutions to forming the first nuclei. This period of time is referred to as induction time. It is a delay in nucleation caused by the fact that the solute concentrations need a specific time to reach a steady state in melt or solution (Karpinski and Bałdyga, 2019; Lasaga, 1998; Söhnel and Mullin, 1988).

However, a different approach to describing nucleation processes, the non-classical nucleation theory (also called NCNT in the literature) or kinetic nucleation theory (KNT), has evolved in the last decades as a response to observations CNT could not explain. The particular characteristic of KNT is the description of the nucleation process as a multiple-step pathway. This implies that nuclei of a reactant phase do not directly form out of melt or solution through one step but via an intermediate phase, which is often metastable. This metastable phase was observed to be either an amorphous phase or a so-called pre-nucleation cluster consisting of polymers (Fig. 2.2) (Jun et al., 2022; Demichelis et al., 2011) or dense liquid-like precursors, or other nanocrystals (Yoreo et al., 2015).

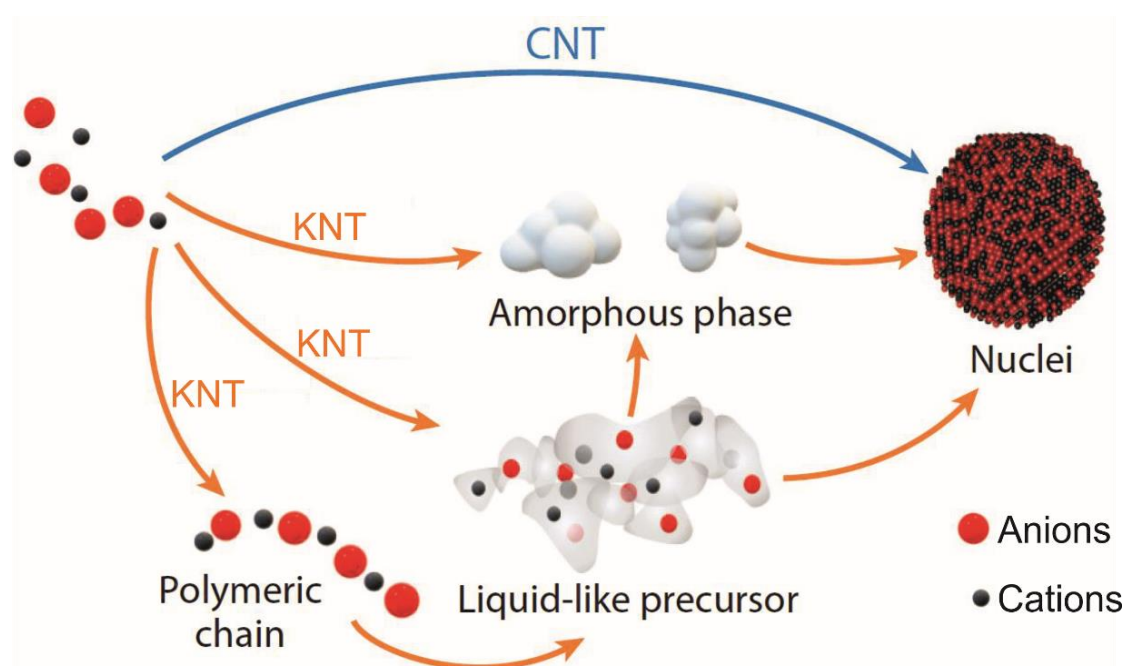


Fig. 2.2 Scheme showing the different crystallisation processes according to CNT and KNT. Modified after Jun et al. (2022).

In contrast to CNT, in KNT, any intermediate metastable phase can and will dissolve and transform further until a thermodynamic stable state is achieved. This leads most often to a multi-step reaction chain that proceeds via the nucleation, growth, and inter-transformation of various components, which can include complexes/polymeric chains, dense liquid-like, or amorphous phases (Erdemir et al., 2019; Benning and Waychunas, 2008).

KNT has been developed in the last decades primarily from observations of crystal growth reactions that aimed at understanding how phases form in sparingly soluble salt systems (e.g., CaCO_3 , CaSO_4 , CaPO_4) (Yoreo et al., 2015). Among these, the formation of calcite from aqueous solution provides an excellent example of a crystal formation process that kinetic nucleation theory can explain well. It was shown that calcite does not form via one step but by transforming from amorphous calcium (Ca) carbonate, sometimes via vaterite, to finally form calcite (Rodriguez-Blanco et al., 2011; Weiner et al., 2005). Another example is the formation of apatite from aqueous solution via the previous formation of amorphous Ca phosphate and further transformation into apatite (Christoffersen et al., 1989).

Crystal growth processes comprise different steps. These are divided into transport processes, which include a long-range transport of atoms through an initial phase or phase boundary layer, and surface processes, which include attachment and movement of atoms on the surface that was created in advance (Erdemir et al., 2019; Karpiński and Bałdyga, 2019; Lasaga, 1998). The growth of a crystalline phase from melt or solution can be dominated by transport or surface processes, but often, it is not only one single process but a complex function that would describe the rate of phase growth (Lasaga, 1998). The free energy of a crystal growth process ΔG comprises the energy gained by adding a number of atoms to the crystal surface ΔE_0 , the energy gained by the bonds between surface atoms, ΔE_1 , the entropy loss in transitioning from liquid to solid, ΔS_0 , and ΔS_1 , the configuration entropy of the surface configuration of a specific number of atoms. The whole term is dependent on the melt/solution temperature, T (Lasaga, 1998):

$$\text{Eq. 2.6 } \Delta G = \Delta E_0 + \Delta E_1 - T * \Delta S_0 - T * \Delta S_1$$

A general law for the calculation of growth rates K is the following (Lasaga, 1998):

$$\text{Eq. 2.7 } K = A * e^{-\frac{E_a}{R*T}} * \prod_i a_i^{n_i} * f(\Delta G)$$

With A as the reactive surface area of the crystal, a as the activity of species i in solution, and n as a real number.

Similarly to the classical and non-classical nucleation theories, different models can describe crystal growth mechanisms. The classical growth theory considers crystal growth as the attachment of atom-by-atom or molecule-by-molecule to a growing surface in a supersaturated system (Andreassen and

Lewis, 2017). There are three different types of classical growth models (Benning and Waychunas, 2008): The Frank-Van der Merwe model assumes that a crystalline phase grows by generating atomic layers after each other (Frank and van der Merwe, 1949). In contrast, the Volmer-Weber model postulates that crystal growth takes place by the nucleation as “islands” on the surface rather than forming atomic layers (Volmer, 1939; Volmer and Weber, 1926). Finally, the Stranki-Krastonov growth model combines both previous models by assuming that crystal growth proceeds initially by forming layers but continues in the form of islands (Stranski and Krastanow, 1937). The mechanisms and rates of crystal growth are primarily affected by supersaturation of the melt or solution, crystal defects (kinks) on the pre-existing crystal surface and the incorporation of impurities (Karpiński and Bałdyga, 2019; Benning and Waychunas, 2008). Processes that are not accounted for by classical growth theory are the formation of metastable phases prior to the final crystalline phase and growth by oriented aggregation of particles. The prior nucleation of a phase, which is not thermodynamically stable, is considered to happen because it is easier to nucleate first. The growth of larger crystals at the expense of smaller crystals, driven by the change in interfacial energy of the particles, is called Ostwald Ripening (Voorhees, 1985; Lifshitz and Slyozov, 1961; Wagner, 1961). Oriented aggregation or attachment describes the attachment of atoms on a crystal surface not layer by layer but in the form of clusters with distinct crystallographic orientations (Li et al., 2012; Penn and Banfield, 1998).

2.2.2 Kinetics of mineral transformation

Phase transformations take place due to a phase being thermodynamically unstable. They entail two different aspects: 1. the mechanism of transformation and 2. the reaction speed, i.e., the kinetics of the reaction. In geochemistry and mineralogy, solid-solid transformations and dissolution-re-precipitation-based transformations are the most important phase-changing processes. The evaluation of kinetic rates assumes that a phase transformation occurs by two distinct, coupled processes (nucleation and growth) that various mathematical models describe. A well-established kinetic model – initially based on the crystallisation of alloys from melts – is the Avrami equation, which is also referred to as the Johnson–Mehl–Avrami–Kolmogorov (JMAK) equation (part 1 of Eq. 2.8) (Lasaga, 1998; Avrami, 1940, 1939; Johnson and Mehl, 1939; Kolmogorov, 1937). Although this model was initially developed for solid-state reactions in crystallising alloys, in many recent studies, it has also been applied to phase transformations in aqueous media (e.g., Kasiotas et al., 2010; Davidson et al., 2008). It can be expanded by including the induction time t_0 , if it applies to the studied system (Bamford and Tipper, 1980) (part 2 of Eq. 2.8):

$$\text{Equation 2.8 } \alpha = 1 - e^{-kt^n} \text{ or } \alpha = 1 - e^{-k(t-t_0)^n}$$

The equation includes the rate constant k , the time t , the induction time t_0 , the reaction progress α and the rate order n . The value of n consists of two components: β , which accounts for the “number of steps involved in nucleus formation”, and λ , which represents the “number of dimensions in which the nuclei grow” (Bamford and Tipper, 1980). It has been used to describe the mechanism of transformation. Bamford and Tipper (1980) and well as Hulbert (1969) distinguished between a range of n values defining the mechanism of the solid-state reaction as well as the growth dimensionality, which Avrami (1940) also postulated before (Tab. 2.1). The transformation of one phase into another one involves 1. the breaking and re-formation of chemical bonds within the host phase and 2. the transport of atoms, ions, or molecules to a reactive zone, which is usually the phase boundary of the host phase (Hulbert, 1969). After that, nucleation and growth of the new phase follow, driving the advancement of the new interface (Bamford and Tipper, 1980). The n value indicates which process dominates the transformation: diffusion or interface-controlled processes. Yet, a combination of different processes was reported to be possible, e.g., for the fluid-driven transformation of aragonite to apatite (Kasioptas et al., 2010).

The growth dimensionality refers to the morphology of the newly formed crystalline phase. Thus, the interpretation of n should always be combined with microscopic observations. If the observed reaction can be described with the Avrami equation, the reaction progress α with time often follows an S-shaped curve (Avrami, 1939). This trend was described for solid-state transformations but has also been observed in many other mineral transformation reactions from liquid to solid and vice versa (e.g., Ballirano and Melis, 2009; Davidson et al., 2008). Other theories describe the kinetics of transformation and decomposition reactions of solid phases based on acceleratory and deceleratory rate equations (Bamford and Tipper, 1980). This literature review focuses on the Avrami theory due to its application throughout this thesis (Ch. 3, 5).

Table 2.1 Values of the rate order n derived from the Avrami equation. From Kirsch et al. (2004), modified after Hulbert (1969).

| Model | | Phase boundary control (n) | Diffusion control (m) |
|--|--------------------------|--------------------------------|---------------------------|
| <i>Three-dimensional growth</i> | | | |
| <i>(Spherical particles of reactant)</i> | | | |
| Nucleation rate | (1) Constant | 4 | 2.5 |
| | (2) Zero (instantaneous) | 3 | 1.5 |
| | (3) Deceleratory | 3–4 | 1.5–2.5 |

| Model | | Phase boundary control (n) | Diffusion control (m) |
|--|------------------|----------------------------|-----------------------|
| <i>Two-dimensional growth</i> | | | |
| <i>(Laminar particles of reactant)</i> | | | |
| Nucleation rate | (1) Constant | 3 | 2.0 |
| | (2) Zero | 2 | 1.0 |
| | (3) Deceleratory | 2–3 | 1.0–2.0 |
| <i>One-dimensional growth</i> | | | |
| <i>(Lath-shaped particles of reactant)</i> | | | |
| Nucleation rate | (1) Constant | 2 | 1.5 |
| | (2) Zero | 1 | 0.5 |
| | (3) Deceleratory | 1–2 | 0.5–1.5 |

Transformation reactions that take place in solids but involve liquid media can lead to the dissolution of the host phase. The dissolution depends on the solubility of the phase and environmental conditions, such as temperature and pressure. If the host phase is dissolved and precipitated somewhere else (that can be, on the surface of the host or on a different phase surface or edge) as a distinct phase, this process is called a dissolution-reprecipitation reaction. If this reaction takes place closely between the host and the new phase, dissolution and reprecipitation are coupled. In this case, the phases show distinct characteristics. These include pseudomorphism of the new phase after the host phase, a change in bulk volume and the development of porosity (Ruiz-Agudo et al., 2014; Putnis, 2009).

2.2.3 Methods to follow kinetic processes

The kinetics of mineral nucleation, growth, and transformation can be quantified using various optical methods, such as visible light or electron microscopy. In addition, these methods can sometimes be combined and complemented with techniques that allow monitoring a change in parameters with time, e.g., change in absorbance, change in diffraction or spectroscopic parameters.

Usually, with microscopy methods, a change in phase morphology with time can be monitored *ex-situ* or *in-situ*. The observation of nuclei growth sites, crystal shape, or pseudomorphism, amongst other features, is useful for the interpretation of the reaction mechanism. For example, light microscopy, scanning electron microscopy (SEM) as well as atomic force microscopy (AFM) enable the user to look at samples on the μm - to nm-scale, which is accomplished by transmission electron microscopy (TEM)

that is useful to observe smallest phase changes and properties such as crystallographic features. In recent decades, such microscopy techniques have been accomplished by cryogenic modes, enabling the observation of unstable phases (Du et al., 2024; Erdemir et al., 2019). Monitoring the change of such properties over a particular time in regular intervals can be used to obtain the parameter of reaction progress α .

Voltametric, spectroscopic or spectrometric techniques are also suitable to obtain kinetic parameters and monitor nucleation processes. Exemplary techniques that were used by several nucleation studies in the last decade comprise time-resolved Fourier transform infrared (FTIR) spectroscopy, photon correlation spectroscopy (PCS) or nuclear magnetic resonance (NMR) spectroscopy, amongst others (Du et al., 2024; Erdemir et al., 2019). Classically, methods to measure the concentration changes in a solution are very suitable for tracking the kinetics of crystallisation in a liquid as well as measuring pH change with time or monitoring the turbidity and/or light absorption of particles in solution through Ultraviolet-visible (UV-Vis) spectroscopy. Furthermore, diffraction techniques such as wide-angle X-ray scattering (WAXS) and small-angle X-ray scattering (SAXS) can be used to follow nucleation and crystallisation in solution using static or flow-through systems (Erdemir et al., 2019; Benning and Waychunas, 2008).

In this thesis, I used *in-situ* turbidity and pH monitoring to track the nucleation and growth of struvite crystals from aqueous solution and complement these analyses with synchrotron-based WAXS and SAXS analyses to derive kinetic parameters (Ch. 3). I employed low-temperature X-ray analyses and derived a more accurate structure of struvite (Ch. 4) and followed its decomposition and transformation in air by *ex-situ* powder XRD complemented by optical and electron microscopy to gain insights into the mechanism of struvite decomposition and transformation (Ch. 5).

2.2 On struvite

Struvite belongs to the group of phosphates. The crystals can be colourless or white to yellowish-brownish. The Mohs hardness is $1\frac{1}{2}$ to 2 with a specific gravity of 1.711 g/cm^3 . It crystallises in the orthorhombic crystal system in the space group $Pmn2_1$ and shows good cleavage in $\{001\}$ and poor cleavage in $\{100\}$ direction with twinning occurring on $\{001\}$. Crystals appear in wedge-shaped, coffin-shaped, short prismatic or tabular morphologies (Anthony et al., 2001-2005) (Fig. 2.3 a, b).

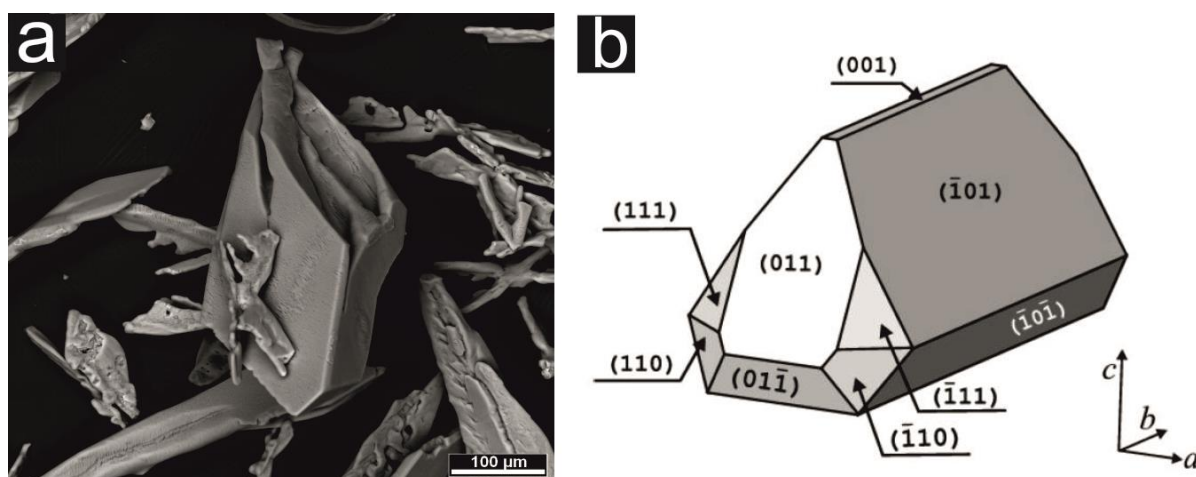


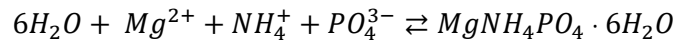
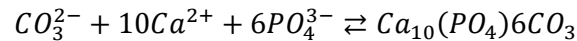
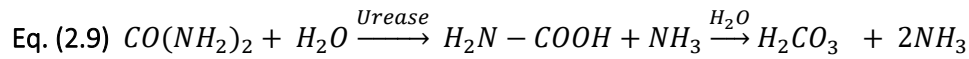
Fig. 2.3 a) Struvite crystals of different morphology under the SEM. b) Crystal morphology with important crystal planes of struvite (Prywer et al., 2019).

In nature, struvite is associated with guano deposits (Teschemacher, 1846) and P-rich soils (Bayuseno and Schmahl, 2020). It was first described by Ulex (1845-1847), who found it in the soil beyond a former dung pit under St. Nicholas Church in Hamburg, Germany. The best investigated, non-natural occurrence of struvite is in wastewater treatment plants. In such industrial plants, struvite can form on the inner surfaces of pipes or other plant equipment in contact with the wastewater. The first description of struvite found in an anthropogenic environment was from a wastewater treatment plant and was published by Rawn et al. (1939). Struvite crystal growth on pipe surfaces slows down the stream flow, increasing the energy input for the movement of flows and leading to additional costs for wastewater companies (Kumar and Pal, 2015; Doyle and Parsons, 2002; Ohlinger et al., 1998; Mohajit et al., 1989).

Researchers focused on preventing struvite precipitation by assessing which additives may slow down the precipitation. However, because P is a scarce commodity on Earth, lately, the focus has shifted to the intentional precipitation of P as struvite from wastewater and sanitary systems because this way, struvite can be recovered and re-used as a sustainable P- and N-source in fertilisers (Doyle et al., 2003; Ohlinger et al., 1998). Studies on the nucleation and growth kinetics and thermodynamic parameters of struvite formation have been conducted to understand better the fundamental reactions and processes

that control or govern P recovery by struvite precipitation. Overall, such studies assess various parameters suitable to mimic wastewater, e.g., chemical composition, pH, or stirring speed (Ariyanto et al., 2014; Capdevielle et al., 2014; Mehta and Batstone, 2013; Kofina and Koutsoukos, 2005; Nelson et al., 2003) but such studies rarely addressed the fundamental mechanisms and pathways of nucleation and growth of struvite itself.

Struvite further occurs in infection stones (a type of urinary stones) in the animal and human body (Manzoor et al., 2018a; Li et al., 2015; Prywer and Olszynski, 2013; Johnson, 1959). Similarly to wastewater, P can be recovered as struvite from urine (Matzdorff, 2020; Rodrigues et al., 2019; Da Filho et al., 2017). Infection stones form by the increase of pH and NH₃ concentration in urine. This is caused by several microorganisms or bacteria producing the enzyme urease. Urease causes hydrolysis of urea (CO(NH₂)₂), which furthermore leads to the generation of NH₃ and carbonic acid (H₂CO₃). The reaction of H₂CO₃ with Ca²⁺ and the reaction of NH₄⁺ with Mg²⁺ ions lead to the precipitation of 1. carbonate apatite (Ca₁₀(PO₄)₆CO₃) and 2. struvite (Manzoor et al., 2018a; Li et al., 2015; Prywer and Olszynski, 2013; Tilley et al., 2008; Bichler et al., 2002):



Paragenetic minerals associated with struvite in guano and other sediments, especially in cave environments, are commonly other Mg phosphates such as newberyite (MgHPO₄·3H₂O), dittmarite (MgNH₄PO₄·H₂O) brushite (CaPO₃(OH)·2H₂O) and monetite (CaHPO₄). Important localities for these mineral assemblies are, e.g., sediments of the Mono Lake, USA (Cohen and Ribbe, 1966), and the Skipton Lava Tube Caves, Australia (Frost et al., 2005; Anthony et al., 2001) (Fig. 2.4).

In association with infection stones and calcitic human or animal residues (bones, teeth), struvite was found in association with end-members of the apatite group, i.e., carbonate apatite and hydroxyapatite (Ca₅(PO₄)₃(OH)) (HAP) (Hassel et al., 2001; Grases et al., 1996; Elliot et al., 1958) besides brushite (Grases et al., 1996), newberyite (Sutor, 1968; Lonsdale and Sutor, 1966), and vivianite (Hassel et al., 2001).



Fig. 2.4 Struvite from guano and other phosphate minerals found in the Skipton Lava Tube Caves. a) Struvite b) Newberyite (Compton, 2009). c) Dittmarite (Eldjarn, 2024).

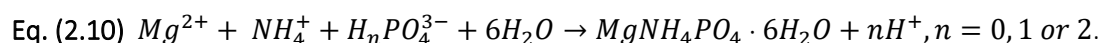
One of the most commonly known isotopes of struvite is Struvite-(K) or K-struvite containing potassium (K) instead of ammonium ($\text{KMgPO}_4 \cdot 6\text{H}_2\text{O}$). This isotype was approved as a new mineral by the International Mineralogical Association in 2003. It occurs in animal and human urine, but the type localities were both ore deposits; one was a sulphosalt deposit in Switzerland and one a galena deposit in Austria (Chauhan et al., 2008; Graeser et al., 2008), where it is described as a secondary alteration product (Graeser et al., 2008). K-struvite can also form from synthetic urine together with sodium (Na)-bearing struvite as a by-product ($\text{NaMgPO}_4 \cdot 7\text{H}_2\text{O}$) (Huang et al., 2019; Gao et al., 2018; Xu et al., 2015). Furthermore, Haferburg et al. (2008) discovered a biomineralised struvite type containing nickel (Ni) $\text{Ni}(\text{NH}_4)(\text{PO}_4) \cdot 6\text{H}_2\text{O}$ that forms in solution in the presence of bacterial activity.

Only a few studies reported the incorporation of heavy metals into the struvite structure. Chand and Agarwal (1991) synthesised zinc (Zn)-struvite isotype, which may also incorporate vanadyl (VO^{2+}) or manganese (Mn^{2+}) ions substituting for Zn. According to Weil (2008), rubidium (Rb) and thallium (Tl) can substitute for NH_4^+ . Perwitasari et al. (2018) analysed synthetic struvite incorporating copper (Cu^{2+}), lead (Pb^{2+}) and Zn^{2+} ions for Mg^{2+} . Furthermore, struvite shows the potential of arsenic (As) adsorption (Rouff et al., 2016; Lin et al., 2013), but detailed studies on this topic are lacking. Although these phases could be formed from solutions in the laboratory, no further information on an abundance of these isotopes in natural environments is available.

2.4 Kinetics of struvite nucleation and growth

To understand the physico-chemical conditions under which struvite precipitation occurs, various synthesis experiments have been conducted.

Struvite forms from aqueous ions if the solution is supersaturated in Mg, N, and P and the molar ratio is equal to or less than 1:1:1 (Le Corre et al., 2009; Doyle and Parsons, 2002) and if the pH is between 7 and 11 (Matynia et al., 2006; Stratful et al., 2001). The reaction equation representing struvite formation is (Le Corre et al., 2007a):



Standard methods of synthesis include chemical precipitation in a stirred batch reactor (e.g., Bouropoulos and Koutsoukos, 2000), a flocculator (e.g., Capdevielle et al., 2014) or a pilot-scale reactor (e.g., Le Corre et al., 2007b). Less common are syntheses in a draft tube magma mixed suspension mixed product removal (DTM MSMPR) type crystalliser (e.g., Matynia et al., 2006), via a counter-diffusion method (Hövelmann et al., 2019a) or by single diffusion gel growth (e.g., Manzoor et al., 2018a). Some authors also used a biomineralisation method by bacteria isolated from soil (e.g., Sinha et al., 2014).

Some studies have focused on improving P recovery by the intentional precipitation of struvite. Therefore, various parameters influencing the crystallisation process have been investigated to optimise the struvite precipitation process. The most critical factors were found to be the concentration of ions (i.e., the supersaturation ratio), the molar ratio of Mg, N and P, and the pH (Bhuiyan et al., 2007; Doyle et al., 2002; Bouropoulos and Koutsoukos, 2000). The Mg:N:P ratio affects the amount of N incorporated into struvite (Celen and Türker, 2001). In the presence of Ca^{2+} ions, a high Ca:Mg ratio of the system can cause simultaneous precipitation of struvite with an amorphous phase in wastewater (Moragaspiya et al., 2019) and calcite (CaCO_3) and HAP in stock solutions (Acelas et al., 2015). Syntheses were conducted under various pH values from 5 to 11 for wastewater, 2 to 12 for urinary solutions and 5 to 11 for stock solutions. The pH affects the supersaturation ratio and, therefore, the amount of P removal (Li et al., 2019). According to other studies, pH also influences the co-precipitation of Ca-bearing phases like apatite (Doyle and Parsons, 2002) and particle size (Ronteltap et al., 2010).

Most studies targeting struvite kinetics used natural or synthetic wastewater in liquid environments. In contrast, experiments in natural and synthetic urine or with pure phosphate and Mg solutions have been the minority. Independently from the experimental solution type, many studies have agreed on the influence of factors such as reactant concentrations (supersaturations), pH, Mg source and reaction temperature. Higher reactant concentrations (higher supersaturations) accelerate the crystallisation of struvite in the solutions (Agrawal et al., 2018; Ariyanto et al., 2014; Mehta and Batstone, 2013; Rahaman et al., 2008). The total concentrations and the molar ratio of Mg:P influence the crystallisation rates. Several studies showed that a higher Mg content than P content leads to faster struvite precipitation (Rahaman et al., 2008; Le Corre et al., 2007a; Quintana et al., 2005). A higher supersaturation leads to an increase in pH, resulting in the connection of increasing pH to increasing nucleation rate of struvite particles (Shaddel et al., 2020; Crutchik and Garrido, 2016; Ronteltap et al., 2010). The intentional precipitation of struvite in environments such as wastewater treatment plants often requires adding a Mg source. Therefore, several studies have examined the influence of different Mg sources, and the parameters considered were source availability and cost efficiency. The effect of using seawater instead

of pure Mg chloride was studied by Shaddel et al. (2020). They observed that seawater led to a decrease in the struvite growth rate. Quintana et al. (2005) reported that the nucleation of struvite became faster when using a byproduct of magnesite calcination instead of magnesium oxide. Interestingly, studies have rarely addressed the effect of temperature on struvite nucleation and growth. Crutchik and Garrido (2016) conducted struvite synthesis experiments over a narrow temperature range (25–35 °C) and found increasing kinetic rates with increasing temperature. Ariyanto et al. (2014) found that the struvite nucleation induction time when precipitated from wastewater decreased with temperature, but again, they studied this over a narrow temperature range (20–30 °C).

Only a few studies determined the kinetic parameters - n and k - for forming struvite from wastewater-type solutions or pure-salt solutions. An overview of these kinetic parameters is given in Table 2.2 (some studies report the reaction rate K instead of k , which is marked in the table). It was found that multiple rate constants k have been published, which are highly variable depending on experimental temperatures and/or different solution supersaturations and/or solution Mg:N:P ratios. Systematic studies evaluating the nucleation and growth kinetics over more extensive temperature ranges are missing from the literature.

Table 2.2 Overview of evaluated kinetic parameters of struvite formation in different solution types in the literature.

| Reference | Solution type | Solution concentration/Mg:N:P | | Initial pH | T [°C] | Induction time [min] | Reported rate constant k/ rate K | | | | |
|------------------------------------|---------------|-------------------------------|-------------------------|------------|--------|----------------------|---|-----------|------|----|------|
| | | ratio/supersaturation ratio | SSR/saturation index SI | | | | | | | | |
| <i>Agrawal et al. (2018)*</i> | Wastewater | Mg:P = 1.2:1 | | 7.05–7.45 | 21–23 | – | k = 1.6 – 11.5 h ⁻¹ | | | | |
| <i>Capdevielle et al. (2016)**</i> | Wastewater | N:P = 3 | | 4.50 | 15 | 5.00–50.00 | K = 10.4, 5.8, 9.4, 14.2 mmol L ⁻¹ h ⁻¹ | | | | |
| | | | | | | | | SI = 1.02 | | | 7.2 |
| | | | | | | | | SI = 1.18 | 8.00 | 20 | 4.35 |
| <i>Ariyanto et al. (2014)</i> | Wastewater | | | 8.00 | 25 | 3.72 | – | | | | |
| | | | | | | | | SI = 1.33 | | | 2.32 |
| | | | | | | | | SI = 1.02 | | | 5.72 |
| | | | | | | | | SI = 1.18 | | | 1.83 |
| | | | | | | | | SI = 1.33 | | | 4.52 |
| | | | | | | | | SI = 1.18 | 8.00 | 30 | 2.88 |
| <i>Jordaan et al. (2010)</i> | Wastewater | – | | 8.40 | 21 | – | k = 1.55 h ⁻¹ | | | | |
| | | | | | | | | SI = 1.33 | | | 1.60 |
| | | | | | | | | | | | |
| <i>Türker and Celen (2007)</i> | Wastewater | Mg:N:P = 1:1:1 | | 8.50 | 37 | – | k = 270 h ⁻¹ (using 1 st order model), 17.76·10 ³ l mol ⁻¹ h ⁻¹ (using 2 nd order model), 1.6 | | | | |

Literature review

| Reference | Solution type | Solution concentration/Mg:N:P | | Initial pH | T [°C] | Induction time [min] | Reported rate constant k/ rate K · 10 ⁶ l ² mol ⁻² h ⁻¹ (using 3 rd order model) |
|------------------------------------|---------------|--|--|---|--------|----------------------|--|
| | | ratio/supersaturation ratio SSR/saturation index SI | | | | | |
| <i>Quintana et al. (2005)</i> | Wastewater | Mg:P = 1.5, using MgO | | 7.80 | 22–25 | – | $k = 0.65 \cdot 10^{-3} \text{ h}^{-1}$ |
| | | Mg:P = 2.0, using MgO | | | | | $k = 0.66 \cdot 10^{-3} \text{ h}^{-1}$ |
| | | Mg:P = 2.5, using MgO | | | | | $k = 0.80 \cdot 10^{-3} \text{ h}^{-1}$ |
| | | Mg:P = 1.5, using BMP | | | | | $k = 0.15 \cdot 10^{-3} \text{ h}^{-1}$ |
| | | Mg:P = 2.0, using BMP | | | | | $k = 0.20 \cdot 10^{-3} \text{ h}^{-1}$ |
| | | Mg:P = 2.5, using BMP | | $k = 0.28 \cdot 10^{-3} \text{ h}^{-1}$ | | | |
| <i>Nelson et al. (2003)</i> | Wastewater | Mg: 28.9 mg/l, NH ₄ ⁺ : 133 mg/l, PO ₄ ⁻ : 19.4 mg/l | | 8.40 | | – | $k = 3.7 \text{ h}^{-1}$ |
| | | Mg: 28.9 mg/l, NH ₄ ⁺ : 127 mg/l, PO ₄ ⁻ : 9.9 mg/l | | 8.70 | 22–24 | | $k = 7.9 \text{ h}^{-1}$ |
| | | Mg: 28.9 mg/l, NH ₄ ⁺ : 124 mg/l, PO ₄ ⁻ : 7.6 mg/l | | 9.00 | | | $k = 12.3 \text{ h}^{-1}$ |
| <i>Hövelmann et al. (2019a)</i> | Pure salt | 3.05 mM | | 8.10 | 25 | 3.50 | – |
| | | 6.10 mM | | | | | |
| <i>Crutchik and Garrido (2016)</i> | Pure salt | | | 8.20 | 25 | 20.00 | $k = 1.72 \cdot 10^{-6} \text{ mol m}^{-2} \text{ h}^{-1}$ |
| | | | | 8.50 | 30 | – | $k = 2.08 \cdot 10^{-6} \text{ mol m}^{-2} \text{ h}^{-1}$ |
| | | N:Mg:P = 3:1:1 | | 8.80 | 35 | 45.00 | $k = 2.57 \cdot 10^{-6} \text{ mol m}^{-2} \text{ h}^{-1}$ |

Literature review

| Reference | Solution type | Solution concentration/Mg:N:P | | T [°C] | Induction time [min] | Reported rate constant k/ rate K |
|-----------------------------------|---------------|--|------------|--------|----------------------|-------------------------------------|
| | | ratio/supersaturation ratio SSR/saturation index SI | Initial pH | | | |
| <i>Rahaman et al.</i> (2008) | Pure salt | SSR = 9.64 | 8.51 | 20 | – | k = 2.034 h ⁻¹ |
| | | SSR = 4.83 | 8.20 | | | k = 1.716 h ⁻¹ |
| | | SSR = 2.44 | 7.91 | | | k = 0.690 h ⁻¹ |
| <i>Le Corre et al.</i> (2007a) | Pure salt | Mg: 1.20 mM, Mg:N:P = 1:2:2 | 9.00 | 25 | 5.00 | k = 9.4 h ⁻¹ |
| | | Mg: 1.35 mM, Mg:N:P = 1:2:2 | | | – | k = 10.7 h ⁻¹ |
| | | Mg: 1.52 mM, Mg:N:P = 1:2:2 | | | – | k = 12.2 h ⁻¹ |
| | | Mg: 1.64 mM, Mg:N:P = 1:2:2 | | | 1.80 | k = 12.5 h ⁻¹ |
| | | Mg: 1.76 mM, Mg:N:P = 1:2:2 | | | – | k = 13.1 h ⁻¹ |
| | | Mg: 1.96 mM, Mg:N:P = 1:2:2 | | | 0.80 | k = 12.7 h ⁻¹ |
| | | Mg: 2.30 mM, Mg:N:P = 1:2:2 | | | 0.50 | k = 13.4 h ⁻¹ |
| | | Mg: 3.5 mM, Mg:N:P = 1:2:2 | | | – | k = 15.7 h ⁻¹ |

Literature review

| Reference | Solution type | Solution concentration/Mg:N:P | | Initial pH | T [°C] | Induction time [min] | Reported rate constant k/ rate K |
|--|---------------|--|------------|---|--------|----------------------|--|
| | | ratio/supersaturation ratio SSR/saturation index SI | | | | | |
| <i>Bouropoulos and Koutsoukos (2000)</i> | Pure salt | | SSR = 3.33 | 8.50 | 25 | 6.00 | $K = 2.87 \cdot 10^7 \text{ mol/h}^{-1}$ |
| | | | SSR = 3.04 | | | 14.00 | $K = 1.87 \cdot 10^7 \text{ mol/h}^{-1}$ |
| | | | SSR = 2.76 | | | 19.00 | $K = 1.75 \cdot 10^7 \text{ mol/h}^{-1}$ |
| | | | SSR = 2.51 | | | 27.00 | $K = 4.33 \cdot 10^6 \text{ mol/h}^{-1}$ |
| | | | SSR = 2.27 | | | 42.00 | $K = 3.33 \cdot 10^6 \text{ mol/h}^{-1}$ |
| | | | SSR = 2.05 | | | 51.00 | $K = 3.17 \cdot 10^6 \text{ mol/h}^{-1}$ |
| | | | SSR = 1.84 | | | 71.00 | $K = 1.67 \cdot 10^6 \text{ mol/h}^{-1}$ |
| | | | SSR = 1.49 | | | 90.00 | $K = 1.17 \cdot 10^6 \text{ mol/h}^{-1}$ |
| | | SSR = 1.13 | 125.00 | $K = 0.5 \cdot 10^6 \text{ mol/h}^{-1}$ | | | |
| <i>Ohlinger et al. (1999)</i> | Pure salt | 4-20 mM, SSR = 1.6-3.1 | | 6.3–7.9 | 22 | 0.20-38.00 | – |

*The study used a seeded synthesis method.

**The synthesis was conducted on different types of natural and synthetic swine wastewater, from which different rates were derived.

2.5 Struvite stability, breakdown and transformation in the Mg-phosphate mineral system

Several studies investigated the stability of struvite in solution. The solubility of struvite in water was determined experimentally to be 169.2 mg/l (Bhuiyan et al., 2007) at 25 °C. Furthermore, the solubility products K_{sp} at temperatures of 10–50 °C were determined by geochemical modelling. Even at equal temperatures, there is some variation of reported solubility products of struvite (Crutchik and Garrido, 2016). It is remarkable that some studies reported the increase of the solubility product with increasing temperature (Crutchik and Garrido, 2016; V. Babić-Ivančić et al., 2002; Aage et al., 1997; Burns and Finlayson, 1982), whereas other publications found an increase of K_{sp} up to 30–36 °C, followed by a decrease of the solubility product value at temperatures > 36 °C (Hanhoun et al., 2011; Bhuiyan et al., 2007) (Fig. 2.5).

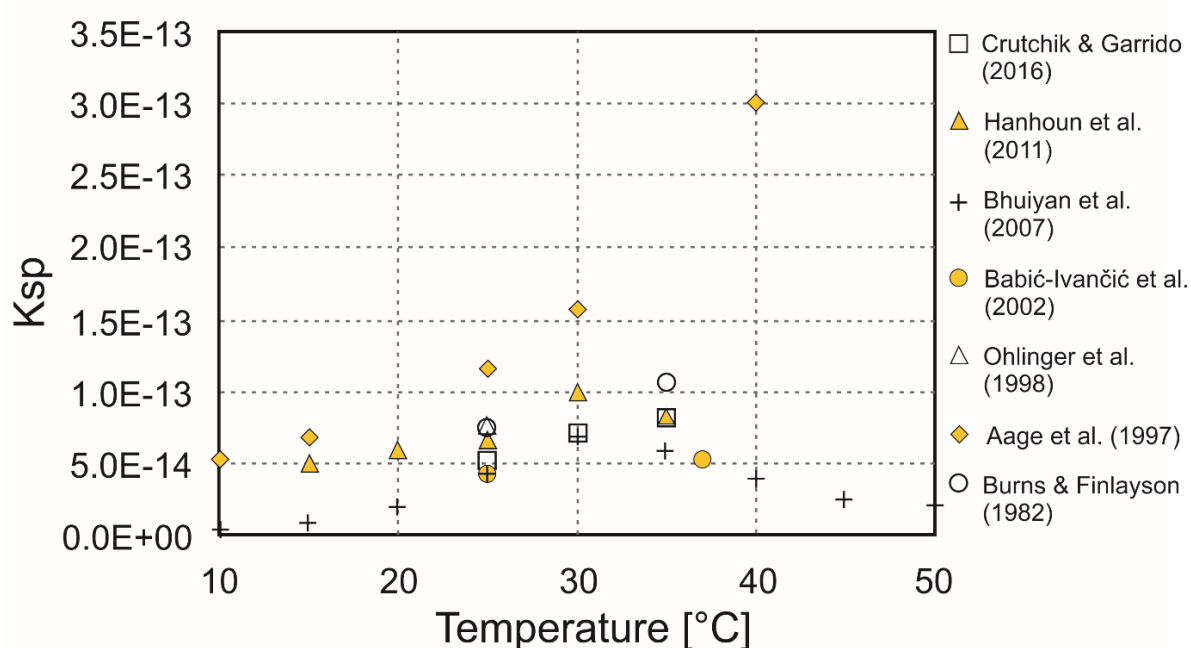


Fig. 2.5 Compilation of reported struvite solubility products. K_{sp} from Ohlinger et al. (1998) ($5.49\text{E-}14$) was calculated from the reported $\text{p}K_s$ value (13.26) and added to the plot. Modified after Crutchik and Garrido (2016).

At ambient conditions (25 °C, 1 bar), struvite is not thermodynamically stable and invariably transforms into other phosphate minerals and/or phases. Yet, the kinetics of these reactions and the physicochemical conditions that drive and control these transformations are not well defined.

Depending on the sample environment, Struvite decomposes and/or transforms into different phases. In solution, struvite transforms into newberyite at room temperature when the pH is kept below 7 (Babić-Ivančić et al., 2006; Babić-Ivančić et al., 2002) or below 5.85 (Abbona et al., 1982). Struvite transforms to cattite ($\text{Mg}_3(\text{PO}_4)_2 \cdot 22\text{H}_2\text{O}$) at a solution pH above 7 (Huang et al., 2015). A solution temperature above 50 °C leads to the formation of bobierrite ($\text{Mg}_3(\text{PO}_4)_2 \cdot 8\text{H}_2\text{O}$). The highest investigated temperatures were referred to as “boiling temperatures”, causing the decomposition of struvite into the monohydrate dittmarite (Bhuiyan et al., 2008).

If struvite is exposed to air, it decomposes by losing its crystal water and ammonia. The subaerial decomposition is reported to start at temperatures of 39 °C (Frost et al., 2004) up to 250 °C (Ramlogan and Rouff, 2016). The total loss of water and ammonia leads to the formation of amorphous magnesium hydrogen phosphate (MgHPO_4) (Hövelmann et al., 2019b), which occurs already at 90 °C. Ramlogan and Rouff (2016) found that struvite partially transforms to dittmarite when heated in air at 100–200 °C. In contrast, Sarkar (1991) described dittmarite as a product of struvite when it is heated in excess water. In comparison, Bayuseno and Schmahl (2020) and Bayuseno and Schmahl (2018) precipitated dittmarite and struvite out of a hydrothermal solution at a temperature range from 60–120 °C. According to the authors, dittmarite rehydration in soils, leading to the formation of struvite, is also possible.

During investigations on natural infection stone samples, Sutor (1968) discovered that struvite started decomposing in air at room temperature after 6 days and fully transformed into newberyite after 6–10 months. Single struvite crystals transformed faster than when struvite crystals were part of infection stones. Whitaker (1968) agreed with this result and reported the decomposition of struvite to newberyite in air when he used different-sized crystal samples. This author mentioned the finding of newberyite in infection stones and developed the idea that newberyite may be a secondary phase grown after the removal of the stone rather than a product that precipitated simultaneously with struvite inside the human body. Tansel et al. (2018) summarised the knowledge about the different struvite decomposition products and conditions in their work (Fig. 2.6).

Despite all the studies mentioned above that evaluated the various pathways of struvite transformation, there is a lack of information about the kinetics of struvite decomposition and transformation processes. Several studies have addressed the kinetics of struvite dissolution concerning different temperatures (~4–35 °C; Aguiar, 2019; Crutchik and Garrido, 2016; Babić-Ivančić et al., 2002) and different crystal morphologies (Babić-Ivančić et al., 2002). But regarding the transformation of struvite, there are only a few studies in the literature (Babić-Ivančić et al., 2006; Babić-Ivančić et al., 2004) that addressed the kinetics of the aqueous transformation of struvite into newberyite as a function of reactant concentrations and pH, and no data on the temperature effect is available. The current state-of-the-art lacks any kinetic characterisation of struvite decomposition and transformation in air. This hinders the evaluation of the mechanisms of transformation into the various possible other phases (Fig. 2.6). This knowledge gap highlights the need for more information on the rates and mechanisms of transformation of struvite in air in particular as this has massive application for the use, storage and transport of struvite as a slow-release fertiliser for agricultural purposes.

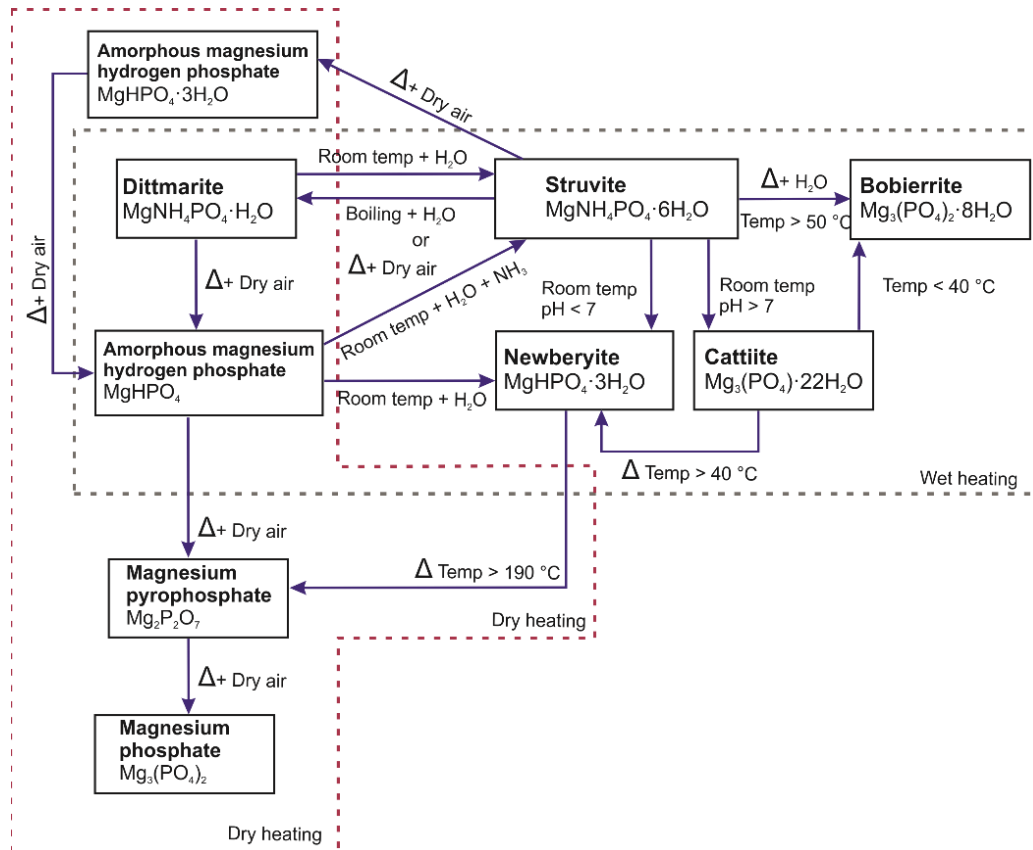


Fig. 2.6 Schematic overview of different decomposition and transformation pathways of struvite under various conditions. Modified after Tansel et al. (2018).

2.6 Scientific and societal relevance of research on struvite

Struvite has been established as the most important phase containing P and N to recover from wastewater (Chandrasekaran et al., 2024). Sidestreams of wastewater treatment plants containing filtrates from dewatering equipment are usually rich in NH_4 and P. This makes struvite a suitable mineral to precipitate aside from the actual wastewater flow (Münch and Barr, 2001). The only component that needs to be added is a Mg source for struvite to form (de-Bashan and Bashan, 2004). P and N recovery through struvite precipitation is not only suitable for wastewater systems but also for recovery from urine (Tilley et al., 2008; Wilsenach et al., 2007). Struvite was successfully recovered from toilet effluent systems (Da Filho et al., 2017). The approach of nutrient recovery from urine was reported to have the potential for developing a cheap recovery method for low-income countries (Dalecha et al., 2014).

Recovered struvite from wastewater is manufactured in the form of pellets and has been established as a fertiliser (Chandrasekaran et al., 2024; Azam et al., 2019; Le Corre et al., 2009; Forrest et al., 2008; Münch and Barr, 2001). It contains nutrients essential for plants (Vogel et al., 2015; Gell et al., 2011; de-Bashan and Bashan, 2004), and its low solubility makes it suitable as a slow-release fertiliser for agricultural purposes (Forrest et al., 2008; Münch and Barr, 2001). However, wastewater-recovered

struvite potentially contains heavy metals that are associated with wastewater streams, e.g., As, cadmium (Cd), (Co), chromium (Cr), Cu, Ni, and Pb. For the majority of such elements, no detectable amounts within or adsorbed to struvite have been found so far (Ronteltap et al., 2010; Uysal et al., 2010). Thus, Lin et al. (2023) and Lin et al. (2013) showed that the incorporation of As into struvite is possible, and Taddeo et al. (2018) detected significant amounts of Cr in struvite precipitated from agroindustrial wastewater. The low number of studies on this topic demonstrates that the incorporation of heavy metals and pharmaceuticals into struvite still requires further research. However, struvite has been recognised as a sustainable fertiliser. It already finds application by, e.g., K+S Minerals and Agriculture GmbH in Spain (K+S Minerals and Agriculture GmbH, 2023) as well as by the Landwirtschaftskammer Niedersachsen (Landwirtschaftskammer Niedersachsen, 2021; Tandler, 2021) in Germany.

Struvite is the main component of infection stones that can form due to infection in the human or animal body. The circumstances of the formation of such stones as well as the avoidance of their formation are subject to ongoing medical research (Wang et al., 2021; Das et al., 2017). Studies combining mineralogy and medicine have investigated the formation of struvite stones by biomineralisation (Li et al., 2015; Griffith, 1978), influencing factors on stone formation (Pérez-García et al., 1989; Elliot et al., 1958) and characterised struvite stones (Hassel et al., 2001; Cifuentes Delatte et al., 1973). New materials for modelling bone implants and prostheses are a recent research topic in medical surgery. As bones and teeth consist of Ca phosphates, the umbrella group of phosphate minerals is considered suitable for synthetic bone tissue substitutes. Struvite, amongst other Mg phosphates, has been investigated on its properties regarding its precipitation conditions and biocompatibility with osteoblasts and bone marrow cell structures (Cao et al., 2019; Tamimi et al., 2011). This shows that research on the formation of struvite in the context of urinary stones and bone material engineering is still an important topic in medical research, to which mineralogical disciplines can contribute.

For various applications in the building sector, fire-resistant materials are needed. Struvite has shown potential for use as a fire-resistant material. It was studied as an additive to wood and found to create a non-flammable gas when heated. The decomposition into amorphous MgHPO_4 was found to act as an insulator in the wood (Guo et al., 2019). Struvite was further found to reduce the flame rate of wood and cotton fabric (Yetilmezsoy et al., 2018). Thus, more studies on the potential of struvite as a fire-resistant material must be conducted to provide reliable results.

As P is a crucial component for living beings, the abundance of P on the Early Earth around the time when first life is believed to have evolved is a vital topic in geosciences. Early life development required prebiotic organic phosphates to develop cells (Burcar et al., 2019; Gull, 2014). Therefore, it is essential

to know which phases existed under environmental conditions of the Early Earth to provide prebiotic phosphates. Struvite is considered as potentially forming under these conditions (Burcar et al., 2019). Feng (2020) proposed the transformation of struvite into Ca phosphate minerals at elevated temperatures that may provide organic P for early life. Following, experiments on the formation and stability of struvite under these conditions have been subject to ongoing research (Feng, 2020; Gull et al., 2020; Burcar et al., 2019).

3 The temperature-dependence of nucleation and growth kinetics of the Mg phosphate mineral struvite

This chapter is adapted from a manuscript in preparation for submission to *European Journal of Mineralogy*:

Volkman, R.; Blukis, R.; Benning, L.G. The temperature-dependence of nucleation and growth kinetics of the Mg phosphate mineral struvite

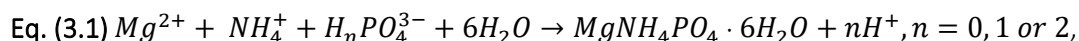
3.1 Abstract

Struvite ($\text{MgNH}_4\text{PO}_4 \cdot 6\text{H}_2\text{O}$), a magnesium phosphate mineral, is the subject of intensive research due to its promising properties for phosphorous recovery from wastewater. Its formation has been investigated under various environmental conditions. However, there is a lack of knowledge on struvite formation mechanisms and kinetics. To address this knowledge gap, we present results from a study where we investigated the temperature-dependent (5–50 °C) struvite formation kinetics from solution through in-situ spectrometry and X-ray diffraction methods. We evaluated 1. the time-resolved growth of Bragg peaks and fitted these with the Avrami equation and 2. pH data through a Monte Carlo simulation. The results were used to determine the kinetic parameters of struvite nucleation and its activation energy describing the crystallisation reaction. Our data revealed only a minor temperature effect on the struvite formation mechanism but a significant change in the induction time. In this work, we present a systematic evaluation and comparison of different parameters that influence the crystallisation of struvite from aqueous solutions.

3.2 Introduction

The Mg phosphate mineral struvite ($\text{MgNH}_4\text{PO}_4 \cdot 6\text{H}_2\text{O}$) is found in various natural and anthropogenic environments. These include guano deposits (MacIvor, 1887; Teschemacher, 1846), urinary concretions (Manzoor et al., 2018a) and wastewater treatment systems (Kumar and Pal, 2015). There has been intensive research on understanding what drives the crystallisation of struvite to devise methods to avoid and remove struvite precipitates from wastewater pipes. Furthermore, the removed struvite scales and/or intentionally precipitated struvite from wastewater have been recognised as a sustainable P- and N-source, particularly for use as slow-release fertilisers (Azam et al., 2019; Doyle and Parsons,

2002). Although thermodynamically, the formation equation for struvite can be written as follows (Le Corre et al., 2009; Bouropoulos and Koutsoukos, 2000):



the kinetics of struvite nucleation and growth from aqueous solutions are still poorly understood. Experimental investigations of its formation from synthetic urine, wastewater, and pure PO_4^{3-} and Mg salt solutions have been conducted at different pH values and Mg:P ratios, but mostly at room temperature (20–25 °C). As an example, struvite crystallisation from pure salt solutions was monitored by Hövelmann et al. (2019a) and Karafiludis et al. (2023b) at 20 °C, and Hövelmann et al. (2019a) as well as Karafiludis et al. (2023a) followed the crystallisation of cobalt (Co) struvite at the same temperature. In addition, in some studies, only indirect means of struvite crystallisation, like changes in solution chemistry, have been used to evaluate the process. For example, the changes in Mg (Capdevielle et al., 2014; Türker and Celen, 2007) or P concentration (Crutchik and Garrido, 2016; Rahaman et al., 2008; Capdevielle et al., 2014; Quintana et al., 2005; Nelson et al., 2003) in the host solution with time have been used to evaluate formation pathways. Overall, from all these studies, a large range of rate constants k were reported for 25 °C. These range from 0.69–15.70 h^{-1} (Rahaman et al., 2008; Le Corre et al., 2007a), yet no studies investigated the kinetics of struvite formation below 20, and only a few at temperatures higher than 35 °C. Also, there is no systematic or temperature-dependent evaluation of how pH or turbidity changes during crystallisation or how struvite actually crystallises through analysing the formed products in a time-resolved manner. Taken together, these studies revealed the necessity of a systematic study combining various methods that allow us to follow the kinetics of nucleation and growth of struvite under a broader spectrum of environmental conditions, while the monitoring of these processes is held as *in-situ* as possible. Such knowledge is especially important to design better pathways for the recovery of struvite from the plethora of anthropogenic sources, e.g., urine (Da Filho et al., 2017), swine farm wastewater (Capdevielle et al., 2016), or industrial wastewater (Kataki et al., 2016a).

To fill this knowledge gap, we present here results from a study where we determined the kinetic parameters and energetics of this system by combining time-resolved and *in-situ* monitoring of changes in pH, changes in turbidity and changes in diffraction of the forming solids as observed by following the changes in Bragg peaks developing during struvite growth by using synchrotron radiation-based WAXS. This data was fitted using two different kinetic models. Data from the *in situ* pH measurements was fitted using a Monte Carlo simulation, while turbidity and WAXS data were fitted with the Avrami equation (Hulbert, 1969; Avrami, 1940, 1939). This approach has often been applied to a range of formation and transformation reactions of sparingly soluble salts (e.g., iron oxides, carbonates) (Roza-Llera et al., 2023; Mulders et al., 2021; Bots et al., 2012; Kasioplas et al., 2010; Davidson et al., 2008).

3.3 Methodology

3.3.1 Struvite synthesis

The struvite synthesis experiments were conducted following the method described by Hövelmann et al. (2019a). In brief, for each experimental series $(\text{NH}_4)_2\text{HPO}_4$ (Sigma-Aldrich, $\geq 98\%$ purity) and $\text{MgCl}_2 \cdot 6\text{H}_2\text{O}$ (Honeywell Fluka, $\geq 98\%$ purity), solutions of various concentrations were prepared with MilliQ water. To start an experiment, the MgCl_2 solution was added rapidly under stirring to the $(\text{NH}_4)_2\text{HPO}_4$ solution of the same concentration so the resulting solution was equimolar. This led to the formation of a precipitate. This approach was used for all *in-situ* and time-resolved experiments, which are detailed below.

3.3.2 In-situ turbidity and pH monitoring

Changes in the experimental solution pH and turbidity were followed, and the induction time and growth kinetics were evaluated using four different solution concentrations (5 mM, 6 mM, 8 mM, 15 mM) at three different temperatures (5 °C, 25 °C, 37 °C). Every measurement was repeated three times. A Thermo Scientific Evolution 200 UV-Vis spectrometer connected to a Peltier control and cooling unit was used for turbidity measurements. The selected wavelength was 700 nm, which was found to produce the lowest absorption of the initial solutions, according to Hövelmann et al. (2019a). A double junction combination pH electrode with a semi-micro tip (Thermo Scientific model 9110DJWP) was used for the pH measurements. Both measurements were recorded at a 1 s-time resolution, and experiments were followed for a duration of 15 min (900 s). Both these types of experiments were conducted in 5 ml cuvettes inside the UV-Vis spectrometer housing, where the Peltier system controlled temperature and stirring (1600 rpm). Before mixing, in all experiments, the turbidity and the pH of the initial $(\text{NH}_4)_2\text{HPO}_4$ were recorded for 10 s before adding the MgCl_2 solution.

3.3.3 XRD characterisation and in-situ XRD experiments

Prior to carrying out the *in-situ* and time-resolved synchrotron diffraction experiments, a batch of struvite crystals was synthesised and separated from the reacting fluids. The solids' identity was confirmed using powder XRD (using a Stoe StadiP diffractometer), and their morphologies were imaged using scanning electron microscopy (SEM) (Zeiss Ultra Plus). The diffraction patterns were collected using $\text{Cu K}\alpha$ radiation in a modified Debye-Scherrer geometry, and the instrument was operated at 40 kV and 40 mA. Data collection occurred within a 2θ range of 0–83.985 ° with a step size of 0.015 ° and a counting time of 32 s per step. In all cases, the end product was crystalline struvite, and no other phases were detected. SEM images were collected using the cryogenic mode (using a Leica EM VCT100 specimen transfer system), as struvite is known to be unstable in vacuum (Hövelmann et al., 2019a), by inserting liquid nitrogen, creating temperatures of –180 °C in the sample chamber. Powders were

deposited on a carbon-padded aluminium stub that was subsequently coated with 20 nm carbon. Images were acquired using secondary electrons at a voltage of 1.4 keV.

The synchrotron-based *in-situ* and time-resolved WAXS experiments were conducted at beamline I22 at the Diamond Light Source Facilities, Didcot, England. We used the same experimental procedure described above for turbidity and pH measurements but with a larger solution volume and a flow-through setup. Furthermore, to obtain a good signal-to-noise ratio for the solution diffraction patterns, we used higher initial solution concentrations (30 mM). The experiments were performed over a temperature range of 5–50 °C. Injection was done remotely through the use of a Bio-Logic SFM-400 mixing system in which the MgCl₂ solution was preheated before injection. The (NH₄)₂HPO₄ solution was preheated (in a water bath) in a double-walled jacketed batch reactor that was continuously stirred. The solution from the reactor was passed via a peristaltic pump within a circuit through a flow-through Hilgenberg capillary of 0.9 mm diameter that was aligned with the beam.

The WAXS data was collected with the energy source operated at 12.4 keV with an emitted beam wavelength of 0.62–1.77 Å. It was monochromatised by a 111-cut double-crystal Si monochromator, and emitted radiation was collected by a Pilatus P3-2M-DLS-L, 172 µm pixel size detector. The 2θ range for the WAXS measurements was 3.75913–71.93471 ° (equivalent to a q range of 0 to ~ 3.86 Å⁻¹), and the diffraction data was collected at an interval of 1 s per frame with experiments running for a total duration of 300 s. The raw diffraction data was processed using the software Dawn (Basham et al., 2015), and further data treatment, including background subtraction and peak fitting, was done with ORIGIN (OriginLab Corporation).

3.3.4 Kinetic and energetic parameters evaluation

The *in-situ* pH data was fitted using a Monte Carlo simulation assuming that the decreasing H⁺ concentration mirrors the struvite precipitation path (Eq. 3.1). The nucleation and growth of struvite with time was simulated by including a number of precursor formation steps (further called “reaction steps”) until a good fit was achieved. These steps represent several chemical reactions assumed to take place during struvite nucleation. The number of steps to include was determined by a trial-and-error procedure until the fit was sufficient. Subsequently, the simulated struvite concentration development was compared to the corresponding time-resolved turbidity curves. We optimised the fit using the 15 mM turbidity and pH patterns at 37 °C. The software used was Igor pro 8 (WaveMetrics, Inc., 1988-2019).

The WAXS data was fitted using the Avrami equation (Lasaga, 1998; Avrami, 1940, 1939):

$$\text{Eq. (3.2)} \quad \alpha = 1 - e^{-k(t-t_0)^n}$$

where k is the rate constant (in s^{-1}), t is the time (in s), α is the reaction progress, and n is the reaction order. α is determined experimentally from the change in integrated area under developing Bragg peaks, while k and n are calculated from the linear fits of $\ln[-\ln(1-\alpha)]$ versus $\ln(t)$. Bamford and Tipper (1980) further suggested using $t-t_0$ replacing t , including the induction time t_0 . Furthermore, the activation energy E_a of struvite formation was determined from the Arrhenius equation:

$$\text{Eq. (3.3)} \quad k = A * \exp\left(\frac{E_a}{R*T}\right)$$

where k is the rate constant (Eq. 3.2), A is the Arrhenius constant, R is the universal gas constant and T is the temperature in Kelvin. If the natural logarithm is applied to remove the exponential function, the following relationship will be given:

$$\text{Eq. (3.4)} \quad \ln k = \ln A * \frac{-E_a}{R*T}$$

A linear fit of $\ln(k)$ versus $1/T$ is used to determine E_a . The slope of the linear fit b is E_a/R . Subsequently, E_a can be calculated by multiplying $-b$ with R .

3.4 Results

The dried precipitates in all synthesis experiments at all temperatures and concentrations were white powders. Images of these powders revealed that the solids were 5–20 μm -sized crystals with prismatic to tabular morphology (Fig. 3.1, a). When analysed with powder XRD, the precipitates were identified as pure struvite (Fig. 3.1, b).

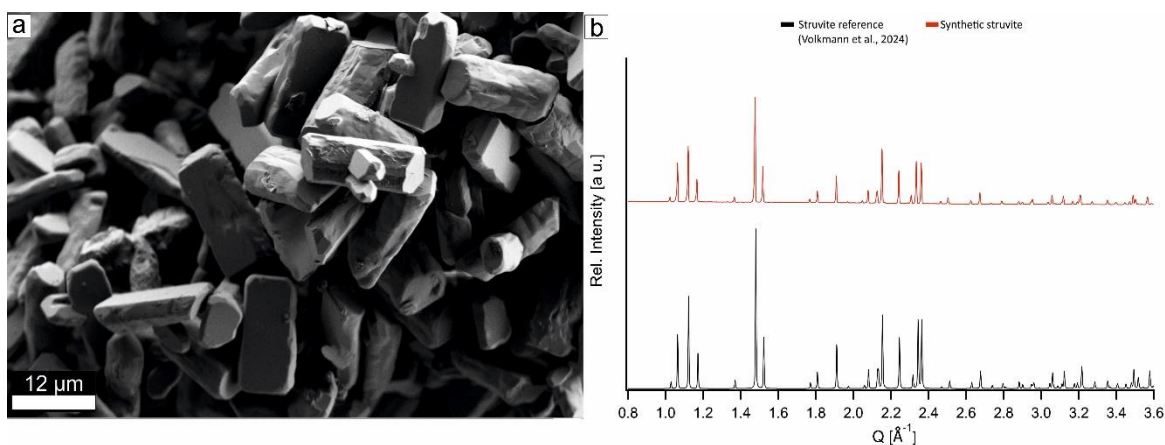


Fig. 3.1 a) SEM image of struvite precipitates obtained during synthesis. b) Powder XRD pattern of the same sample and a reference (Volkman et al., 2024).

3.4.1 Development of the pH and turbidity profiles

Examples of the development of the temperature-dependent pH profiles at 5 mM and 15 mM concentrations are shown in Figure 3.2, a, b. The initial pH of the $(\text{NH}_4)_2\text{HPO}_4$ solution varied with solution concentration and temperature between ~ 7.6 (5 °C, 15 mM) and ~ 8.0 (25 °C, 15 mM). Upon mixing with the respective equimolar MgCl_2 solution, in all experiments, the pH immediately decreased by ~ 0.2 (Fig. 3.2, a, b) and after a brief plateau, a continuous decrease followed until it reached a constant value that varied between 6.2 and 7.6 depending on temperature and concentration. The time of the second drop was defined as the induction time for the formation of struvite. The pH dropped between ~ 0.1 to 0.4 units, depending on reaction temperature (Fig. 3.2, a, b). The effect of concentration was manifested by a reduction in the time after mixing and until the second pH decrease occurred. For example, at 25 °C at the highest concentration (15 mM), this time was reduced by ~ 70 s compared to the lowest concentration (5 mM) (Fig. 3.2, a, b). Similarly, an increase in temperature from 5 to 25 °C also led to a decrease in the duration until the second pH drop occurred. In contrast, at solution temperatures from 25 to 37 °C, this period increased at constant concentrations (Fig. 3.2, a, b).

The turbidity curves followed a similar pattern for all concentrations and temperatures, matching the development of the pH profiles. For example, the time-resolved patterns of 5 and 15 mM (Figure 3.2, c, d; for other patterns, see App. A, Fig. A1) revealed that an initial low-intensity period was followed by a sharp increase in turbidity. This increase reached a maximum intensity, after which the data plateaued. In some cases, a drop in intensity was observed (e.g., at 25 and 37 °C, Fig. 3.2, c, d). The induction time was determined as the period between the mixing of the reactant solutions that happened 10 s after starting recording data and the first observable time point where the turbidity signal was markedly above noise level. The induction time was more pronounced with changing concentration and less pronounced with changing temperature. Like the pH profiles, the turbidity-derived induction time shortened with increasing concentration. For example, at 25 °C, the induction time decreased by ~ 70 s from the 5 to 15 mM experiment (App. A, Tab. A1). At a constant temperature of 25 °C, similarly, the period of rapid increase in turbidity became shorter with higher concentrations and lasted between ~ 90 s (15 mM) and ~ 350 s (5 mM) (Fig. 3.2, c, d). Contrary to the faster drop in pH, the rise in turbidity became constantly slower with higher temperatures. Overall, the effect of temperature on both pH and turbidity of the formation of struvite was stronger at lower concentrations.

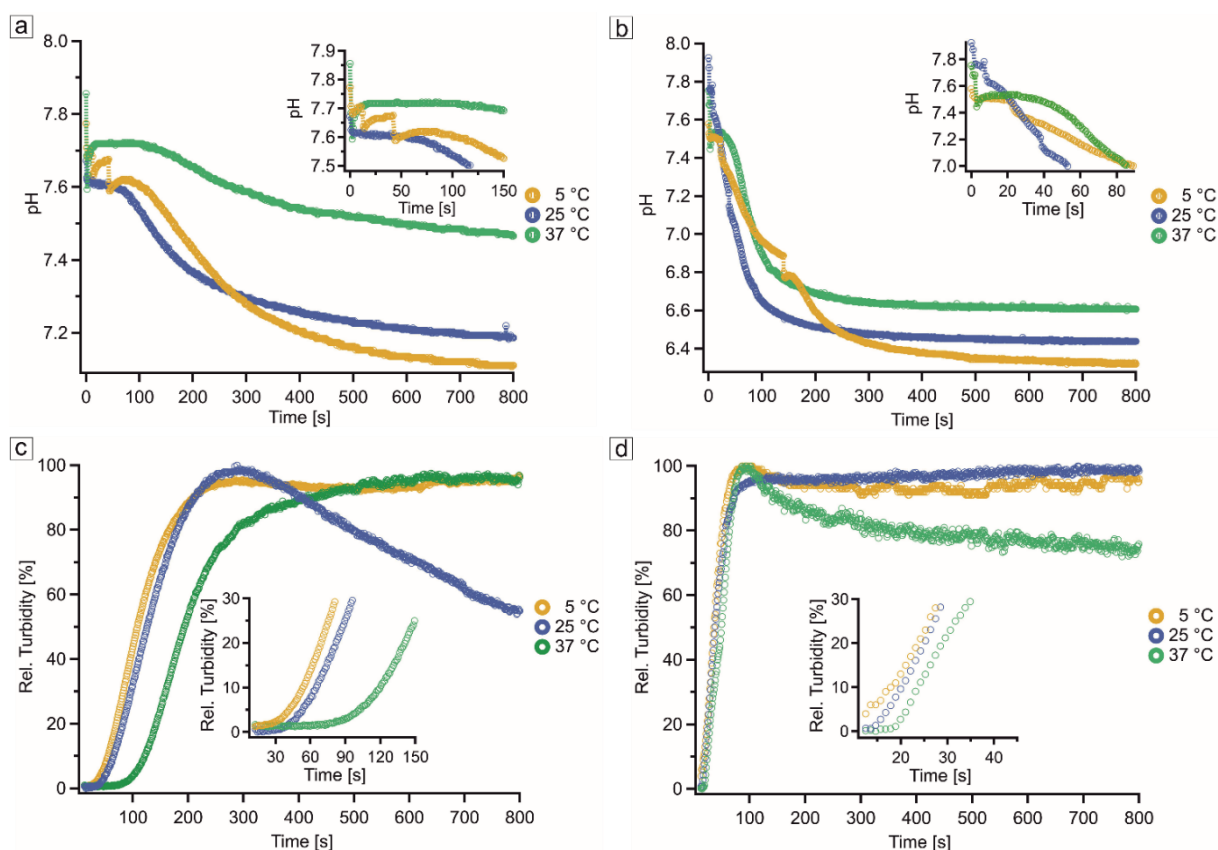


Fig. 3.2 a) pH curves at a solution concentration of 5 mM. b) pH curves at a solution concentration of 15 mM. c) Turbidity curves at a solution concentration of 5 mM. d) Turbidity curves at a solution concentration of 15 mM.

Modelling the reaction progress of struvite formation based on the pH data (Fig. 3.3) and comparing it with the development of the turbidity at the same condition helped us evaluate the various possible reaction steps contributing to the overall reaction. At 15 mM and 37 °C, for example, the fits to the pH curve suggested five possible reaction steps, with the first two steps having peaks before the sharp rise in turbidity at the same conditions and the other three steps within the turbidity space. We assumed that the first reaction step that takes place in the solution after mixing comprises the reaction PO_4^{3-} and Mg^{2+} , forming the first intermediate product. When we plotted the sum of reaction steps 3, 4 and 5, the resulting curve fitted the experimental turbidity data very well. We derived the rate constant k for the overall formation process based on the last reaction step 5. This step was assumed to represent the reaction of the last chemical species with NH_4^+ forming the final struvite, and this reaction was considered to be of 2nd order. The value for k was derived as $\sim 4.1 \text{ (mmol/l)}^{-1}\cdot\text{s}^{-1}$. This modelled curve described struvite formation based on the corresponding pH data. It revealed a longer induction time than observed from the corresponding turbidity curve, which may reflect the faster chemical change measurable in the pH monitoring compared with the turbidity increase (Fig. 3.2, b; Fig. 3.3).

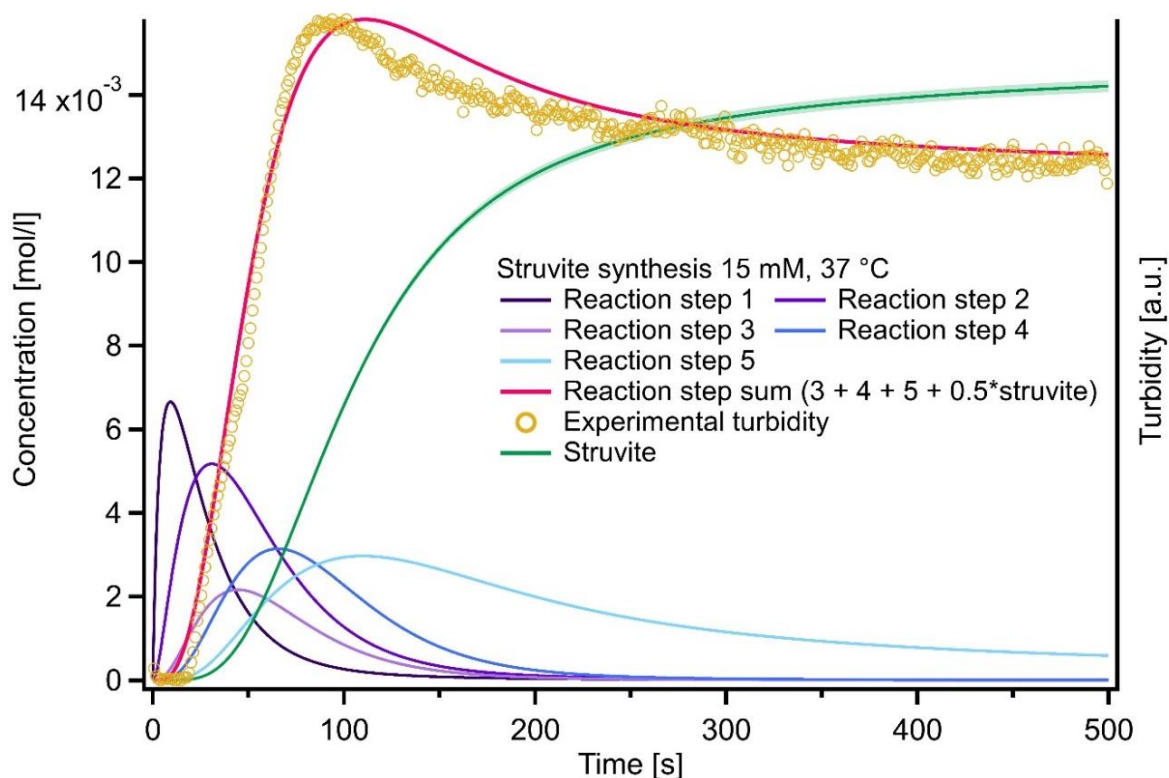


Fig. 3.3 Modelled reaction progress curves for the formation of struvite (green curve) based on the experimental pH data for the synthesis at 15 mM, 37 °C. The Reaction step sum, comprising different chemical species that form during the reaction to struvite (red curve), closely reflects the experimental turbidity data (yellow data points).

3.4.2 Struvite crystallisation kinetics from in-situ diffraction analysis

The time-resolved and *in-situ* WAXS data (Fig. 3.4) from experiments carried out at a concentration of 30 mM revealed that the first diffraction peaks appeared after ~ 25 to 27 s at each temperature (Fig. 3.4, a; Tab. 3.1). To evaluate the reaction progress, the integrated peak area of the main peak for each experiment was computed and the evaluation shows a fast increase in area that reached a plateau after about ~ 50 s at all temperatures (Fig. 3.4, b), after which only a minor decrease was observed. No peaks, other than those assigned to struvite, were observed.

Among several significant diffraction peaks for struvite, the main (111) peak exhibited, not surprisingly, the most prominent change in intensity with time at all experimental temperatures. The integrated area of this peak from the experiments conducted at 50 °C showed irregular patterns (App. A, Fig. A2) that were unsuitable for peak fitting. Thus, this peak area was excluded in further fitting. The change in integrated area for all other peaks with time was plotted as the normalised reaction progress α vs. time at all temperatures (Fig. 3.4, b). The shape of the reaction progress curve does not differ significantly at different temperatures, except 25 °C, where the formation of the plateau started at ~ 90 s. When comparing the reaction progress from the WAXS data with the data from the turbidity and pH in

experiments carried out at the same concentration and at 25 °C, we observed that the turbidity already started to increase after ~ 10 s, which was also mirrored by the decrease in pH (Fig. 3.4, d).

Using the Avrami equation, the reaction order values n and rate constants k were determined for the different temperatures (Fig. 3.4, c). For the corresponding $\ln[-\ln(1-\alpha)]$ versus $\ln(t-t_0)$ plots, only data points of the period of peak growth, i.e., reaction progress increase (25–50 s), were used.

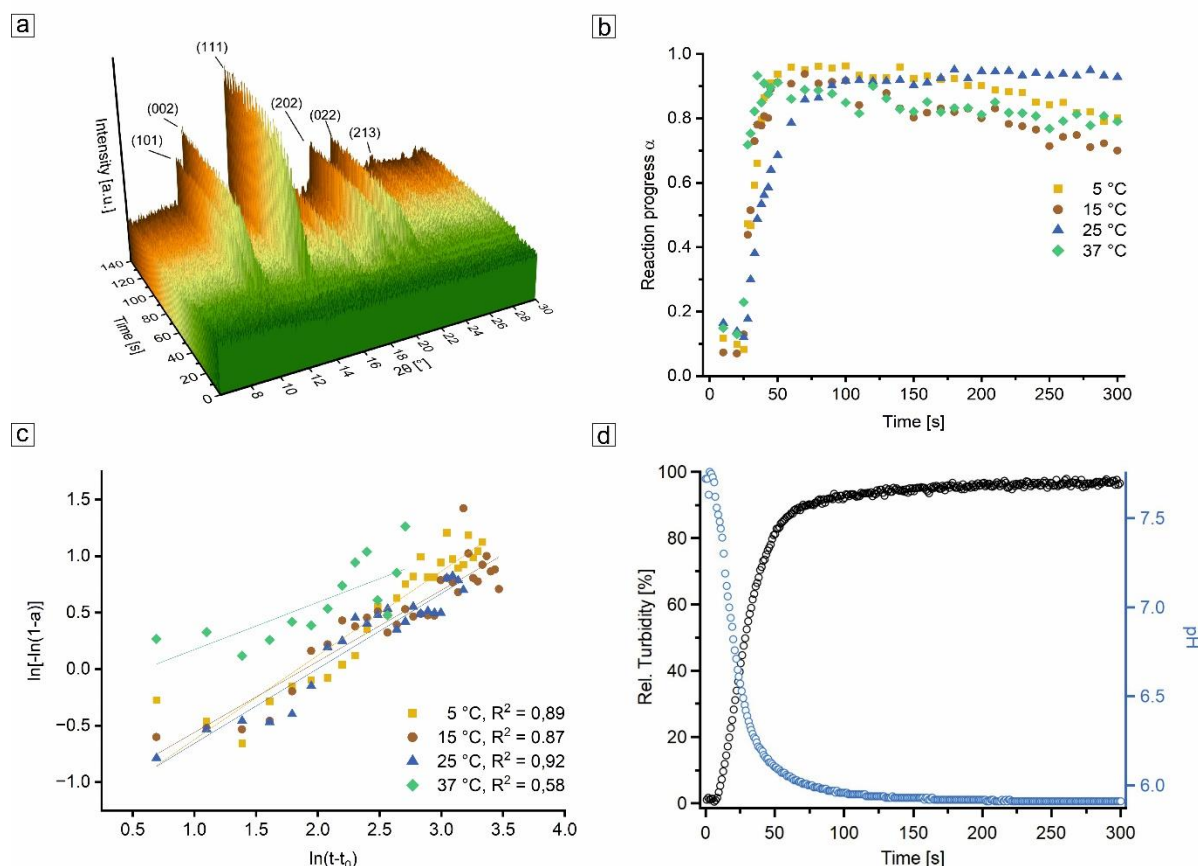


Fig. 3.4 a) 3D waterfall plot showing the development of struvite diffraction peaks during the aqueous crystallisation at 25 °C. b) Reaction progress α versus time plot showing the struvite nucleation and growth progression at different temperatures. c) Linear fits using the Avrami equation to obtain the reaction order n . d) pH and turbidity vs. time of struvite nucleation and growth at 25 °C with a solution concentration of 30 mM, showing an induction time of ~ 10 s in contrast to the WAXS-derived induction time of ~ 25 s at the same temperature (in b).

The calculated n values range between 0.42 (37 °C) to 0.75 (5 °C) (Tab. 3.1) and show a considerable similarity at the different temperatures. The rate constant k ranges from 0.25 (5 °C) to 0.78 s^{-1} (37 °C) (Tab. 3.1) with a comparably high value for the 37 °C experimental series. The Arrhenius equation was used to calculate the activation energy E_a for the formation of struvite from aqueous solution (Fig. 5). The derived activation energy was 17.2 kJ/mol (Fig. 3.5, Tab. 3.1).

Tab. 3.1 Overview of induction times, n values and rate constants k for every reaction temperature derived from evaluation of the WAXS data.

| Nucleation temperature [°C] | Appearance of first peaks [s] | Reaction order n | Rate constant k [s ⁻¹] | Activation energy [kJ/mol] |
|-----------------------------|-------------------------------|------------------|------------------------------------|----------------------------|
| 5 | 25 | 0.75 ± 0.05 | 0.25 ± 0.03 | |
| 15 | 26 | 0.63 ± 0.01 | 0.30 ± 0.03 | |
| 25 | 27 | 0.66 ± 0.04 | 0.26 ± 0.02 | 17.2 ± 0.5 |
| 37 | 25 | 0.42 ± 0.1 | 0.78 ± 0.05 | |
| 50 | 26 | – | – | |

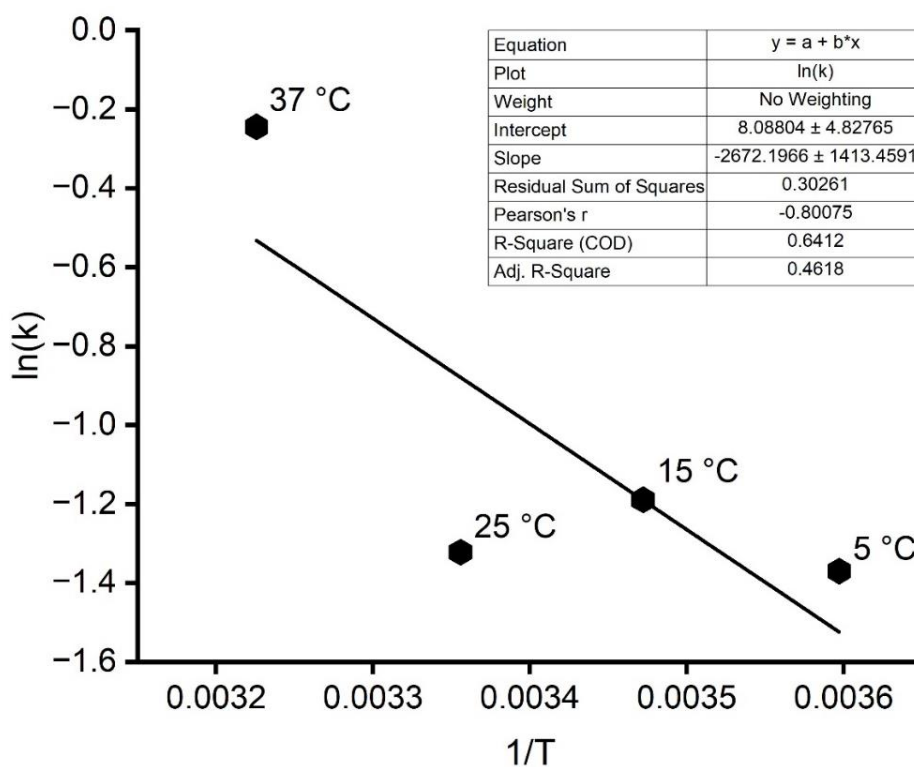


Fig. 3.5 1/T versus ln(k) (Arrhenius) plot used to determine the activation energy of struvite formation from aqueous solution.

3.5 Discussion

3.5.1 Struvite formation behaviour

Based on the pH, turbidity and diffraction data presented above, we can describe the formation of struvite from aqueous solution as follows: after the mixing of the starting solutions, struvite starts nucleating after an induction time, which is dependent on the solution concentration/supersaturation and temperature. The initial nucleation of solids in our experiments was evidenced by the drop in pH and the increase in turbidity due to the scattering of light by the newly forming particles. The formation of crystalline particles was evidenced by the growth of diffraction peaks as observed by WAXS. Correspondingly to the rise in turbidity, the pH decreased, caused by the release of H⁺ ions during the mixing and subsequent chemical reactions during struvite formation. The transition from ions to solids and to crystallisation progresses via the formation of different aqueous PO₄³⁻ species, which react with the aqueous Mg and the NH₄⁺ in the water H₂O (Fig. 3.6, a). We observed that the pH decreased in two distinct steps. The initial period of constant pH is likely caused by buffering reactions in solution, linked to the gradual protonation of PO₄³⁻ species (Fig. 3.6, b).

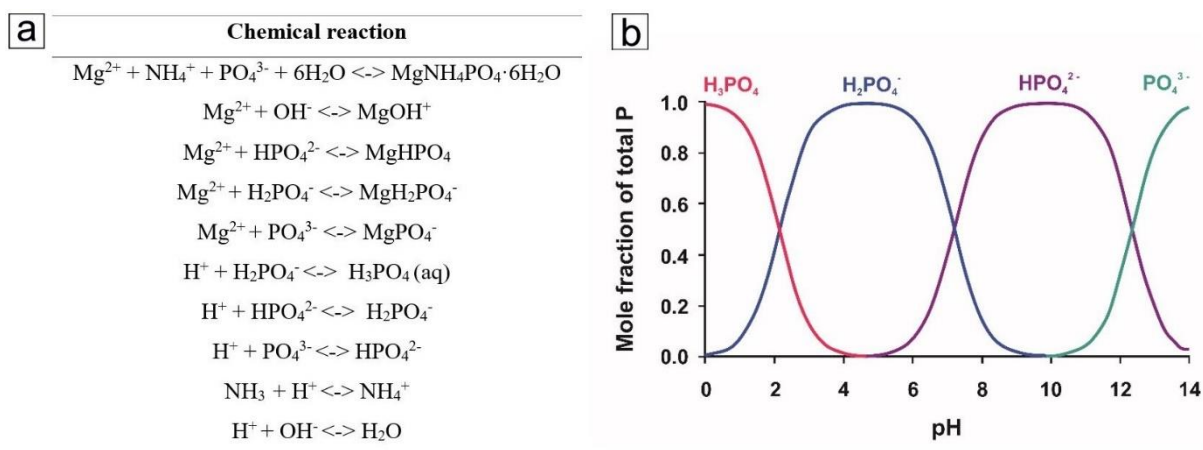


Fig. 3.6 a) Chemical reactions taking place during struvite formation in aqueous solution (Fattah et al., 2022; Rahaman et al., 2014). b) Phosphoric acid speciation in aqueous solutions (Hinsinger, 2001).

Additionally, some studies have shown that the initial stages of the reactions include the formation of a struvite precursor phase, as evidenced recently by Karafiludis et al. (2023a) for pure struvite and by Hövelmann et al. (2019a) for Co-containing struvite. Both these studies documented the existence of non-crystalline, spherical, nm-sized particles that formed prior to struvite crystallisation in aqueous solution at 20 °C. The presence of at least one precursor phase is further supported by the kinetic modelling done in the current study for the dataset at 37 °C, which suggested the best fit requires the inclusion of several chemical species as reaction steps (Fig. 3.3). This is also supported by the fact that both the pH and the turbidity curve development documented multiple steps in the reaction (Fig. 3.2). This behaviour of the turbidity and pH during struvite formation was previously documented by

Hövelmann et al. (2019a), who followed the struvite synthesis in aqueous solutions at 20 °C and whose data followed the same trends at concentrations of 6.1 and 3.05 mM. Similarly, Kabdaşlı et al. (2006) monitored the pH during struvite synthesis at 2.45 mM but in the presence of Ca²⁺ and Na⁺ ions and also documented similar pH profiles as in our current work.

3.5.2 Evaluation of kinetic parameters

Based on the analyses of the pH, turbidity and WAXS data sets presented above we obtained the reaction order n for the crystallisation of struvite (Tab. 3.1) and combined this with evaluations of the dominating growth mechanism and growth dimensionality as described in Hulbert (1969). Based on the calculations using the Avrami equation (Eq. 3.2), the reaction order values were higher than 0.5 for all experimental conditions. Such a value for n suggests a diffusion-dominated nucleation with either stagnating or deceleratory nucleation rate and a 1-dimensional crystal growth (Hulbert, 1969). A diffusion-dominated growth in this case would mean that the rate-limiting step of the reaction is the diffusion of growth units from the inner nuclei to the active surface site (Karpiński and Bałdyga, 2019). A diffusion-dominated mechanism for the nucleation of struvite was also suggested by Bouropoulos and Koutsoukos (2000). However, it is important to note that the n value can only give an indication of the nucleation mechanism, but ideally, such assertions would need independent complementary evidence for the interpretation. Such evidence could be information on the crystal morphology (Kasioptas et al., 2010), which in our case is evidenced by the SEM images, that show prismatic crystals that may have primarily grown into one direction (interpreted as 1-dimensional crystal growth) (Fig. 3.1, a). It also should be considered that the Avrami equation was originally developed for crystallisation from the melt and/or transformation and decomposition reactions in high-temperature systems (Hulbert, 1969), and thus its transferability and applicability to nucleation processes in aqueous solutions may be affected.

Nevertheless, the obtained activation energy value (17 kJ/mol) is somewhat lower, yet within the same order of magnitude as literature data that range from ~ 25 kJ/mol (Ariyanto et al., 2014; Ben Moussa et al., 2011) to ~ 56 kJ/mol (Polat and Sayan, 2020). However, the fit for the struvite activation energy in this current study (Fig. 3.5) was only moderately good (R^2 -value of ~ 0.6) because some data in the 25 and 37 °C experimental series were outliers.

3.5.3 Influence of concentration and temperature

The comparison of struvite formation kinetics, monitored by various analytical techniques, not surprisingly confirms that the formation of struvite becomes faster with increasing concentrations. The influence of supersaturation/concentration on the decrease of induction time with higher solution supersaturation closely resembles what has been reported in the literature (e.g., Hövelmann et al., 2019a; Le Corre et al., 2007a; Bouropoulos and Koutsoukos, 2000). An increase in supersaturation and,

corresponding, an increase in concentration is associated with a shift in the thermodynamic equilibrium to the product side according to Le Chatelier's principle, leading to a faster precipitation of the product struvite. However, the formation experiments at different temperatures revealed two contradicting findings: at constant supersaturation, the induction time decreased with elevating reaction temperatures from 5 to 25 °C, matching the known increasing solubility of struvite with temperature. A higher solubility leads to a lower tendency of a phase to precipitate from a saturated solution, which is shown through the increasing induction time at higher temperatures. Contrarily, the induction time increased from 25 to 37 °C in the turbidity and pH monitoring experiments (Fig. 3.2) at 5–15 mM. Further comparing these data sets is hindered by the fact that there are no systematic but contradictory datasets in the literature about the temperature-dependent struvite solubility. Some previous studies reported that the solubility of struvite increased with temperature (Crutchik and Garrido, 2016; Aage et al., 1997), while other solubility studies showed an increase in solubility up to 30 °C followed by a decrease up to 50 °C (Hanhoun et al., 2011; Bhuiyan et al., 2007). The results of the two latter studies match well the observations made in this study at lower concentrations (≤ 15 mM; Fig. 3.2, a, c). However, from the temperature-dependent WAXS measurements, this was not observed (Fig. 3.4). It may be that at a concentration of 30 mM, where the system is highly supersaturated and the reactions were extremely fast, the temperature effect was negligible, while the concentration/supersaturation controlled the reaction, in contrary to what was observed at lower concentrations/supersaturations. This was confirmed by the lab-scale experiments that showed a stronger temperature effect at lower supersaturations (Fig. 3.2).

3.5.4 Future indications

Although this will not be part of this thesis, further evaluation of the above-presented data sets and a more detailed comparison between kinetic modelling using the Avrami equation of the WAXS data and the Monte Carlo simulation applied to the pH data is planned. The aim is to model the reaction progress by a Monte Carlo simulation and derive further information on the kinetics of the crystallisation at different temperatures. Furthermore, any changes in nucleation and growth behaviour induced by changes in concentration/supersaturation can be derived from the pH datasets. Obtained k values will be used to determine the activation energy based on the pH data, which can be compared to the activation energy based on the WAXS data. This comparison will show the advantages and disadvantages of 1. using different types of data to evaluate the kinetics of crystallisation processes and 2. the application of two different models for determining kinetic parameters.

To summarise, this chapter details a systematic temperature- and concentration-dependent evaluation of the kinetics of struvite crystallisation from aqueous solution. The results show that the induction time strongly depends on solution concentration. The change in induction time with temperature is only

linear until 25 °C and shows a reverse dependency at higher temperatures. This may be a reflection of the change in struvite solubility with temperature, as previously suggested (Bhuiyan et al., 2007 and Aage et al., 1997). Furthermore, the Avrami equation was used for the first time to determine the reaction order n and rate constant k for the struvite system. Future modelling using a Monte Carlo simulation and comparing it to the approach using the Avrami equation will strengthen the outputs from this chapter.

Acknowledgements

The authors thank the beamline scientists at the I22 beamline, Diamond Light Source Facilities, Didcot, for their help in setting up the beamline for our experiments.

4 A new structure determination of the magnesium phosphate mineral struvite ($\text{MgNH}_4\text{PO}_4 \cdot 6\text{H}_2\text{O}$) at 100 K

This chapter is adapted from a data publication in *EarthArXiv* and *GFZ Data Publication Services*:

Volkman, R.; Münchhalfen, M.; Benning, L.G. (2024). A new structure determination of the magnesium phosphate mineral struvite ($\text{MgNH}_4\text{PO}_4 \cdot 6\text{H}_2\text{O}$) at 100 K.

Preprint available at: <https://doi.org/10.31223/X5KQ4F>

Data publication available at: <https://doi.org/10.5880/GFZ.3.5.2024.001>

4.1 Abstract

The magnesium phosphate mineral struvite ($\text{MgNH}_4\text{PO}_4 \cdot 6\text{H}_2\text{O}$) is of interest for the recovery of phosphorus from wastewater and for use as a fertiliser in agriculture, yet its structure is still debated. The structure of synthetic single crystals of struvite was characterised through the refinement of a single-crystal X-ray diffraction pattern acquired at 100 K, with the positions of all H atoms being identified through subsequent difference Fourier analyses. We show that the ionic interactions between the Mg^{2+} and NH_4^+ cations and the phosphate anions are reinforced by a three-dimensional network of hydrogen bonds of moderate strength. In contrast to the previously published struvite structure determined at room temperature, the ammonium groups do not rotate but are locked by three hydrogen bonds to neighbouring oxygen atoms. It is likely that the rotation of the NH_4^+ groups that occurs when approaching room temperature plays an essential role in the known decomposition of struvite to newberyite ($\text{MgHPO}_4 \cdot 3\text{H}_2\text{O}$), ammonia, and water.

4.2 Chemical context

The magnesium phosphate mineral struvite occurs naturally in P-rich soils (Teschemacher, 1846), in kidney stones comprising a sub-group called infection stones (Das et al., 2017), and as a common precipitate in wastewater pipelines. As P is a limited but crucial resource, research on the formation, stability and transformation of phosphate minerals such as struvite aims to provide new insights into rates and mechanisms for P recovery from wastewater and the use of such minerals as slow-release fertilisers in agriculture (Azam et al., 2019). The crystal structure of struvite has been determined at room temperature (Ferraris et al., 1986; Abbona et al., 1984; Whitaker and Jeffery, 1970a). However, struvite is unstable but information about both its formation and stability is lacking. Under atmospheric

conditions, struvite gradually decomposes into newberyite even at room temperature (Sutor, 1968; Whitaker, 1968), releasing NH_3 and H_2O , while at higher temperatures (e.g., 90°C), struvite decomposes and transforms to an amorphous high surface area material (Hövelmann et al., 2019b). In order to determine what controls the stability and induces the transformation of struvite at ambient conditions, we characterised crystals synthesised in an aqueous solution, and their crystal structure was determined with XRD carried out at 100 K.

4.3 Structural commentary

The crystal structure of struvite at 100 K was solved in the polar orthorhombic space group $\text{Pmn}2_1$ (for details, see Tab. 4.1). The positions of all hydrogen atoms were determined by difference Fourier analysis and refined using individual isotropic displacement parameters. The structure consists of octahedral $[\text{Mg}(\text{H}_2\text{O})_6]^{2+}$ complexes and tetrahedral PO_4^{3-} and NH_4^+ groups (Fig. 4.1), which are linked by ionic interactions reinforced by a three-dimensional network of hydrogen bonds. The Mg–O bond lengths vary between 2.048 Å and 2.107 Å, and the O–Mg–O angles deviate by up to about 5° from those of an ideal octahedron (Tab. 4.2). All water molecules of the $[\text{Mg}(\text{H}_2\text{O})_6]^{2+}$ complex are involved in strong hydrogen bonds to oxygen atoms of neighbored phosphate groups, which in turn are characterised by donor-acceptor distances of on average 2.65 Å (Tab. 4.3). The tetrahedral PO_4^{3-} group is only slightly distorted with mean P–O bond lengths and P–O–P angles of ~ 1.54 Å and $\sim 109.47^\circ$, respectively (Tab. 4.2). Charge compensation is achieved by NH_4^+ molecules located in the cavities between the $[\text{Mg}(\text{H}_2\text{O})_6]^{2+}$ and PO_4^{3-} groups (Fig. 4.1) and with the ammonium group connected to the phosphate group and the $[\text{Mg}(\text{H}_2\text{O})_6]^{2+}$ groups by hydrogen bonds of the type N–H1C \cdots O6 and N–H1D \cdots O2, respectively (Tab. 4.3 and Fig. 4.3). The latter hydrogen bond occurs twice due to symmetry. Therefore, the ammonium group is fixed in its position and does not rotate at 100 K.

4.4 Database survey

The crystal structure of struvite was first studied by Whitaker and Jeffery (1970a) at ambient temperatures using double-film equi-inclination Weissenberg photographic XRD, which at that time did not allow the determination of the positions of all H atoms. However, they presented evidence for the rotation of the ammonium group around a single bond (Whitaker and Jeffery, 1970b). Later, Abbona et al. (1984) employing XRD and Ferraris et al. (1986) using neutron diffraction improved the knowledge of the arrangement of hydrogen atoms in struvite and suggested that at room temperature, the ammonium group is ordered and linked by one single and several polyfurcated N \cdots O bonds.

Regarding the positions of non-hydrogen atoms and considering thermal expansion effects, our results at 100 K agree well with literature data at room temperature. The determined hydrogen bond lengths are in good agreement with Abbona et al. (1984) but are $\sim 0.1 \text{ \AA}$ shorter than the bond lengths reported by Ferraris et al. (1986). The temperature factors for water H atoms are improved by $\sim 0.38 \text{ \AA}^2$, compared to Abbona et al. (1984). Especially the thermal parameters of the hydrogen atoms of the ammonium group atoms are reduced by up to $\sim 0.04 \text{ \AA}^2$ compared to the U_{iso} values derived by Ferraris et al. (1986). Furthermore, Ferraris et al. (1986) also mention the connection of the NH_4^+ group by only one single hydrogen bond and describe the other $\text{N}\cdots\text{O}$ bonds as polyfurcated. We could not confirm the Ferraris et al. (1986) arrangement by our structure solution, but our description of the hydrogen bonding network agrees well with Abbona et al. (1984).

In summary, we show that the locking of the NH_4^+ group by several H–bonds at 100 K gives evidence to the increased stability of struvite at temperatures below 273 K. With increasing temperature, the weakening of the $\text{N–H1D}\cdots\text{O2}$ bond likely initiates a possible bouncing rotation of the NH_4^+ group that leads eventually to the decomposition of struvite.

4.5 Synthesis and crystallisation

Struvite was synthesised using a counter-diffusion crystallisation method according to Hövelmann et al. (2019a): 1.0 M solutions of $(\text{NH}_4)_2\text{HPO}_4$ and $\text{MgCl}_2 \cdot 6\text{H}_2\text{O}$ were filled separately into 100 ml glass beakers up to their rims. They were placed at opposite sides of a 6 l plastic box. This box was then filled with de-ionized Milli-Q water until the two beakers were fully immersed. Finally, the box was closed with a lid to avoid evaporation. Crystals started to form at the bottom of the plastic container and at the outlets of the two beakers after a few days and had been left to grow for about two weeks until they reached sizes of several millimetres. Thereafter, the crystals were removed from the solution, rinsed with Milli-Q water and dried in air at 295 K (22 °C) for 2 h until stored in plastic membrane boxes in a fridge at 273 K (0 °C).

4.6 Refinement

Crystal data, data collection, and structure refinement details are summarised in Table 4.1. All non-hydrogen atoms were refined anisotropically. Hydrogen atom positions were identified by difference Fourier analysis and refined using the riding model. $\text{N}\cdots\text{H}$ and $\text{O}\cdots\text{H}$ bond distances were refined using similarity restraints. The refinements were conducted using SHELXL (Sheldrick, 2015).

Tab. 4.1 Experimental details.

| Crystal data | strv_unaltered |
|--|---|
| Chemical formula | $\text{H}_{12}\text{MgO}_6 \cdot \text{O}_4\text{P} \cdot \text{H}_4\text{N}$ |
| M_r | 245.42 |
| Crystal system, space group | Orthorhombic, $Pmn2_1$ |
| Temperature (K) | 100 |
| a, b, c (Å) | 6.9484 (2), 6.1038 (2), 11.1930 (5) |
| V (Å ³) | 474.71 (3) |
| Z | 2 |
| Radiation type | Mo $K\alpha$ |
| μ (mm ⁻¹) | 0.39 |
| Crystal size (mm) | 0.22 × 0.14 × 0.08 |
| Data collection | |
| Diffractometer | XtaLAB Synergy, Dualflex, Pilatus 300K |
| Absorption correction | Gaussian <i>CrysAlis PRO</i> 1.171.41.119a (Rigaku Oxford Diffraction, 2021) Numerical absorption correction based on Gaussian integration over a multifaceted crystal model. Empirical absorption correction using spherical harmonics as implemented in SCALE3 ABSPACK scaling algorithm |
| T_{\min}, T_{\max} | 0.609, 1.000 |
| No. of measured, independent and observed [$I > 2\sigma(I)$] reflections | 13014, 2424, 2241 |
| R_{int} | 0.047 |
| $(\sin \theta/\lambda)_{\text{max}}$ (Å ⁻¹) | 0.833 |

| Crystal data | strv_unaltered |
|---|--|
| Refinement | |
| $R[F^2 > 2\sigma(F^2)], wR(F^2), S$ | 0.028, 0.066, 1.02 |
| No. of reflections | 2424 |
| No. of parameters | 106 |
| No. of restraints | 7 |
| H-atom treatment | All H-atom parameters refined |
| $\Delta\rho_{\max}, \Delta\rho_{\min}$ (e Å ⁻³) | 0.45, -0.28 |
| Absolute structure | Flack x determined using 984 quotients [(I+)-(I-)]/[(I+)+(I-)] (Parsons et al., 2013). |
| Absolute structure parameter | -0.04 (5) |

Tab. 4.2 Bond lengths and angles of non-hydrogen bonds (Å, °).

| Atoms | Length | Atoms | Angle |
|---------------------|------------|--------------------------------------|-----------|
| P1–O5 | 1.5425(15) | O5–P1–O6 | 109.67(9) |
| P1–O6 | 1.5478(16) | O7–P1–O5 | 108.68(5) |
| P1–O7 ¹ | 1.5413(11) | O7–P1–O5 | 108.67(5) |
| P1–O7 | 1.5413(11) | O7–P1–O6 | 109.49(6) |
| | | O7–P1–O6 | 109.49(6) |
| | | O7–P1–O7 ¹ | 110.82(8) |
| Mg1–O1 ² | 2.0477(14) | O1–Mg1–O1 ² | 89.36(8) |
| Mg1–O1 | 2.0477(14) | O1 ² –Mg1–O2 ² | 87.70(5) |
| Mg1–O2 | 2.0744(12) | O1–Mg1–O2 ² | 176.62(6) |
| Mg1–O2 ² | 2.0744(12) | O1–Mg1–O2 | 87.70(5) |

| Atoms | Length | Atoms | Angle |
|--------|------------|-------------------------|-----------|
| Mg1–O3 | 2.1070(19) | O1 ² –Mg1–O2 | 176.62(7) |
| Mg1–O4 | 2.1028(19) | O1 ² –Mg1–O3 | 89.34(6) |
| | | O1–Mg1–O3 | 89.34(6) |
| | | O1–Mg1–O4 | 90.36(6) |
| | | O1 ² –Mg1–O4 | 90.36(6) |
| | | O2–Mg1–O2 ² | 95.19(7) |
| | | O2–Mg1–O3 | 88.96(5) |
| | | O2 ² –Mg1–O3 | 88.96(5) |
| | | O2–Mg1–O4 | 91.32(5) |
| | | O2 ² –Mg1–O4 | 91.32(5) |
| | | O4–Mg1–O3 | 179.59(9) |

¹1-x,+y,+z; ²-x,+y,+z

Tab. 4.3 Hydrogen-bond geometry (Å, °).

| <i>D</i> –H [⋯] <i>A</i> | <i>D</i> –H | H [⋯] <i>A</i> | <i>D</i> ⋯ <i>A</i> | <i>D</i> –H [⋯] <i>A</i> |
|---------------------------------------|-------------|-------------------------|---------------------|-----------------------------------|
| O4–H4A [⋯] O5 ⁱ | 0.83 (3) | 1.85 (3) | 2.672 (2) | 178 (4) |
| O1–H1A [⋯] O7 ⁱⁱ | 0.83 (2) | 1.84 (2) | 2.6477 (14) | 164 (3) |
| O1–H1B [⋯] O5 | 0.81 (2) | 1.82 (2) | 2.6225 (15) | 170 (3) |
| O2–H2A [⋯] O6 | 0.83 (2) | 1.88 (2) | 2.6936 (16) | 166 (3) |
| O2–H2B [⋯] O7 ⁱⁱⁱ | 0.84 (2) | 1.81 (3) | 2.6310 (17) | 168 (3) |
| O3–H3 [⋯] O7 | 0.86 (3) | 1.79 (3) | 2.6496 (14) | 175 (3) |
| N1–H1C [⋯] O6 | 0.93 (2) | 1.85 (2) | 2.785 (3) | 180 (3) |
| N1–H1D [⋯] O2 ^{iv} | 0.91 (2) | 2.11 (2) | 2.971 (2) | 158 (2) |
| N1–H1E [⋯] O1 ⁱⁱⁱ | 0.92 (3) | 2.55 (4) | 3.150 (2) | 123 (3) |
| N1–H1E [⋯] O1 ^v | 0.92 (3) | 2.55 (4) | 3.150 (2) | 123 (3) |

¹1/2-x,-y,1/2+z; ²+x,-1+y,+z; ³1/2-x,1-y,1/2+z; ⁴1-x,1+y,+z; ⁵1/2+x,1-y,1/2+z

Tab. 4.4 Fractional Atomic Coordinates ($\times 10^4$) and Equivalent Isotropic Displacement Parameters ($\text{\AA}^2 \times 10^3$). U_{eq} is defined as 1/3 of the trace of the orthogonalised U_{ij} .

| Atom | x | y | z | U_{eq} |
|------|------------|------------|------------|-----------------|
| P1 | 5000 | 4993.9(8) | 3945.9(5) | 6.41(9) |
| O5 | 5000 | 2679(2) | 3393.3(15) | 9.4(2) |
| O6 | 5000 | 4818(2) | 5325.4(15) | 9.5(3) |
| O7 | 3174.0(15) | 6209.3(16) | 3531.3(11) | 9.42(18) |
| Mg1 | 0 | 1286.9(12) | 5223.1(7) | 7.78(13) |
| O1 | 2072.2(16) | 250.8(17) | 4051.5(14) | 13.1(2) |
| O2 | 2204.4(16) | 2370.5(19) | 6324.4(10) | 11.0(2) |
| O3 | 0 | 4372(3) | 4378.2(17) | 15.0(3) |
| O4 | 0 | -1803(3) | 6054.2(16) | 15.0(3) |
| N1 | 5000 | 8724(3) | 6611.2(19) | 13.9(3) |

Tab. 4.5 Anisotropic thermal displacement parameters (\AA^2) ($\times 10^4$). The anisotropic displacement factor exponent takes the form: $-2\pi^2[h^2a^{*2} \times U_{11} + \dots + 2hka^* \times b^* \times U_{12}]$.

| Atom | U_{11} | U_{22} | U_{33} | U_{23} | U_{13} | U_{12} |
|------|----------|----------|----------|----------|----------|----------|
| P1 | 6.25(17) | 6.04(17) | 6.94(19) | 0.08(16) | 0 | 0 |
| O5 | 10.7(6) | 6.7(5) | 10.6(6) | -1.9(5) | 0 | 0 |
| O6 | 10.9(6) | 10.7(6) | 7.0(6) | 0.2(5) | 0 | 0 |
| O7 | 7.3(4) | 9.7(4) | 11.3(5) | 1.0(4) | -0.8(3) | 1.5(3) |
| Mg1 | 7.6(3) | 7.6(3) | 8.2(3) | -0.1(2) | 0 | 0 |
| O1 | 11.4(4) | 9.9(4) | 18.1(6) | -2.8(5) | 5.4(4) | -0.7(3) |

| Atom | U ₁₁ | U ₂₂ | U ₃₃ | U ₂₃ | U ₁₃ | U ₁₂ |
|------|-----------------|-----------------|-----------------|-----------------|-----------------|-----------------|
| O2 | 10.6(5) | 13.1(5) | 9.4(5) | -0.7(4) | 0.1(4) | -2.1(3) |
| O3 | 7.9(6) | 13.6(7) | 23.4(9) | 7.6(6) | 0 | 0 |
| O4 | 25.5(9) | 9.0(7) | 10.7(7) | 1.3(5) | 0 | 0 |
| N1 | 14.0(8) | 13.1(8) | 14.7(9) | -2.3(6) | 0 | 0 |

Figures

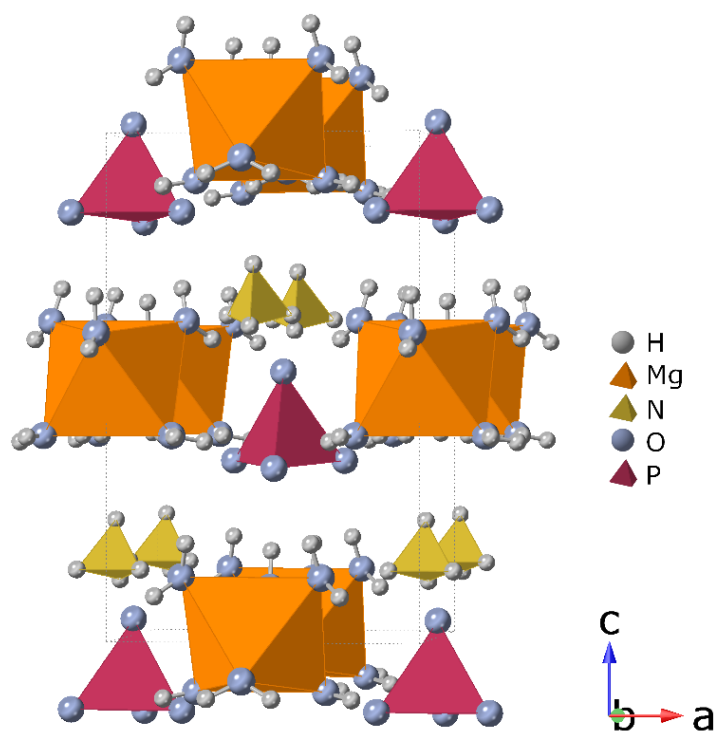


Fig. 4.1 Polyhedral model of the struvite crystal structure approximately along *b*. Figure created with CrystalMaker (Palmer, 2014).

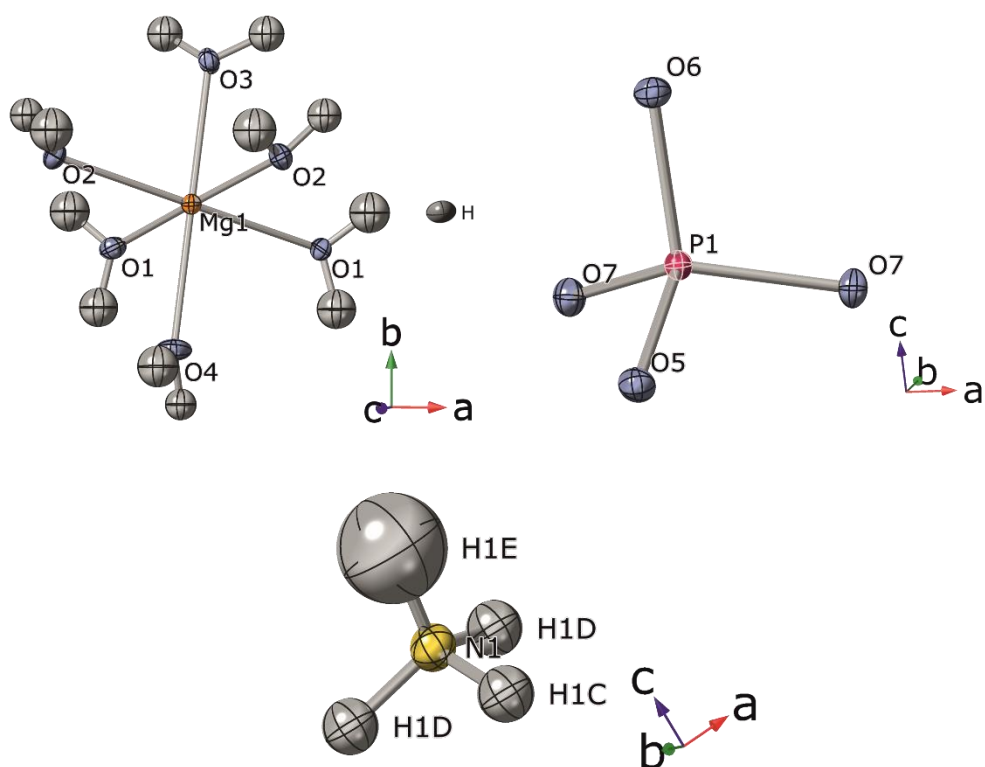


Fig. 4.2 Ellipsoidal models and coordination environment of single structural components of the struvite structure at 100 K. Ellipsoids are modelled with a 50 % probability. Figure created with CrystalMaker (Palmer, 2014).

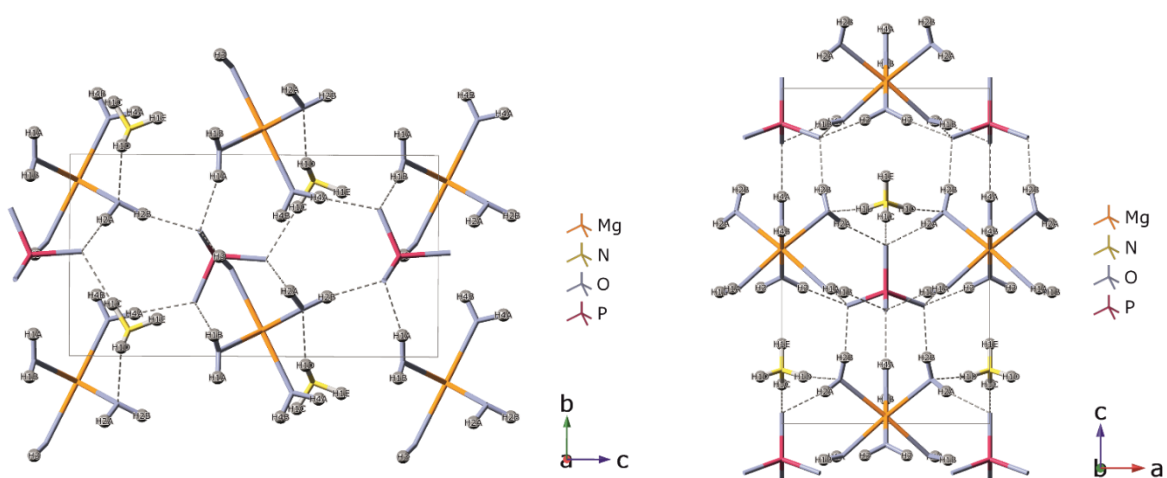


Fig. 4.3 Network of hydrogen bonds in struvite. Projection of structure at 100 K along a (left) and along b (right). Figure created with CrystalMaker (Palmer, 2014).

5 The transformation of magnesium phosphate minerals at atmospheric conditions – A kinetic and mineralogical study with environmental applications

This chapter is adapted from a manuscript submitted to *American Mineralogist*:

Volkman, R.; Blukis, R.; Schmidt, C.; Forjan, P.; Benning, L.G. The Transformation of Magnesium Phosphate Minerals at Atmospheric Conditions – A Kinetic and Mineralogical Study with Environmental Applications

5.1 Abstract

Struvite ($\text{MgNH}_4\text{PO}_4 \cdot 6\text{H}_2\text{O}$), a magnesium phosphate mineral, is a promising recoverable P and N source and is employed as a slow-release agricultural fertiliser. However, struvite is unstable in air and transforms into two distinct crystalline phases - newberyite ($\text{MgHPO}_4 \cdot 3\text{H}_2\text{O}$) and dittmarite ($\text{MgNH}_4\text{PO}_4 \cdot \text{H}_2\text{O}$), before breaking down into an amorphous phase. Because the transformation rates and mechanisms are unknown, we present complementary X-ray diffraction, Raman and microscopic data from which we determined the temperature-dependent (21–60 °C) kinetics and mechanisms for the transformation and breakdown of struvite. Our results revealed that its transformation into both newberyite and dittmarite follows a coupled dissolution-reprecipitation mechanism, with the reaction kinetics being dominated by the diffusion of H_2O and NH_3 out of the struvite structure. The reaction pathways proved to be temperature-dependent, with newberyite being the only transformation product at room temperature even after 10 months, a transformation resulting from the loss of ammonia and three of the six water molecules. On the contrary, at higher temperatures, dittmarite is the major transformation product of struvite, forming through the release of five of the six molecules of water, but retaining its ammonia. At 60 °C and after 3 months, dittmarite breaks down into an amorphous magnesium phosphate phase. This study provides comprehensive insights into the kinetics and the underlying processes governing the transformation of struvite. These findings have significant implications for the long-term storage of struvite, and its subsequent utilisation as a slow-release fertiliser.

5.2 Introduction

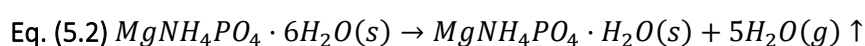
Struvite, a magnesium phosphate mineral, is found in various natural and anthropogenic settings, including guano deposits (MacIvor, 1887; Teschemacher, 1846), encrustations in wastewater pipelines

(Kumar and Pal, 2015), and as a component of urinary infection stones in the human body (Manzoor et al., 2018a). Struvite is recognised as a sustainable source of P and N for agriculture. Notably, struvite recovered from wastewater is employed as a slow-release fertiliser (Azam et al., 2019; Kataki et al., 2016b; Le Corre et al., 2009).

It is widely accepted that struvite is not thermodynamically stable under ambient conditions (25 °C, 1 bar). Several studies have documented the transformation of struvite into other phosphate phases both in aqueous media and air. For example, Sutor (1968) observed that various-sized struvites from urinary infection stones began to decompose in air after 6 days, fully transforming into newberyite after 6–10 months, a trend confirmed by Whitaker (1968). These findings suggest that newberyite may be a secondary phase formed only after removing the infection stone from the human body rather than being precipitated simultaneously with struvite during the infection stone formation. The proposed breakdown reaction (Paul et al., 2002) is:



Conversely, other studies documented that when struvite was reacted in aqueous solutions at temperatures between 100–200 °C, it transformed into dittmarite (Ramlogan and Rouff, 2016; Sarkar, 1991) and not newberyite. At higher temperatures and alkaline conditions (60–120 °C and pH 9–10), Bayuseno and Schmahl (2020) formed dittmarite alongside struvite. Farhana (2016) found that dittmarite was formed from struvite when heated in humid air (95 % relative humidity) at temperatures ≥ 65 °C. The formation of dittmarite during struvite heating is marked by the release of five molecules of water, whereas ammonium stays in the structure (Ramlogan and Rouff, 2016; Abdelrazig and Sharp, 1988) following the reaction:



The decomposition of struvite in air at temperatures between 50–725 °C revealed a transformation to either amorphous magnesium hydrogen phosphate ($MgHPO_4$) (Hövelmann et al., 2019b; Novotny, 2011; Sarkar, 1991) or to low-crystalline $MgHPO_4$ (Chen et al., 2015) and/or to magnesium pyrophosphate ($Mg_2P_2O_7$) via newberyite (Paul et al., 2002). Studies focusing on the transformation occurring at ambient temperatures, akin to those prevalent in environments where struvite might be employed as an agricultural fertiliser, are limited. Furthermore, many of these studies only evaluated the transformation's initial and end-products and did not evaluate the kinetics or mechanisms of the struvite transformations.

In order to fill this knowledge gap and to comprehensively characterise the time-resolved decomposition of struvite, we monitored its transformation to newberyite and dittmarite at temperatures between 22–60 °C in air for up to 10 months. We derived the kinetic parameters

associated with these dry transformations and evaluated the accompanying macro- to microscopic morphological and textural changes. Our findings bear significance in the context of the storage of struvite intended to be used as a slow-release fertiliser because the transformation of struvite through the loss of ammonia and water alters its composition and properties, and thus its efficiency as a dual N- and P-containing fertiliser.

5.3 Methodology

5.3.1 Starting materials and experiments

We monitored the transformation of synthetic struvite in air using two different grain sizes:

Struvite powders were synthesised at 22 °C, 1 atm and 42 % relative humidity by mixing $(\text{NH}_4)_2\text{HPO}_4$ (Sigma-Aldrich, ≥ 98 % purity) and $\text{MgCl}_2 \cdot 6\text{H}_2\text{O}$ (Honeywell Fluka, ≥ 98 % purity) solutions following Hövelmann et al. (2019a). In brief, a 0.1 M $(\text{NH}_4)_2\text{HPO}_4$ solution was mixed under constant stirring (400 rpm) with a 0.1 M $\text{MgCl}_2 \cdot 6\text{H}_2\text{O}$ solution in a 1:1 volume ratio. This led to the immediate formation of a white precipitate. The mixture was continuously stirred for 3 h, after which it was allowed to react further without stirring for an additional 24 h. The resulting material was vacuum filtered through 0.2- μm polycarbonate membrane filters, and the resulting powder dried in air for 2 h. The final product was a white powder that when observed by optical microscopy, contained crystals with average crystal sizes ranging between 10–30 μm . The so produced powders were stored in closed glass vials at 0 °C for a maximum of 10 days prior to further use.

mm-sized struvite single crystals were produced using the counter-diffusion method described in Hövelmann et al. (2019a). Two 100 mL glass beakers filled up to their rims with 1.0 M solutions of $(\text{NH}_4)_2\text{HPO}_4$ and $\text{MgCl}_2 \cdot 6\text{H}_2\text{O}$, respectively, were placed at the opposite sides of a 6-litre plastic container, fully filled with de-ionised Milli-Q water. The container was sealed to prevent evaporation. The system was left to react at room temperature for two weeks, during which time crystals up to a size of several mm grew at the bottom of the plastic container and on the rims of the two beakers. The crystals were rinsed with Milli-Q water and air-dried at 22 °C for 2 h and subsequently stored in plastic membrane boxes at 0 °C.

The transformation of both the struvite powders and the single crystals was followed by reacting both materials in air at temperatures of 22, 37 and 60 °C for up to 10 months (40 weeks) (see App. B, Tab. B1 for full details). For the transformation at 22 °C, the samples were placed in 10 mL glass vials that were stored open in a drawer. Experiments at 37 and 60 °C were conducted by putting the samples inside Pyrex glass tubes that were heated in block heaters. At 37 °C, samples were reacted in a Stuart Block Heater (Model SBH200D), which offered temperature stability/homogeneity of ± 0.1 °C, while at 60 °C,

transformations were carried out using either an IKA or a VWR Dry Block Heater, with temperature stabilities of ± 0.4 – 0.5 and homogeneity of ± 0.2 – 0.6 °C. After heat treatment, every sample was allowed to cool for 10 min, after which they were stored at 0 °C until further analysis was carried out, usually immediately after removal from the reaction conditions. At the end of the experiments, the mm-sized crystals were prepared as 30 and 100 μm -thick uncovered thin sections for optical microscopy and vibrational spectroscopy methods.

5.3.2 Sample characterisation

The changes in mineralogical characteristics were evaluated using powder XRD. The as-synthesised initial samples and the reaction end products were ground in an agate mortar, filled into 0.5 mm glass capillaries (special glass, “Lindemann type”, Hilgenberg) and analysed on a Stoe StadiP diffractometer. We used a Cu K α source operating at 40 kV and 40 mA and collected data over the 2θ range of 0–84 ° using a step size of 0.015 ° and a counting time of 32 s per step. The data was averaged over 18 repetitions (more information on the XRD instrument properties and refinement statistic indicators can be found in App. B, Tab. B2). The collected data were processed through Rietveld analysis, and the phase identification and quantification were done with the GSAS-II software (B.H. Toby and R.B. Von Dreele, 2013) using the following published reference crystal structures: Volkmann et al. (2024) for struvite; Abbona et al. (1979) for newberyite, and Frazier et al. (1966) for dittmarite.

To monitor the changes in appearance and structure of the altered single crystals and the end product powders, we imaged our materials post-reaction with no further treatment using both a binocular and a transmitted light microscope (Carl Zeiss Stemi 305 binocular and Carl Zeiss Jenapol). Higher resolutions were acquired using an SEM (FEI Quanta 3D Dual Beam) coupled with an energy-dispersive spectrometer. Struvite is highly unstable under vacuum (Hövelmann et al., 2019a). Thus, all SEM images were done at low vacuum (1 bar), at voltages between 5–20 kV, and using a 4 nA current setting. All images were taken using back-scattered electron (BSE) mode. All single crystals or powders were mounted on aluminium stubs using carbon films, and measurements were carried out without coating. However, copper bridges were used to mount the samples to prevent charging.

Distinguishing between struvite, newberyite, and dittmarite based solely on light microscopy has proved to be challenging because all these phases show similar optical properties. We chemically differentiated between these phases based on the different ammonia and water contents by Raman microspectroscopy (Horiba Jobin Yvon LabRAM HR 800 VIS, at 473nm) and by bulk Fourier transform infrared spectroscopy (FTIR, Thermo Fisher Nicolet iS5 single bounce diamond ATR, resolution 4 cm^{-1}) analyses. The FTIR measurements were conducted on mm-sized unaltered as well as on crystal samples altered for 6 months at 60 °C while Raman analyses were carried out on unreacted and reacted single crystals and additional 100 μm thin sections prepared of selected single crystals. Detailed instrument

and analysis parameters for both vibrational spectroscopy techniques can be found in Appendix B, Table B3. Sample spectra were compared with reference spectra for struvite and newberyite from the RRUFF database (Frost et al., 2005 and Stefov et al., 2004 for struvite; Frost et al., 2012 for newberyite). Vibrational patterns for dittmarite are not available in the literature.

To obtain the kinetic parameters describing the transformation between phases in our time-resolved reactions, we fitted the change in phase quantities derived from Rietveld analysis using the Avrami equation, also known as Johnson-Mehl-Avrami-Kolmogorow (JMAK) equation (Lasaga, 1998; Avrami, 1940, 1939) (Eq. 5.3, in linear form in Eq. 5.4):

$$\text{Eq. (5.3)} \quad \alpha = 1 - e^{-k(t-t_0)^n}$$

$$\text{Eq. (5.4)} \quad \ln[-\ln(1 - \alpha)] = n \ln t + \ln k$$

where α represents the reaction progress, t is the time (in s), and t_0 stands for the induction time (in s). n describes the growth dimensionality constant, and k is the rate constant (in s^{-1}) (Hulbert, 1969). Further details about the approach taken are given in Appendix B, Text B1.

5.4 Results

Our XRD patterns confirmed the identity of the synthesised unreacted powder and single crystal samples as pure struvite, with the diffraction patterns closely matching the reference patterns in the literature (Volkman et al., 2024; Ferraris et al., 1986; Whitaker and Jeffery, 1970a).

5.4.1 XRD-derived solid-phase quantification and transformation kinetics

The diffraction patterns of struvite samples exposed to air at 22 °C for between 1 h and 40 weeks revealed a progressive increase of newberyite besides the original struvite (Fig. 5.1, a). The formation of newberyite was evidenced in the diffraction patterns through the growth of (111), (020), (021), (102) and (221) Bragg peaks (Fig. 5.1, a).

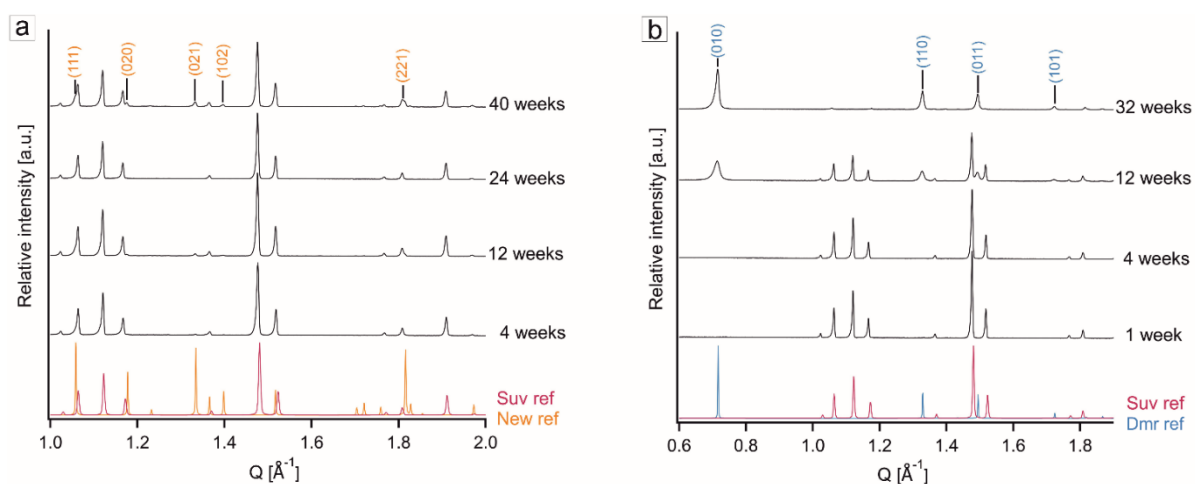


Fig. 5.1 XRD patterns of powder samples transformed at a) 22 °C and b) 37 °C over time. The peaks corresponding to struvite are red, while the newberyite peaks are orange and dittmarite peaks are blue. Abbreviations: Suv: Struvite; New: Newberyite; Dmr: Dittmarite.

Our analyses showed that after 3 days, ~ 5 wt% of the sample had transformed to newberyite (Fig. 5.2), which steadily increased to ~ 14 wt% after 40 weeks, with the remainder still being struvite. At higher temperatures, the transformation to newberyite was faster and far less long-lived. At 37 °C, newberyite remained a minor (max. ~ 12 wt%) phase characterised by broad and low-intensity diffraction peaks (Fig. 5.2 and App. B, Fig. B1). In comparison, at 60 °C, the newberyite fraction only reached a maximum of ~ 6 wt% after 1 week. It decreased again to 0 wt% after ~ 12 weeks, as characterised by Bragg peaks of low intensity (Fig. 5.2 and App. B, Fig. B2).

At temperatures ≥ 37 °C, dittmarite, confirmed through its strong (010), (110), and (101) diffraction peaks (Fig. 5.1, b), appeared progressively. The fraction of dittmarite increased continuously with temperature as struvite was exposed to air. The first occurrence of dittmarite at 37 °C was observed after 12 weeks (~ 12 wt%; Fig. 5.1, b; Fig. 5.2), while after 40 weeks of interaction, the altered sample contained ~ 78 wt% dittmarite, ~ 10 wt% struvite and ~ 12 wt% newberyite (Fig. 5.2). At 60 °C, the dominance of dittmarite in the altered sample was even more evident; with the first peaks appearing after just 20 h of interaction. After 1 week at 60 °C, the sample consisted almost exclusively of dittmarite (~ 95 wt%) (Fig. 5.2; App. B, Fig. B3). Noteworthy was the fact that in the XRD patterns of samples reacted at temperatures > 22 °C, a noticeable broadening of the struvite and newberyite peaks was observed after 12 and 40 weeks of interaction at 37 °C, respectively. This process occurred even earlier when the interaction temperature was 60 °C, with struvite peaks broadening and their intensity or peak areas decreasing until absent already after 5 days of interaction. Similarly, at 60 °C, dittmarite was also not detectable anymore after 12 weeks in air (Fig. 5.2).

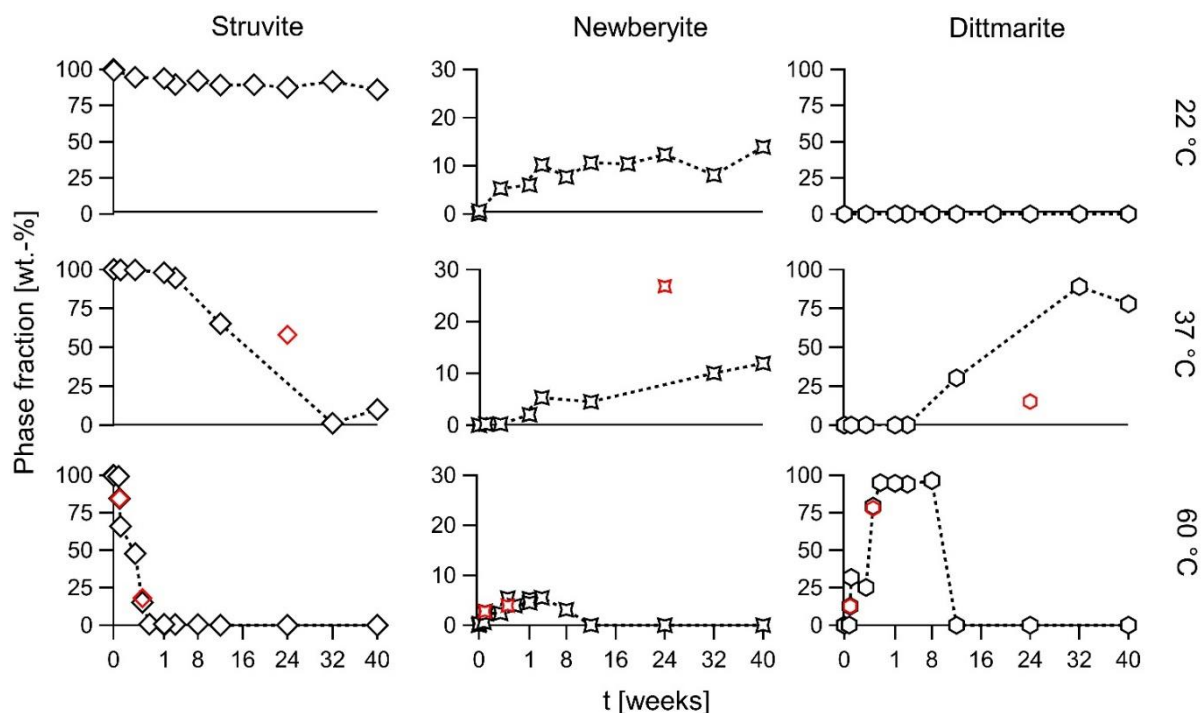


Fig. 5.2 Development of struvite, newberyite and dittmarite weight fractions in powder samples versus time, derived from Rietveld refinements of XRD patterns. Red outlier data points were excluded from the kinetic calculations.

Using the Avrami equation, we evaluated the reaction progress and derived the reaction orders n and the rate constants k for both transformations (struvite \rightarrow newberyite and struvite \rightarrow dittmarite) at each temperature. The reaction order of the reaction struvite \rightarrow newberyite varied from 0.3 to 0.5, with the rate constant varying between $0.5 \cdot 10^{-4}$ – $8.1 \cdot 10^{-4} \text{ s}^{-1}$ (Tab. 5.1) depending on the specific temperature conditions. The reaction order for the formation of dittmarite at 60 °C closely mirrored that of newberyite. However, the rate constant for dittmarite at 60 °C was notably higher, with a value of $2.9 \cdot 10^{-3} \text{ s}^{-1}$ (Tab. 5.1). At 37 °C, dittmarite formation only began after an induction period of 12 weeks (Fig. 5.2). Consequently, a limited dataset comprising only three data points was available for calculating both the n and k for this reaction (24 weeks, 32 weeks, 40 weeks). Due to this limited data, the values for this particular reaction are estimates and were therefore excluded from further analysis.

Tab. 5.1 Reaction orders and rate constants calculated for single-phase transformations at different temperatures. Values were rounded to one digit.

| Phase formation | Temperature [°C] | n | k [s ⁻¹] | R ² |
|-----------------|------------------|-----------|---|----------------|
| Newberyite | 22 °C | 0.3 ± 0.1 | 8.1·10 ⁻⁴ ± 2.0·10 ⁻⁴ | 0.9 |
| | 37 °C | 0.5 ± 0.3 | 0.5·10 ⁻⁴ ± 0.4·10 ⁻⁴ | 0.89 |
| | 60 °C | 0.4 ± 0.2 | 1.3·10 ⁻⁴ ± 0.5·10 ⁻⁴ | 0.77 |
| Dittmarite | 37 °C | n.d. | n.d. | – |
| | 60 °C | 0.5 ± 0.3 | 2.9·10 ⁻³ ± 1.2·10 ⁻³ | 0.8 |

5.4.2 Microscopic features documenting the phase transformations

Optical and electron microscopy imaging of the pristine and altered mm-sized single crystals allowed us to follow the morphological and textural evolution of the samples. Pristine struvite crystals appeared colourless and translucent and were characterised by their predominant tabular to prismatic crystal morphology (App. B, Fig. B4). The crystals showed frequent twinning, with butterfly-shaped aggregates as previously shown for similarly grown struvite crystals (Hövelmann et al., 2019a).

Samples reacted at 22 °C for 4 weeks revealed a new phase (Phase I) on the crystal surfaces. This phase initially grew at (or near) the edges, at cleavage planes and within small fractures initially present on the surface of the parent struvite. After 12 weeks, the new phase developed into 50–100 µm-sized rounded spots (Fig. 5.3, b; App. B, Fig. B4). The size of these spots increased to 100–200 µm after 24 weeks and to 200–400 µm after 40 weeks, often traversed by fractures (Fig. 5.3, a, b, c). SEM images revealed that these rounded spots consisted of prismatic to needle-shaped crystals, each measuring 5–15 µm, growing radially outward from a central point (Fig. 5.3, d). Interestingly, the interface between the new growing crystals and the parent struvite exhibited a µm-sized gap (Fig. 5.3, e), and the rounded spots contained fractures that radiated from the spot centres (Fig. 5.3, f).

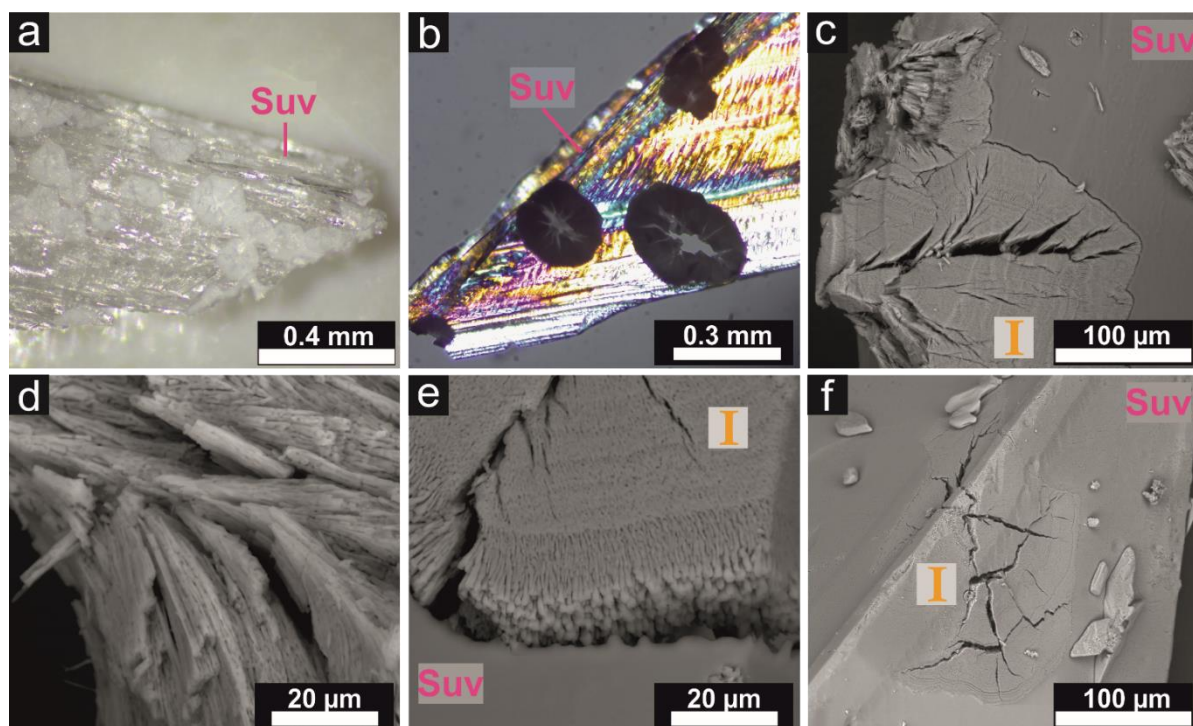


Fig. 5.3 a) Struvite crystal altered at 22 °C for 40 weeks showing hexagonal, opaque phases in the optical microscopic images. b) Crystal shown in a) under transmitted light with crossed polarisers showing the host crystal with opaque, fractured phases. c) SEM image of radially oriented crystals (Phase I) with fractures in the same sample shown in b). d) Close-up of the marked area in c). e) Phase-boundary between the new phase (Phase I) and struvite with a μm -sized gap in the same sample shown in b). f) Struvite crystal altered at 37 °C for 40 weeks with hexagonal structures (Phase I). Abbreviations: Suv: Struvite.

The above-described observations at 22 °C were also notable in the crystals altered at 37 °C, where rounded spotty patches with high refractive index under the transmitted light microscope were found on the host crystals' surfaces after 1 week of air exposure. After 40 weeks, the crystals were largely covered by the newly formed phases (App. B, Fig. B5). BSE-SEM imaging showed inhomogeneities in the struvite's crystal surfaces, expressing in elemental contrast in many areas of the samples. They were in the form of irregular grainy patterns or were found to have clear-lined, rectangular shapes (App. B, Fig. B6).

Alteration of the single crystal struvite samples at 60 °C invariably also led to the development of rounded, opaque patches (Fig. 5.4, a) that were observed already after 1 d of reaction – matching the powdered sample XRD data (Fig. 5.2). When examined under the SEM, two newly-formed phases that could be clearly distinguished based on their crystal morphology, texture and elemental contrast were observed. One phase (Phase II), which looked different from Phase I observed at 22 °C samples, formed a distinct layer with, at times, tabular-shaped crystals on the host crystal's surface (Fig. 5.4, b, c). Struvite crystals altered for 1 week appeared carpeted entirely by the two new phases (Fig. 5.4, d). Yet, the original external morphology of the struvite crystals was maintained throughout the whole process, resulting in a typical pseudomorphic overgrowth. At higher resolution, Phase II consisted of 10 μm -sized

crystals with a prismatic habit and no apparent relationships to the original struvite substrate (Fig. 5.4, e, f). The formation of this phase was not observed on struvite surfaces at lower temperatures. The other phase (Phase I) closely resembled what was observed in the SEM on struvite crystals transformed at lower temperatures (22 and 37 °C). It consisted of elongated crystals with an acicular habit and radial growth (Fig. 5.4, e, f). The crystals' size was difficult to determine due to areas with a less-developed crystallinity within the radial structures (Fig. 5.4, f). It is important to note that, throughout the process, the homogeneous struvite surfaces became entirely covered by the two polycrystalline phases, which hosted a significant amount of porosity (Fig. 5.4, e, f).

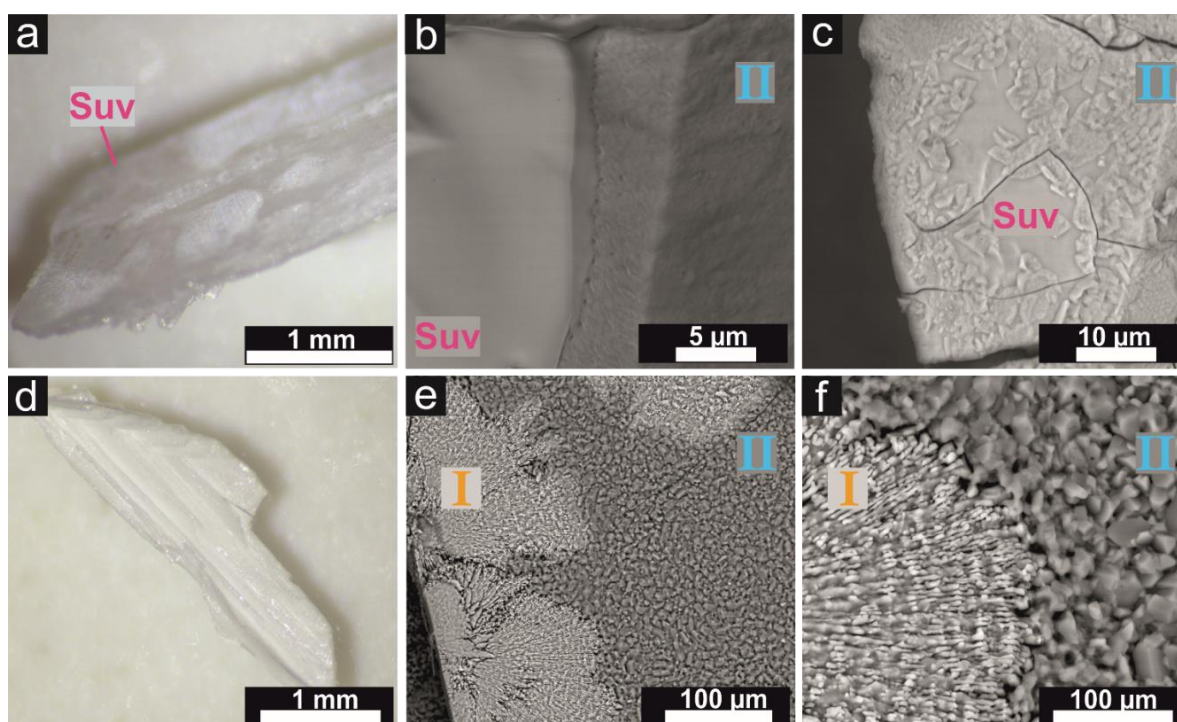


Fig. 5.4 a) Struvite crystal altered at 60 °C for 1 day. b) SEM image of a struvite host crystal altered at 60 °C for 3 days with a layer of a newly formed phase (Phase II). c) Surface of another crystal interacting with air for 3 days showing tabular-shaped phases (Phase II). d) Struvite crystal altered at 60 °C for 1 week with e) SEM image showing similar structures as observed at lower temperatures with the marked Phase II and II. f) Close-up of image e) showing the phase boundary and different morphologies of the two new phases (Phase I and II). Abbreviations: Suv: Struvite.

As imaging alone is unsuitable for identifying phases, we confirmed the light microscopic and SEM information by Raman microspectroscopic analyses of the altered mm-sized struvite crystals. The spectra confirmed the presence of peaks corresponding to struvite and newberyite in samples altered at 22 and 37 °C (Frost et al., 2012; Frost et al., 2005). We also collected mixed spectra showing struvite and dittmarite peaks (due to possible underlying of struvite below dittmarite) in samples altered at 37 °C. Note that to the best of our knowledge, a reference pattern for dittmarite is lacking in the literature,

and thus, here we present the first evidence for the Raman spectrum of this phase (Fig 5.5, a). Struvite showed Raman bands at ca. 275 cm^{-1} , 295 cm^{-1} , $413\text{--}448\text{ cm}^{-1}$, 570 cm^{-1} and 945 cm^{-1} . In addition, there were Raman bands from N–H and O–H stretching vibrations at $\sim 2930\text{ cm}^{-1}$ and between ~ 3110 to $\sim 3250\text{ cm}^{-1}$ (Fig. 5.5, a). Meanwhile, the spectrum of newberyite showed Raman bands at ca. 393 , 400 , 500 , 514 , 541 , 890 , 984 , 1054 and 1153 cm^{-1} and from O–H stretching vibrations between ~ 3270 and $\sim 3480\text{ cm}^{-1}$ (Fig. 5.5, a). The bands at ~ 3350 and $\sim 3382\text{ cm}^{-1}$ were assigned to OH groups (Frost et al., 2005). The Raman spectrum of dittmarite was very similar to that of struvite, with differences in the position of the most intense peak (at 945 cm^{-1} in the case of struvite and $\sim 950\text{ cm}^{-1}$ in the spectrum of dittmarite, the latter displaying an asymmetric shape suggesting the presence of two overlapping peaks) and in the O–H stretching region (Fig. 5.5, a). In $60\text{ }^\circ\text{C}$ samples, spectra of altered struvite, as well as the reaction product newberyite, showed considerable peak broadening (Fig. 5.5, b).

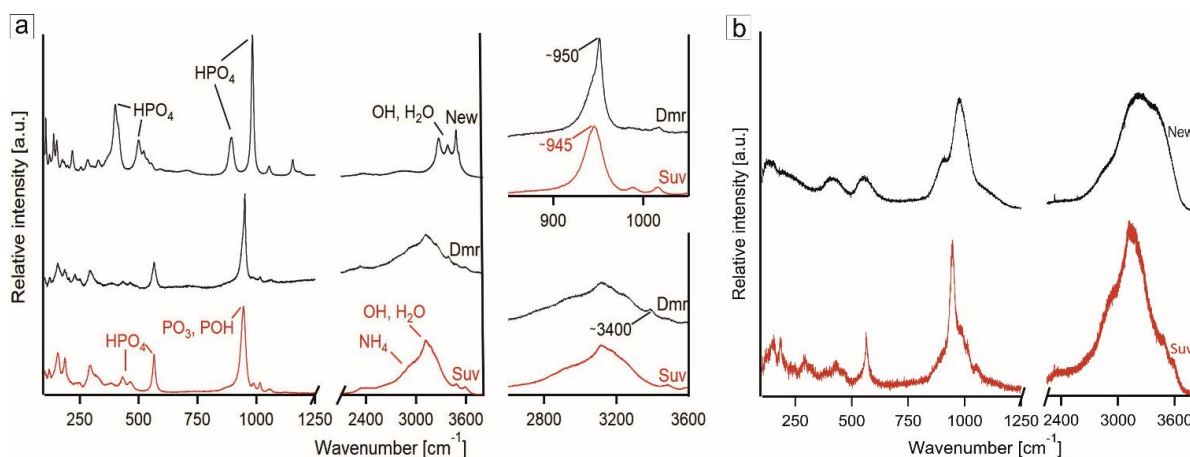


Fig. 5.5 a) Raman spectra of struvite, newberyite and dittmarite collected from single crystals at 22 and $37\text{ }^\circ\text{C}$ after 10 months. The right side shows details of selected wavenumber ranges in the spectra of struvite and dittmarite. b) Raman spectra of single crystals transformed at $60\text{ }^\circ\text{C}$ after 1 day of reaction (struvite) and after 1 week (newberyite). All spectra were collected using 5 accumulations of 5 s each and a $50\times$ objective. Abbreviations: Suv: Struvite; New: Newberyite; Dmr: Dittmarite.

As mentioned above, at $60\text{ }^\circ\text{C}$ and after ~ 12 and 24 weeks, no more diffraction peaks could be observed in the XRD patterns (Fig. 5.2), inferring the breakdown of dittmarite into an amorphous phase. We characterised this material by FTIR spectroscopy, and the patterns (Fig. 5.6) revealed only low intensity and broad PO_4^{3-} asymmetric stretching bands at $\sim 1000\text{ cm}^{-1}$, NH_4^+ bending bands at $\sim 1400\text{ cm}^{-1}$ and H_2O bending bands at $\sim 1600\text{ cm}^{-1}$. A broad, low-intensity band between ~ 2600 and $\sim 3300\text{ cm}^{-1}$ attributed to water stretching bands was also identified. Compared to the sharper bands of the initial struvite (red pattern in Fig. 5.6), the lower intensity in the amorphous product (Fig. 5.6) revealed both the loss of water and ammonia and the breakdown of the crystalline structure, confirming the observations of Hövelmann et al. (2019b) who observed the same breakdown at $90\text{ }^\circ\text{C}$. A full list of all observed Raman and IR bands is shown in Appendix B, Tab. B4, B5.

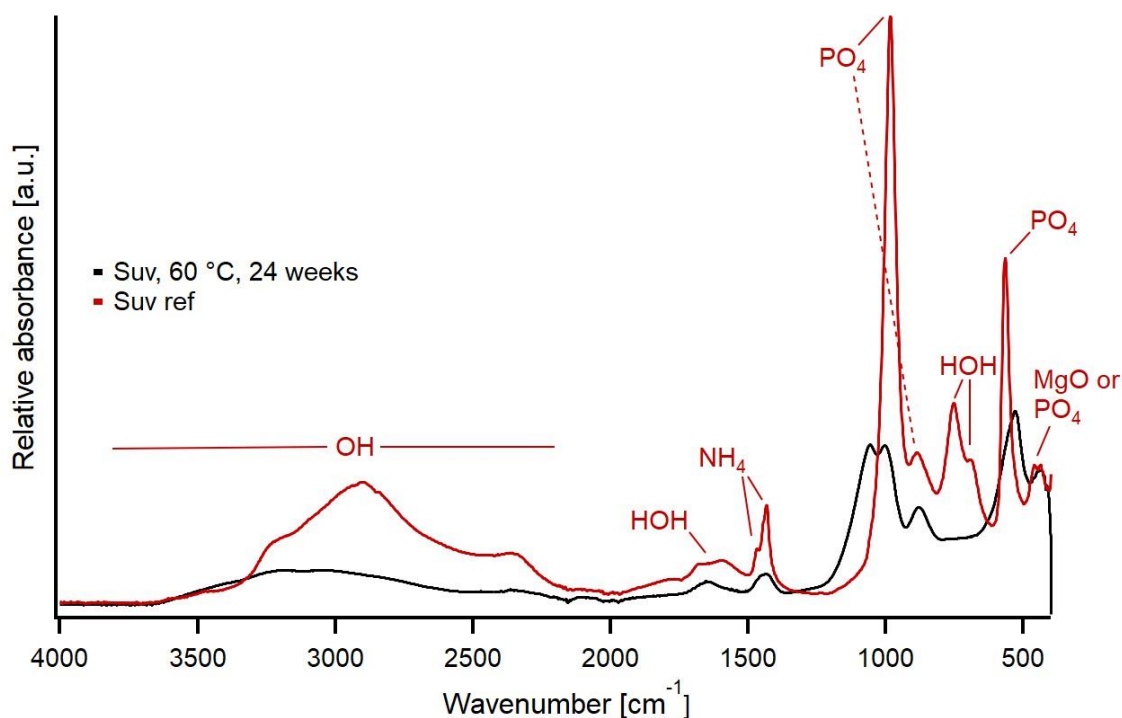


Fig. 5.6 IR spectra of a struvite reference (Stefov et al., 2005) and the resulting amorphous phase (as confirmed by XRD, Fig. 5.2) after reacting at 60 °C for 24 weeks.

5.5 Discussion

5.5.1 Struvite transformation products

Our results documented the conditions under which struvite transforms when reacted in air at ambient conditions and at temperatures up to 60 °C. We assigned phase I (as observed by SEM imaging, Fig. 5.3; Fig. 5.4) to be newberyite based on the results of powder XRD (Fig. 5.1; App. B, Fig. B1; Fig. B2) and Raman spectroscopy (Fig. 5.5, a, b). Although we do not have direct evidence to prove the identity of Phase II (as observed by SEM, Fig. 5.4) in the samples reacted at 60 °C, we interpret this phase to be dittmarite, based on the powder XRD patterns (Fig. 5.1, b; App. B, Fig. B3) and the Raman spectra of samples transformed at 37 °C (Fig. 5.5, a).

It is noteworthy that, although we observed the transformation of struvite to the new phases in the powder samples to be very fast at 60 °C in single crystals, this transformation seemed to proceed slower. This is indicated by the fact that we could not find dittmarite in single crystal samples that reacted for < 10 months at 37 °C and that we did not find dittmarite in samples that reacted for ≤ 1 month at 60 °C by Raman spectroscopy. However, this is not surprising since the grain size is expected to influence the reaction rate due to a lower surface area than powder-sized samples.

With our temperature-dependent information for the transformation reaction, we extracted kinetic parameters for the transformation reactions. Our data showed that upon interaction with air, both the

mm-sized single crystals and μm -sized struvite powder samples transformed partially or fully into secondary phases. The extent of the transformation and the reaction pathways were highly temperature-dependent: While struvite transformed only to a minor extent and exclusively into newberyite at 22 °C, dittmarite was the dominating secondary phase at higher temperatures. Dittmarite formed at the expense of newberyite, which became a minor phase. Both reactions, struvite to newberyite as well as struvite to dittmarite, took place while the host crystal's morphology and outer features were preserved, resulting in pseudomorphs of newberyite and/or dittmarite after struvite. These results mirror observations of natural settings, where several cm-sized struvite crystals formed in guano samples became pseudomorphically replaced by newberyite (Cohen and Ribbe, 1966). Dittmarite is rarely found in nature, but e.g., Snow et al. (2014) proposed that dittmarite found in guano sediments has probably formed from decomposed struvite.

5.5.2 Reaction kinetics and replacement mechanism

Based on the derived Avrami exponent or n -value (Tab. 5.1), we can draw conclusions regarding the reaction mechanism, the type of nucleation and the geometry of the new phases forming in the transformation reactions (Hancock and Sharp, 1972; Hulbert, 1969), as was successfully done for other mineral transformations (e.g., Roza-Llera et al., 2023; Davidson et al., 2008). The derived empirical n -value is also cross-correlated and supported by our morphological observations (Fig 5.3.; Fig. 5.4). The nearly constant reaction order at each temperature indicates a single transformation mechanism.

We documented that the reaction from struvite to newberyite and struvite to dittmarite at 22 and 60 °C progressed with a reaction order of 0.3–0.5 (Tab. 5.1). Taking experimental and analytical errors into account, these values match those of Hulbert (1969) who assigned reactions with an order in the range of $0.53 < n < 0.58$ to a 1-dimensional, diffusion-dominated growth process with either a constant or decreasing nucleation rate. This transformation pathway is supported by our findings of the needle-shaped morphology of the newberyite (Phase I; Fig. 5.3, d, e) and prismatic-shaped dittmarite crystals (Phase II; Fig. 5.4, f). The similar n -values indicate that the transformation of struvite to newberyite and struvite to dittmarite progressed both following the same transformation mechanism.

In this case, a diffusion-dominated process can be interpreted as the reaction kinetics being driven by the release of NH_3 and $3\text{H}_2\text{O}$ removed by diffusion from the crystal, which is the rate-limiting step of the transformation. Kasioptas et al. (2010) similarly obtained a reaction order of 0.77 for the fluid-driven replacement of aragonite by apatite, which they interpreted as a combination of “diffusion factors and [...] a first-order kinetics value”. Given the kinetic parameters obtained for the transformation of struvite to newberyite and struvite to dittmarite in the current study, we propose that, indeed, the transformations occurred by a combination of a temperature-dependent diffusion of water and

ammonia out of the struvite structure as the slowest step of the transformation. Our Raman and FTIR data (Fig. 5.5; Fig. 5.6) confirm this, showing the broadening and/or loss of NH_3 and $3\text{H}_2\text{O}$ with related bands with increasing temperature and longer reaction time.

5.5.3 Coupled dissolution-precipitation transformation reactions

Although diffusion of H_2O and NH_3 determines the rate of struvite transformation in air, it is unlikely that the transformation solely occurs through a solid-state diffusion mechanism. This is due to the total reorganisation of the crystal structures for both transformation reactions (struvite \rightarrow newberyite and struvite \rightarrow dittmarite; see App. B, Fig. B7 for structural models of these phases). Indeed, newberyite and dittmarite formed from struvite exhibit textural characteristics typical of a mineral replacement reaction through a dissolution-precipitation process. These are, among others, the preservation of the external shape of the original parent struvite crystal, the formation of a pseudomorph, and the generation of high amounts of porosity within the replaced phase (Ruiz-Agudo et al., 2014; Putnis, 2009). Several mineral transformation reactions occur through a dissolution-crystallisation mechanism, even in the virtual absence of an aqueous fluid/water in the system. Examples include the carbonation of portlandite ($\text{Ca}(\text{OH})_2$), where the former mineral transforms pseudomorphically into calcite upon exposure to air (Ruiz-Agudo et al., 2013) or the conversion of ikaite to calcite (Sánchez-Pastor et al., 2016). Beruto and Botter (2000) reported that, during the portlandite to calcite conversion, the exposure of the former mineral to air generated a thin layer of water adsorbed on the portlandite crystal surfaces. This nanometric fluid layer provided the means to initiate the dissolution-crystallisation process (Ruiz-Agudo et al., 2013). Indeed, the presence of a free fluid phase in a replacement system can catalyse the transformation (Putnis, 2021), and experimental evidence showed that even small amounts of water (i.e. a few ppm) can suffice and will shift the replacement reaction from a “dry” solid-state type diffusion mechanism to a “wet” dissolution-precipitation type reaction. In the latter, the catalytic effect of water will invariably also alter the rate and mechanism of the transformations (Putnis, 2021; Milke et al., 2013). This current study documented a similar mechanism for transforming struvite into newberyite and/or newberyite and dittmarite. Both these transformation reactions release substantial amounts of water (three mol of H_2O during the formation of newberyite and five mol of H_2O during the formation of dittmarite). This shift of struvite into less hydrated phases as documented through our XRD (Fig 5.1, Fig. 5.2), SEM (Fig. 5.3, Fig. 5.4), Raman (Fig. 5.5), and FTIR (Fig. 5.6) analyses supports this scenario.

In particular, the loss of water and ammonia during the transformation, as documented by both our microscopic observations through the formation of fractures and voids in the original struvite upon its transformation (Fig. 5.3; Fig. 5.4) and the change in Raman and FTIR band intensities (Fig. 5.5; Fig. 5.6)

revealed that the replacement reaction likely started simultaneously at several points of the surface of the parent struvite. Once the transformation is initiated at different points and water is released, the destabilisation of the struvite structure progresses and is temperature-dependent. This fluid film promotes the formation of the secondary phases, which leads to the progressive breakdown of struvite and the growth of newberyite and dittmarite. The boundary between the unaltered struvite and the secondary phases, which marks the reaction front, is very sharp in all cases. The transformation progress follows through the continuous transfer of ammonia and water out of the primary struvite to the reaction front and into the new phases. This water and/or ammonia removal/transport is concomitant with the generation of porosity during the transformation, as documented in our SEM images (Fig. 5.3; Fig. 5.4). This porosity is formed as a result of the decrease in molar volume between the primary and secondary phases. Indeed, for the replacement to be pseudomorphic, the deficit in molar volume between the dissolving struvite ($V_{\text{Suv}} = 144.36 \text{ mol}\cdot\text{cm}^{-3}$) and the precipitating secondary phases ($V_{\text{Dta}} = 73.96 \text{ mol}\cdot\text{cm}^{-3}/V_{\text{New}} = 83.01 \text{ mol}\cdot\text{cm}^{-3}$) (calculated from mineral densities (Anthony et al., 2001-2005) and molar masses) needs to be compensated by the generation of equal amounts of porosity. As a result, the transformed areas surrounding or within the unreacted struvite must equate to a volume of porosity equal to the volume loss derived from the molar volume change associated with the replacement reaction ($\Delta V = -70.4 \text{ mol}\cdot\text{cm}^{-3}$ and $-61.35 \text{ mol}\cdot\text{cm}^{-3}$ for the transformation into dittmarite and newberyite, respectively): i.e., $\geq 51.2 \%$ when struvite transforms into dittmarite and $\geq 42.5 \%$ porosity when it transforms into newberyite. We have no empirical measurements for the ΔV change, but our SEM images (Fig. 5.3; Fig. 5.4) document the shrinkage (negative ΔV) of the transformation reactions.

The decrease in molar volume between the primary and secondary phases is so pronounced that it is impossible to accommodate all the porosity within the replaced layer. This explains the development of a gap between the two phases, which is often observed in the SEM images (Fig. 5.3) between the new phases and the unaltered struvite surfaces. Similar gaps have been reported in other mineral replacement systems with large molar volume changes between the primary and secondary phases. For example, the replacement of gypsum by celestine (Forjanés et al., 2020) or the replacement of rutile by pyrochlore (Pöml et al., 2007) also proceeded by such large ΔV changes. The formation of gaps with reaction progress and the development of porous secondary layers explains the brittleness of the pseudomorphs and why they appear extensively fractured (see Fig. 5.3; Fig. 5.4). Fracture formation during transformation reactions is a common feature in fluid-driven mineral transformations with very pronounced molar volume changes between the primary and secondary phases. For example, such processes have been documented during the transformation of leucite to analcime (Putnis et al., 2007).

5.5.4 Reaction pathways

This study's novelty is that we have, for the first time, quantified the temperature-dependent decomposition of struvite. We have documented that, at 22 °C, even after 10 months, less than 20 wt% of the initial struvite transforms to newberyite, while at higher temperatures, dittmarite is the dominant and full transformation product. Previous studies have shown that slow heating of struvite in air leads to a replacement by newberyite. During this reaction, the ammonia leaves the structure before the mineral loses water molecules (Frost et al., 2004). This observation is consistent with our results at 22 °C. However, at higher temperatures, its faster transformation to dittmarite requires a quicker and more substantial release of water (five H₂O molecules in contrast to three H₂O molecules necessary to form newberyite), yet the retention of ammonia in the dittmarite structure. Similar preferential and temperature-dependent reaction pathways have also been reported, for example, during the transformation of ikaite crystals (CaCO₃·6H₂O) at 10 °C into calcite, where six H₂O molecules are also lost through pseudomorphic transformations. Conversely, at 20 °C, ikaite transformed first to vaterite, a metastable phase, due to accelerated water loss from the ikaite before its transformation to calcite (Sánchez-Pastor et al., 2016). These observations evidence the vital role that the reaction temperature and the heating rate (invariably, ikaite) have in reaction pathways during the decomposition of intensely hydrated minerals such as struvite or ikaite. Furthermore, we did not evaluate the potential role of humidity in the sample environment during our transformation reactions. However, our open-system experimental vials cannot disregard an increase or change. This would match the suggestion that humidity can be an essential factor in transforming struvite to dittmarite (Farhana, 2016) and indicates that humidity influences the stability of struvite in general. Farhana (2016) further proposed that the presence of ammonia also influences the stability of struvite, yet no empirical data exists to support this effect.

5.6 Conclusions and implications

We document the transformation of struvite under variable temperature conditions into newberyite and/or dittmarite before all crystalline phases break down into an anhydrous amorphous phase. At 22 °C, struvite transforms exclusively into newberyite even after 10 months of reaction. At higher temperatures, struvite transforms to both newberyite and dittmarite, with dittmarite being favoured with increasing temperature. The transformations occur through dissolution-precipitation and are driven by the diffusive release of ammonia and water during the decomposition of struvite.

Struvite is considered a sustainable recoverable resource for P and N from wastewater and ideal for use as a slow-release fertiliser, and thus has implications from the point of view of a circular economy (Chandrasekaran et al., 2024; Azam et al., 2019; Kataki et al., 2016b). Our data shows, however, that to

use struvite as a fertiliser, the dry struvite manufactured in the form of pellets (Forrest et al., 2008) must be stored at low temperatures to avoid its transformation into less valuable materials (loss of N). Our empirical data suggests that to retain N in the crystal structure of struvite, fertiliser must be stored ideally in closed containers at low temperatures. If storage temperatures increase to ≥ 22 °C, this will lead to the transformation of struvite to newberyite and/or dittmarite, resulting in the loss of N from the mineral, or at higher temperatures, the formation of a phase susceptible to undergo a rapid amorphisation process. Our relatively long-term study (up to 10 months) revealed that to optimise the use of struvite as a fertiliser, one has to keep the fertilisers at low temperature and reduce the maximum time that such struvite fertilisers are stored before use to avoid its transformation into secondary phases and thus lose part of their fertiliser capacity.

Acknowledgements

The authors thank Marcin Syczewski for assistance with scanning electron microscopic imaging and Nicolai Klitscher for preparing thin sections, both from the German Research Centre for Geosciences GFZ Potsdam. We further thank Max Wilke and Christoph Moeller for their allowance to use the Raman spectroscope of the University of Potsdam while the Raman spectroscope of the GFZ Potsdam was under repair. Furthermore, we thank Dr. Jeffrey Perez from the GFZ Potsdam for the fruitful scientific discussions.

6 Discussion and concluding remarks

In this thesis, the particular projects investigated different aspects of geochemistry and mineralogy of the mineral struvite. These aspects comprised the molecular structure of the crystalline struvite, the kinetics of struvite formation, and its transformation. The experiments and analyses were conducted under a selected temperature range under environmental conditions. This ensures the applicability of the results to P recovery and the use of struvite as a fertiliser. The presented work contributes to a better understanding of the formation of struvite under different temperatures. It adds new insights into the conditions of struvite stability and the pathways and products of its decomposition under ambient conditions.

6.1 Summary of the most important findings

6.1.1 Struvite nucleation and growth in aqueous solution

The formation of struvite has been widely analysed experimentally with a focus on the precipitation from wastewater (e.g., Agrawal et al., 2018; Ariyanto et al., 2014; Nelson et al., 2003), besides the precipitation from urine (e.g., Li et al., 2019; Ronteltap, 2009; Tilley et al., 2008). The primary study subjects were process parameters influencing the formation of struvite, such as pH and Mg:N:P ratios, the P recovery potential of struvite, and economic feasibility. The synthesis from the pure salt solutions has been investigated regarding Mg:N:P ratios and the source of Mg, as well as some kinetics (e.g., Shaddel et al., 2020; Hövelmann et al., 2019a; Rahaman et al., 2008). The kinetic studies on struvite nucleation and growth only insufficiently consider different concentrations, pH and temperature conditions of the growth solution. Several mechanisms were proposed for the nucleation of struvite at room temperature amongst the determination of kinetic parameters. One sub-project of this work addressed the experimental temperature as an essential factor influencing the formation of struvite, besides the concentration of salts in solution (Ch. 3). Synthesis experiments in pure salt solutions were conducted at different temperatures (5–50 °C) and the kinetics were monitored by 1. off-site *in-situ* pH and turbidity measurements, and 2. *in-situ* synchrotron-based WAXS methods. The results of the off-site experiments demonstrate a decrease in nucleation induction time from 5–25 °C and an increase in induction time from 25–37 °C. This emphasises that the temperature-dependency of struvite solubility reverses at 25–50 °C. Struvite's solubility in dependence on temperature is still discussed (Crutchik and Garrido, 2016), with some authors suggesting a reverse temperature-dependence (Hanhoun et al., 2011; Bhuiyan et al., 2007).

Furthermore, data from *in-situ* WAXS analyses was evaluated with the Avrami model to gain the nucleation mechanism and rate constants k for different temperatures. The obtained parameters were

used to calculate the activation energy of struvite formation. Secondly, one dataset of the off-site pH and turbidity measurements was evaluated by using a Monte Carlo simulation approach. This calculation provided a kinetic rate constant for the dataset. While this work is submitted as a chapter of the thesis, additional data will be added by further kinetic modelling using the Monte Carlo simulation on all pH and turbidity datasets. Then, this chapter will be prepared as a manuscript to be submitted to a scientific journal. *This study already has further implications for the solubility properties of struvite with temperature. Furthermore, future publications will provide a unique comparison of two different approaches to evaluate kinetic data using two different methods.*

6.1.2 The crystal structure of struvite

A crystalline material's structure is crucial to understanding its chemico-physical properties and interactions with the environment. All crystallographic information of a crystalline structure is stored and made available to scientific researchers in the form of CIF-files (Hall and Westbrook, 2006). The crystal structure of struvite has been solved by single-crystal XRD and neutron diffraction by several researchers (Ferraris et al., 1986; Abbona et al., 1984; Whitaker and Jeffery, 1970a). However, information on the hydrogen bonding network of struvite was incomplete. The stability and vibrational behaviour of chemical bonds, especially of hydrogen bonds, are temperature-dependent (Jeffrey, 1997). In this thesis, the crystal structure of struvite was analysed by single crystal-XRD at 100 K and solved using SHELXL (Ch. 4). This improves the former studies, which were all conducted at room temperature. *The structure solution at low temperatures revealed that the structure of struvite is well comparable to other reported structures but provides a higher resolution of structure parameters and a more reliable image of the hydrogen bonding network. It is shown that the NH_4^+ ion is bonded by three hydrogen bonds to the other ionic complexes in the struvite structure at 100 K in contrast to only one bond at 298 K.*

6.1.3 Stability of struvite under different conditions

Struvite has a low solubility (Bhuiyan et al., 2007). Therefore, it is considered relatively stable in aqueous solution. As mentioned before, clear information on its solubility with changing temperatures is still missing. The results of Chapter 5 provide more implications on the stability of struvite depending on the solution temperature.

In air, struvite is known to be unstable at ambient conditions: It was reported to decompose into different Mg phosphate products by losing NH_3 and H_2O (Tansel et al., 2018). In this thesis, implications on the causes of struvite's instability in air are given by the results of Chapter 4. The new information on the hydrogen bonding network reveals that, at temperatures of 100 K, the ammonium ion in the struvite structure has at least two hydrogen bonds. This indicates that the ion is behaving statically and is more stable. In contrast, it was reported to rotate at 298 K (Whitaker and Jeffery, 1970b), implicating that removing NH_3 from the struvite structure at room temperature is easier. *The structural analysis of*

struvite at low temperatures that was conducted in this thesis helps better to understand the instability of this mineral at ambient conditions.

6.1.4 Struvite decomposition and transformation

The decomposition products of the reaction of struvite in the air were reported to be very diverse. Whitaker (1968) proposed that struvite be transformed into newberyite at room temperature, but this hypothesis was not proved. In contrast, the transformation into newberyite was only observed in aqueous solution (Babić-Ivancić et al., 2006; Boistelle et al., 1983). Struvite was further reported to react to dittmarite in the presence of water (Bayuseno and Schmahl, 2020; Bayuseno and Schmahl, 2018; Ramlogan and Rouff, 2016), and, in air, into amorphous magnesium hydrogen phosphate (Bayuseno and Schmahl, 2019; Hövelmann et al., 2019b), as well as magnesium phosphates without structural water (Novotny, 2011; Sarkar, 1991). The study presented in Chapter 5 of this thesis quantifies the decomposition of struvite in air for the first time. The reaction was monitored with time at different temperatures by *ex-situ* XRD. This provided the kinetic evaluation of the process and the product characterisation. It was found that struvite transforms into two different products, newberyite and dittmarite, with newberyite as the only product at 25 °C and dittmarite as the preferred product at higher temperatures. Kinetic modelling using the Avrami equation showed that the rate-limiting step of this reaction is the diffusion of NH₃ and H₂O out of the struvite structure. Optical and electron microscopy further revealed that both transformation reactions follow a coupled dissolution-precipitation mechanism. *This work reports the reactions of struvite into both newberyite and dittmarite for the first time and defines specific temperature conditions for their formation. It further reveals the kinetics and mechanisms of the transformation processes by a combined methodological approach.*

6.2 Conclusions and impact

The original scope of this doctoral thesis was to understand better the formation of struvite from pure salt solutions, without any additives, on a small scale. Fundamental research on the formation of this mineral contributes to the design of struvite precipitation and recovery facilities for the recovery of P and N as crucial resources for fertilisers. It aimed to characterise better the kinetics of nucleation and growth and formation conditions when struvite forms in aqueous solutions to understand better its formation conditions rather than when it is monitored in wastewater and urine. During the work of this thesis, it was shown that the formation kinetics are highly dependent on the solute concentration in solution and the solution temperature. At the same time, a change in these conditions did not lead to a shift in the nucleation mechanism. However, the time of formation (the induction time) changed at

temperatures $> 25\text{ }^{\circ}\text{C}$. This has an important implication for struvite recovery in different aqueous environments, as the precipitation kinetics would change with the environmental temperature.

Experiments and characterisation of struvite precipitates in the scope of the nucleation and growth project revealed problems in storing struvite samples in the laboratory. After storage in a petri dish for several months, the struvite crystals developed white, opaque spots on their surface, as observed under the optical microscope (Fig. 6.1). It was found to transform into another phase by XRD analysis. This led to further literature research about the state of the art of struvite stability. It was found that there has been a lack of information on the stability of struvite, especially when kept under atmospheric conditions. This coincidence led to this work's second research goal: to better understand the stability of struvite in air. Knowing the stability conditions and the decomposition products is crucial for producing, storing and applying struvite fertiliser pellets. It is important to know under which temperature conditions struvite can be stored safely without transforming. Following, knowing the phase properties of the decomposition products helps judge if the altered struvite can still be applied as a fertiliser to a crop field.

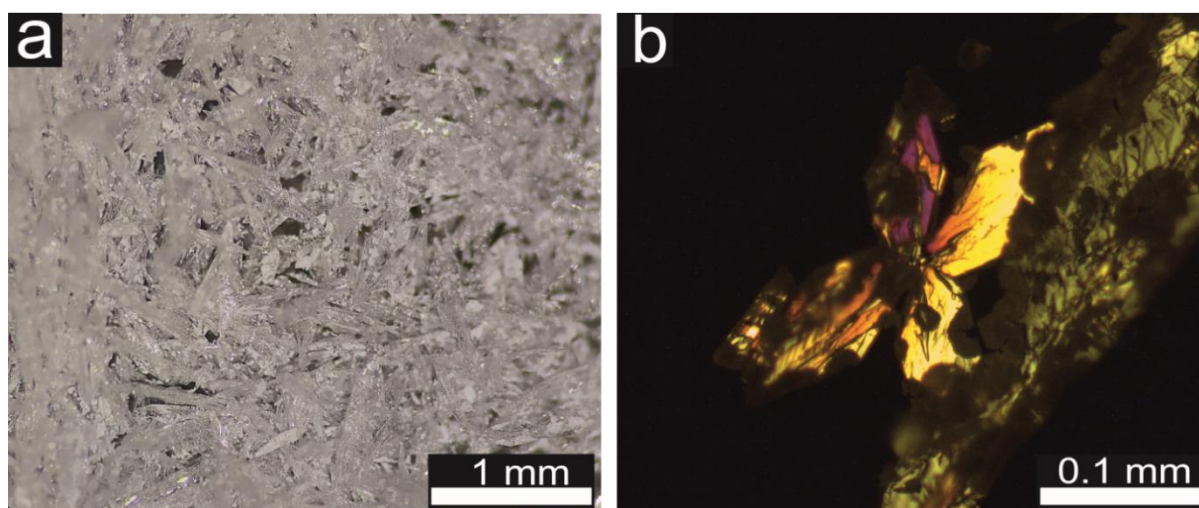


Fig. 6.1 a) Light microscope image of a seven months old struvite sample with white, opaque spots. b) Image of the same sample under transmitted, crossed-polarized light.

Solving the crystal structure of this mineral at low temperatures revealed highly resolved data on structural properties and the hydrogen bonding network. It was shown that, at 100 K, the NH_4^+ ion in the structure was bound by at least two hydrogen bonds. This leads to a static behaviour of the ion and an improved stability of the structure. Therefore, the structural investigations lead to a better understanding of the influence of environmental temperature on the stability of struvite as a whole.

Furthermore, this work investigated the reaction of struvite in air at room temperature and elevated room temperatures for the first time. It was shown that struvite transforms to newberyite only when

kept in air at 22 °C, while there are two transformation products, struvite and dittmarite, at higher temperatures. The loss of NH_4^+ and H_2O is crucial for these processes, which is expressed as a diffusion-dominated kinetic mechanism. It was further found that the phase transformations to both newberyite and dittmarite occur by a coupled dissolution-precipitation reaction. These reactions induce a change in phase volumina and create porosity. Therefore, this study implies that there are important changes in the physico-chemical properties of struvite, influencing its characteristics as a fertiliser. Based on the results of this thesis, it is advised to store struvite products in closed containers at temperatures ≤ 0 °C to maintain their properties.

6.3 Future outlook

Although some important research questions of this study could be examined, new questions and opportunities arose during this work and after the evolution of the results.

Modelling the kinetics of struvite nucleation and growth has been done by various researchers for the formation of struvite in wastewater (e.g., Ariyanto et al., 2014; Capdevielle et al., 2014; Quintana et al., 2005). However, detailed information on the formation from pure salt solutions is still lacking. Therefore, this thesis's analysis of struvite formation kinetics adds valuable data. Modelling using the Avrami equation for the struvite system is entirely new. Furthermore, the comparison with a different model, as done here, presents a unique approach. Therefore, future work includes modelling with all datasets collected during this project and submitting Chapter 3 as a publication to a scientific journal.

The work done in Chapter 3 evaluates kinetic mechanisms purely by modelling the parameters n and k . However, the evaluation of the mechanism profits from accomplishing techniques such as imaging. Therefore, for future work, struvite samples could be recovered at different time points of the synthesis. These samples should be imaged using electron microscopy techniques, such as SEM and TEM, for additional insights into the mechanism. As an amorphous precursor phase prior to struvite has been proposed by some publications (Karafiludis et al., 2023b; Hövelmann et al., 2019a), the existence of this phase could be verified.

Many parameters influencing the stability of struvite in air and in solution have not been investigated sufficiently. Notably, the long-term stability of struvite in air at temperatures ≤ 25 °C should be examined thoroughly regarding the storage of struvite fertiliser. Furthermore, this work, as well as references in the literature, imply that air humidity influences stability (Farhana, 2016; Frost et al., 2004), which should be further investigated in combination with temperature conditions.

During the analyses of transformed struvite (-newberyite,-dittmarite) samples, imaging the phase boundaries of the transformed phases proved to be difficult due to insufficient resolution. It would be

Discussion and concluding remarks

useful to apply analytical techniques, such as TEM, that allow nm-scale resolution to examine the areas around the exact phase boundaries and gain further insight into the transformation mechanism. As struvite is highly sensitive to vacuum, special measures in sample preparation and cryogenic conditions are required when using the TEM.

Especially for applying struvite as a fertiliser, there is still potential future work that is crucial for a successful application of struvite for agricultural purposes, contributing to a more sustainable industrial P cycle.

References

- Aage, H. K., Andersen, B. L., Blom, A., and Jensen, I. (1984) The solubility of struvite. *Journal of Radioanalytical and Nuclear Chemistry*, 223, 213–215, DOI: <https://doi.org/10.1007/BF02223387>.
- Abbona, F., Calleri, M., and Ivaldi, G. (1984) Synthetic struvite, $\text{MgNH}_4\text{PO}_4 \cdot 6\text{H}_2\text{O}$: correct polarity and surface features of some complementary forms. *Acta Crystallographica B Structural Science*, 40, 223–227, DOI: <https://doi.org/10.1107/S0108768184002020>.
- Abbona, F., Lundager Madsen, H. E., and Boistelle, R. (1982) Crystallization of two magnesium phosphates, struvite and newberyite: Effect of pH and concentration. *Journal of Crystal Growth*, 57, 6–14, DOI: [https://doi.org/10.1016/0022-0248\(82\)90242-1](https://doi.org/10.1016/0022-0248(82)90242-1).
- Abbona, F., Boistelle, R., and Haser, R. (1979) Hydrogen bonding in $\text{MgHPO}_4 \cdot 3\text{H}_2\text{O}$ (newberyite). *Acta Crystallographica B Structural Science*, 35, 2514–2518, DOI: <https://doi.org/10.1107/S0567740879009791>.
- Abdelrazig, B. and Sharp, J. H. (1988) Phase changes on heating ammonium magnesium phosphate hydrates. *Thermochimica Acta*, 129, 197–215, [https://doi.org/10.1016/0040-6031\(88\)87336-2](https://doi.org/10.1016/0040-6031(88)87336-2).
- Acelas, N. Y., Flórez, E., and López, D. (2015) Phosphorus recovery through struvite precipitation from wastewater: effect of the competitive ions. *Desalination and Water Treatment*, 54, 2468–2479, DOI: <https://doi.org/10.1080/19443994.2014.902337>.
- Agrawal, S., Guest, J. S., and Cusick, R. D. (2018) Elucidating the impacts of initial supersaturation and seed crystal loading on struvite precipitation kinetics, fines production, and crystal growth. *Water research*, 132, 252–259, DOI: <https://doi.org/10.1016/j.watres.2018.01.002>.
- Andreassen, J.-P. and Lewis, A. E. (2017) Classical and Nonclassical Theories of Crystal Growth, in: *New Perspectives on Mineral Nucleation and Growth: From Solution Precursors to Solid Materials*. Edited by: van Driessche, A. E., Kellermeier, M., Benning, L. G., and Gebauer, D., Springer International Publishing; Imprint: Springer, Cham, 137–154, DOI: https://doi.org/10.1007/978-3-319-45669-0_7.
- Anthony, J. W., Bideaux, R. A., Bladh, K. W., and Nichols, M. C. (2001-2005): *Handbook of Mineralogy. Mineralogical Society of America*, Chantilly, VA 20151-1110, USA, <http://www.handbookofmineralogy.org/>.
- Ariyanto, E., Ang, H. M., and Sen, T. K. (2014) Impact of various physico-chemical parameters on spontaneous nucleation of struvite ($\text{MgNH}_4\text{PO}_4 \cdot 6\text{H}_2\text{O}$) formation in a wastewater treatment plant: kinetic and nucleation mechanism. *Desalination and Water Treatment*, 52, 6620–6631, <https://doi.org/10.1080/19443994.2013.821042>.
- Arrhenius, S. (1889a) Über die Reaktionsgeschwindigkeit bei der Inversion von Rohrzucker durch Säuren, *Zeitschrift für Physikalische Chemie*, vol. 4U, no. 1, 226–248, DOI:10.1515/zpch-1889-0416.
- Arrhenius, S. (1889b) Über die Dissociationswärme und den Einfluss der Temperatur auf den Dissociationsgrad der Elektrolyte, *Zeitschrift für Physikalische Chemie*, 4U, 96–116, DOI: <https://doi.org/10.1515/zpch-1889-0408>.
- Avrami, M. (1940) Kinetics of Phase Change. II Transformation-Time Relations for Random Distribution of Nuclei, *The Journal of Chemical Physics*, 8, 212–224, DOI: <https://doi.org/10.1063/1.1750631>.

References

- Avrami, M. (1939) Kinetics of Phase Change. I General Theory. *The Journal of Chemical Physics*, 7, 1103–1112, DOI: <https://doi.org/10.1063/1.1750380>.
- Azam, H. M., Alam, S. T., Hasan, M., Yameogo, D. D. S., Kannan, A. D., Rahman, A., and Kwon, M. J. (2019) Phosphorous in the environment: characteristics with distribution and effects, removal mechanisms, treatment technologies, and factors affecting recovery as minerals in natural and engineered systems. *Environ Science and Pollution Research*, 26, 20183–20207, DOI: <https://doi.org/10.1007/s11356-019-04732-y>.
- B.H. Toby and R.B. Von Dreele (2013): General Structure Analysis System-II (GSAS-II). *Journal of Applied Crystallography*, 544–549, <https://doi.org/10.1107/S0021889813003531>.
- Babić-Ivancić, V., Kontrec, J., and Brecević, L. (2004) Formation and transformation of struvite and newberyite in aqueous solutions under conditions similar to physiological. *Urological research*, 32, 350–356, DOI: <https://doi.org/10.1007/s00240-004-0427-5>.
- Babić-Ivancić, V., Kontrec, J., Brecević, L., and Kralj, D. (2006) Kinetics of struvite to newberyite transformation in the precipitation system $MgCl_2-NH_4H_2PO_4NaOH-H_2O$. *Water research*, 40, 3447–3455, DOI: <https://doi.org/10.1016/j.watres.2006.07.026>.
- Babić-Ivančić, V., Kontrec, J., Kralj, D., and Brečević, L. (2002) Precipitation Diagrams of Struvite and Dissolution Kinetics of Different Struvite Morphologies. *Croatica Chemica Acta*, 75, 89–106, ISSN-0011-1643.
- Ballirano, P. and Melis, E. (2009) Thermal behaviour and kinetics of dehydration of gypsum in air from in situ real-time laboratory parallel-beam X-ray powder diffraction. *Physics and Chemistry of Minerals*, 36, 391–402, DOI: <https://doi.org/10.1007/s00269-008-0285-8>.
- Bamford, C. H. and Tipper, C. F. H. Eds. (1980) Reactions in the Solid State. In: *Comprehensive chemical kinetics* 22. Elsevier, Amsterdam, 340 pp., ISBN: 0-444-41807-5.
- Basham, M., Filik, J., Wharmby, M. T., Chang, P. C. Y., El Kassaby, B., Gerring, M., Aishima, J., Levik, K., Pulford, B. C. A., Sikharulidze, I., Sneddon, D., Webber, M., Dhesi, S. S., Maccherozzi, F., Svensson, O., Brockhauser, S., Náray, G., and Ashton, A. W. (2015) Data Analysis Workbench (DAWN), *Journal of Synchrotron Radiation*, 22, 853–858, <https://doi.org/10.1107/S1600577515002283>.
- Bayuseno, A. P. and Schmahl, W. W. (2020) Crystallization of struvite in a hydrothermal solution with and without calcium and carbonate ions. *Chemosphere*, 250, 126245, DOI: <https://doi.org/10.1016/j.chemosphere.2020.126245>.
- Bayuseno, A. P. and Schmahl, W. W. (2019) Thermal decomposition of struvite in water: qualitative and quantitative mineralogy analysis. *Environmental technology*, 41, 3591–3597, DOI: <https://doi.org/10.1080/09593330.2019.1615558>.
- Bayuseno, A. P. and Schmahl, W. W. (2018) Hydrothermal synthesis of struvite and its phase transition: Impacts of pH, heating and subsequent cooling methods. *Journal of Crystal Growth*, 498, 336–345, DOI: <https://doi.org/10.1016/j.jcrysgro.2018.06.026>.
- Ben Moussa, S., Tlili, M. M., Batis, N., and Amor, M. B. (2011) Influence of temperature on Struvite precipitation by CO₂-deagassing method. *Crystal Research and Technology*, 46, 255–260, DOI: <https://doi.org/10.1002/crat.201000571>.

References

- Benning, L. G. and Waychunas, G. A. (2008) Nucleation, Growth, and Aggregation of Mineral Phases: Mechanisms and Kinetic Controls, in: *Kinetics of water-rock interaction*, edited by: Brantley, S. L., Kubicki, J. D., and White, A. F., Springer Verlag, New York, 259–333, DOI: https://doi.org/10.1007/978-0-387-73563-4_7.
- Beruto, D. T. and Botter, R. (2000) Liquid-like H₂O adsorption layers to catalyze the Ca(OH)₂/CO₂ solid–gas reaction and to form a non-protective solid product layer at 20°C, *Journal of the European Ceramic Society*, 20, 497–503, DOI: [https://doi.org/10.1016/S0955-2219\(99\)00185-5](https://doi.org/10.1016/S0955-2219(99)00185-5).
- Bhuiyan, M. I. H., Mavinic, D. S., and Beckie, R. D. (2007) A solubility and thermodynamic study of struvite. *Environmental technology*, 28, 1015–1026, DOI: <https://doi.org/10.1080/09593332808618857>.
- Bhuiyan, M. I. H., Mavinic, D. S., and Koch, F. A. (2008) Thermal decomposition of struvite and its phase transition. *Chemosphere*, 70, 1347–1356, DOI: <https://doi.org/10.1016/j.chemosphere.2007.09.056>.
- Bichler, K.-H., Eipper, E., Naber, K., Braun, V., Zimmermann, R., and Lahme, S. (2002) Urinary infection stones. *International Journal of Antimicrobial Agents*, 19, 488–498, DOI: [https://doi.org/10.1016/S0924-8579\(02\)00088-2](https://doi.org/10.1016/S0924-8579(02)00088-2).
- Boistelle, R., Abbona, F., and Lundager Madsen, H. E. (1983) On the transformation of struvite into newberyite in aqueous systems, *Physics and Chemistry of Minerals*, 9, 216–222, DOI: <https://doi.org/10.1007/BF00311958>.
- Bots, P., Benning, L. G., Rodriguez-Blanco, J.-D., Roncal-Herrero, T., and Shaw, S. (2012) Mechanistic Insights into the Crystallization of Amorphous Calcium Carbonate (ACC), *Crystal Growth & Design*, 12, 3806–3814, DOI: <https://doi.org/10.1021/cg300676b>.
- Bouropoulos, N. C. and Koutsoukos, P. G. (2000): Spontaneous precipitation of struvite from aqueous solutions. *Journal of Crystal Growth*, 213, 381–388, DOI: [https://doi.org/10.1016/S0022-0248\(00\)00351-1](https://doi.org/10.1016/S0022-0248(00)00351-1).
- Burcar, B., Castañeda, A., Lago, J., Daniel, M., Pasek, M. A., Hud, N. V., Orlando, T. M., and Menor-Salván, C. (2019) A Stark Contrast to Modern Earth: Phosphate Mineral Transformation and Nucleoside Phosphorylation in an Iron- and Cyanide-Rich Early Earth Scenario. *Angewandte Chemie International Edition*, 58, 16981–16987, DOI: <https://doi.org/10.1002/anie.201908272>.
- Burns, J. R. and Finlayson, B. (1982) Solubility Product of Magnesium Ammonium Phosphate Hexahydrate at Various Temperatures. *The Journal of urology*, 128, 426–428, DOI: [https://doi.org/10.1016/S0022-5347\(17\)52952-3](https://doi.org/10.1016/S0022-5347(17)52952-3).
- Cao, X., Lu, H., Liu, J., Lu, W., Guo, L., Ma, M., Zhang, B., and Guo, Y. (2019) 3D plotting in the preparation of newberyite, struvite, and brushite porous scaffolds: using magnesium oxide as a starting material. *Journal of materials science. Materials in medicine*, 30, 88, DOI: <https://doi.org/10.1007/s10856-019-6290-2>.
- Capdevielle, A., Sýkorová, E., Béline, F., and Daumer, M.-L. (2016) Effects of organic matter on crystallization of struvite in biologically treated swine wastewater, *Environmental technology*, 37, 880–892, DOI: <https://doi.org/10.1080/09593330.2015.1088580>.

References

- Capdevielle, A., Sýkorová, E., Béline, F., and Daumer, M.-L. (2014) Kinetics of struvite precipitation in synthetic biologically treated swine wastewaters, *Environmental technology*, 35, 1250–1262, DOI: <https://doi.org/10.1080/09593330.2013.865790>.
- Celen, I. and Türker, M. (2001) Recovery of ammonia as struvite from anaerobic digester effluents. *Environmental technology*, 22, 1263–1272, DOI: <https://doi.org/10.1080/09593332208618192>.
- Chand, P. and Agarwal, O. P. (1991) Electron paramagnetic resonance study of doped synthetic crystals of struvite and its zinc analogue. *Spectrochimica Acta Part A: Molecular Spectroscopy*, 47, 775–783, DOI: [https://doi.org/10.1016/0584-8539\(91\)80149-D](https://doi.org/10.1016/0584-8539(91)80149-D).
- Chandrasekaran, S., Zaffar, A., and Balasubramanian, P. (2024) Struvite in circular economy: Production techniques, emerging applications and market opportunities. *WIREs Energy & Environment*, 13, DOI: <https://doi.org/10.1002/wene.529>.
- Chauhan, C. K., Joseph, K. C., Parekh, B. B., and Joshi, M. J. (2008) Growth and characterization of struvite crystals. *Crystal Research and Technology*, 46, 187–194, DOI: <https://doi.org/10.1002/crat.201000587>.
- Chen, Y., Tang, J., Li, W., Zhong, Z., and Yin, J. (2015) Thermal decomposition of magnesium ammonium phosphate and adsorption properties of its pyrolysis products toward ammonia nitrogen. *Transactions of Nonferrous Metals Society of China*, 25, 497–503, DOI: [https://doi.org/10.1016/S1003-6326\(15\)63630-5](https://doi.org/10.1016/S1003-6326(15)63630-5).
- Christoffersen, J., Christoffersen, M. R., Kibalczyk, W., and Andersen, F. A. (1989) A contribution to the understanding of the formation of calcium phosphates. *Journal of Crystal Growth*, 94, 767–777, DOI: [https://doi.org/10.1016/0022-0248\(89\)90102-4](https://doi.org/10.1016/0022-0248(89)90102-4).
- Cifuentes Delatte, L., Hidalgo, A., Bellanato, J., and Santos, M. (1973) Polarization Microscopy and Infrared Spectroscopy of Thin Sections of Calculi, in: *Urinary calculi: Recent advances in aetiology, stone structure and treatment*, edited by: Cifuentes Delatte, L., Hodgkinson, A., and Rapado, A., Karger, Basel, London, 220–230, DOI: <https://doi.org/10.1159/000394944>.
- Cohen, L. H. and Ribbe, P. H. (1966) Magnesium phosphate mineral replacement at Mono Lake, California. *American Mineralogist*, 51, 1755–1765.
- Compton, K. F. (2009) Newberyite from Skipton Caves (Figure). Last access: 26 March 2024, from <https://www.mindat.org/photo-207833.html>.
- Cordell, D., Drangert, J.-O., and White, S. (2009) The story of phosphorus: Global food security and food or thought. *Global Environmental Change*, 19, 292–305, DOI: <https://doi.org/10.1016/j.gloenvcha.2008.10.009>.
- Crutchik, D. and Garrido, J. M. (2016) Kinetics of the reversible reaction of struvite crystallisation. *Chemosphere*, 154, 567–572, DOI: <https://doi.org/10.1016/j.chemosphere.2016.03.134>.
- Da Filho, J. L. P., Tonetti, A. L., Guimarães, M. T., and Silva, D. (2017) Nutrient recovery from airplane wastewater: composition, treatment and ecotoxicological assay. *Water science and technology a journal of the International Association on Water Pollution Research*, 75, 1952–1960, DOI: <https://doi.org/10.2166/wst.2017.081>.

References

- Dalecha, T., Assefa, E., Krasteva, K., and Meinhold, K. (2014) Struvite production from source separated urine: Application and economic feasibility in Arba Minch, Ethiopia. *Sustainable Sanitation Practice*, 19, 16–22, ISSN: 2308-5797.
- Das, P., Gupta, G., Velu, V., Awasthi, R., Dua, K., and Malipeddi, H. (2017) Formation of struvite urinary stones and approaches towards the inhibition-A review. *Biomedicine & pharmacotherapy*, 361–370, DOI: <https://doi.org/10.1016/j.biopha.2017.10.015>.
- Davidson, L. E., Shaw, S., and Benning, L. G. (2008) The kinetics and mechanisms of schwertmannite transformation to goethite and hematite under alkaline conditions. *American Mineralogist*, 93, 1326–1337, DOI: <https://doi.org/10.2138/am.2008.2761>.
- de-Bashan, L. E. and Bashan, Y. (2004) Recent advances in removing phosphorus from wastewater and its future use as fertilizer (1997-2003). *Water research*, 38, 4222–4246, DOI: <https://doi.org/10.1016/j.watres.2004.07.014>
- Demichelis, R., Raiteri, P., Gale, J. D., Quigley, D., and Gebauer, D. (2011) Stable prenucleation mineral clusters are liquid-like ionic polymers. *Nature Communication*, 2, 590, DOI: <https://doi.org/10.1038/ncomms1604>.
- Doyle, J., Oldring, K., Churchley, J., and Parsons, S. (2002) Struvite formation and the fouling propensity of different materials. *Water research*, 36, 3971–3978, DOI: [https://doi.org/10.1016/S0043-1354\(02\)00127-6](https://doi.org/10.1016/S0043-1354(02)00127-6).
- Doyle, J. D. and Parsons, S. A. (2002) Struvite formation, control and recovery. *Water research*, 36, 3925–3940, DOI: [https://doi.org/10.1016/S0043-1354\(02\)00126-4](https://doi.org/10.1016/S0043-1354(02)00126-4).
- Doyle, J. D., Oldring, K., Churchley, J., Price, C., and Parsons, S. A. (2003) Chemical Control of Struvite Precipitation. *Journal of Environmental Engineering*, 129, 419–426, DOI: [https://doi.org/10.1061/\(ASCE\)0733-9372\(2003\)129:5\(419\)](https://doi.org/10.1061/(ASCE)0733-9372(2003)129:5(419)).
- Du, J. S., Bae, Y., and Yoreo, J. J. de (2024) Non-classical crystallization in soft and organic materials. *Nature Reviews Materials*, 9, 229–248, DOI: <https://doi.org/10.1038/s41578-023-00637-y>.
- Eldjarn, K. (2024) Dittmarite from Skipton (Figure). Last access: 26 March 2024, from: <https://www.mindat.org/photo-1352063.html>.
- Elliot, J. S., Quaide, W. L., Sharp, R. F., and Lewis, L. (1958) Mineralogical Studies of Urine: The Relationship of Apatite, Brushite and Struvite to Urinary pH. *The Journal of urology*, 80, 269–271, DOI: [https://doi.org/10.1016/S0022-5347\(17\)66177-9](https://doi.org/10.1016/S0022-5347(17)66177-9).
- Erdemir, D., Lee, A. Y., and Myerson, A. S. (2019) Crystal Nucleation, in: *Handbook of industrial crystallization*, Third edition, edited by: Myerson, A. S., Erdemir, D., and Lee, A. Y., Cambridge University Press, Cambridge, 76–114, DOI: <https://doi.org/10.1017/9781139026949.003>.
- European Commission. Directorate General for Internal Market, Industry, Entrepreneurship and SMEs (2023) Study on the critical raw materials for the EU 2023: final report, Publications Office, DOI: 10.2873/12230.
- European Commission. Directorate General for Internal Market, Industry, Entrepreneurship and SMEs (2020) Study on the EU's list of critical raw materials (2020): executive summary, Publications Office, DOI: 10.2873/24089.

References

- Farhana, S. (2016) Thermal decomposition of struvite a novel approach to recover ammonia from wastewater using struvite decomposition products. M.Sc. thesis, University of British Columbia, Vancouver, 225 pp.
- Feng, T., Gull, M., Omran, A., Abbott-Lyon, H., Slavicinska, K., Pasek, M. A. (2020) Ephemeral minerals in planetary science: the case of struvite. 51st Lunar and Planetary Science Conference, The Woodlands, Texas, USA, 16-20 March, 2020, id.2080.
- Fernández-García, C., Coggins, A. J., and Powner, M. W. (2017) A Chemist's Perspective on the Role of Phosphorus at the Origins of Life. *Life* (Basel, Switzerland), 7, DOI: <https://doi.org/10.3390/life7030031>.
- Ferraris, G., Fuess, H., and Joswig, W. (1986) Neutron diffraction study of $\text{MgNH}_4\text{PO}_4 \cdot 6\text{H}_2\text{O}$ (struvite) and survey of water molecules donating short hydrogen bonds. *Acta Crystallographica B Structural Science*, 42, 253–258, DOI: <https://doi.org/10.1107/S0108768186098269>.
- Filippelli, G. M. (2008) The global phosphorous cycle: past, present and future. *Elements*, 4, 89–96. DOI: 10.2113/GSELEMENTS.4.2.89.
- Forjanés, P., Astilleros, J., and Fernández-Díaz, L. (2020) The Formation of Barite and Celestite through the Replacement of Gypsum. *Minerals*, 10, 189, DOI: <https://doi.org/10.3390/min10020189>.
- Forrest, A. L., Fattah, K. P., Mavinic, D. S., and Koch, F. A. (2008): Optimizing Struvite Production for Phosphate Recovery in WWTP. *Journal of Environmental Engineering*, 134, 395–402, DOI: [https://doi.org/10.1061/\(ASCE\)0733-9372\(2008\)134:5\(395\)](https://doi.org/10.1061/(ASCE)0733-9372(2008)134:5(395)).
- Frank, F. C. and van der Merwe, J. H. (1949) One-Dimensional Dislocations. II. Misfitting Monolayers and Oriented Overgrowth. *Proceedings of the Royal Society of London. Series A, Mathematical and Physical Sciences*, 198, 216–225, DOI: <https://doi.org/10.1098/rspa.1949.0096>.
- Frazier, A. W., Smith, J. P., and Lehr, J. R. (1966) Precipitated impurities of fertilizers prepared from wet-process phosphoric acid. *Journal of agricultural and food chemistry*, 14, 522–529, DOI: <https://doi.org/10.1021/jf60147a026>.
- Frost, R. L., Weier, M. L., and Erickson, K. L. (2004) Thermal decomposition of struvite. *Journal of Thermal Analysis and Calorimetry*, 76, 1025–1033, DOI: <https://doi.org/10.1023/B:JTAN.0000032287.08535.b3>.
- Frost, R. L., Palmer, S. J., and Pogson, R. E. (2012) Thermal Stability of newberyite $\text{Mg}(\text{PO}_3\text{OH}) \cdot 3\text{H}_2\text{O}$. *Journal of Thermal Analysis and Calorimetry*, 107, 1143–1146, DOI: <https://doi.org/10.1007/s10973-011-1593-7>.
- Frost, R. L., Weier, M. L., Martens, W. N., Henry, D. A., and Mills, S. J. (2005) Raman spectroscopy of newberyite, hannayite and struvite. *Spectrochimica acta. Part A, Molecular and biomolecular spectroscopy*, 62, 181–188, DOI: <https://doi.org/10.1016/j.saa.2004.12.024>.
- Galbraith, S. C. and Schneider, P. A. (2009) A review of struvite nucleation studies. International Conference on Nutrient Recovery from Wastewater Streams, Vancouver, Canada, 10–13 May 2009, Identifier: 991005544802507891 .
- Gao, Y., Liang, B., Chen, H., and Yin, P. (2018) An experimental study on the recovery of potassium (K) and phosphorous (P) from synthetic urine by crystallization of magnesium potassium phosphate. *Chemical Engineering Journal*, 337, 19–29, DOI: <https://doi.org/10.1016/j.cej.2017.12.077>.

References

- Gell, K., Ruijter, F., Kuntke, P., Graaff, M. de, and Smit, A. L. (2011) Safety and Effectiveness of Struvite from Black Water and Urine as a Phosphorus Fertilizer. *Journal of Agricultural Science*, 3, DOI: <https://doi.org/10.5539/jas.v3n3p67>.
- Gibbs, J. W. (1948) The Collected Works of J. Willard Gibbs: Volume 1 Thermodynamics, *The Collected Works of J. Willard Gibbs*, Yale University Press, New Haven, 434 pp.
- Graeser, S., Postl, W., Bojar, H.-P. B., Armbruster, T., Raber, T., Ettinger, K., and Walter, F. (2008) Struvite-(K), $\text{KMgPO}_4\cdot 6\text{H}_2\text{O}$, the potassium equivalent of struvite a new mineral. *European Journal of Mineralogy*, 20, 629–633, DOI: <https://doi.org/10.1127/0935-1221/2008/0020-1810>.
- Grases, F., Söhnel, O., Vilacampa, A. I., and March, J. G. (1996) Phosphates precipitating from artificial urine and fine structure of phosphate renal calculi. *Clinica chimica acta; international journal of clinical chemistry*, 244, 45–67, DOI: [https://doi.org/10.1016/0009-8981\(95\)06179-7](https://doi.org/10.1016/0009-8981(95)06179-7).
- Griffith, D. P. (1978) Struvite stones. *Kidney international*, 13, 372–382, DOI: <https://doi.org/10.1038/ki.1978.55>.
- Gull, M. (2014) Prebiotic Phosphorylation Reactions on the Early Earth. *Challenges*, 5, 193–212, DOI: <https://doi.org/10.3390/challe5020193>.
- Gull, M., Omran, A., Feng, T., and Pasek, M. A. (2020) Silicate-, Magnesium Ion-, and Urea-Induced Prebiotic Phosphorylation of Uridine via Pyrophosphate; Revisiting the Hot Drying Water Pool Scenario. *Life (Basel, Switzerland)*, 10, DOI: <https://doi.org/10.3390/life10080122>.
- Guo, H., Luković, M., Mendoza, M., Schlepütz, C. M., Griffa, M., Xu, B., Gaan, S., Herrmann, H., and Burgert, I. (2019) Bioinspired Struvite Mineralization for Fire-Resistant Wood. *American Chemical Society applied materials & interfaces*, 11, 5427–5434, DOI: <https://doi.org/10.1021/acsami.8b19967>.
- Haferburg, G., Kloess, G., Schmitz, W., and Kothe, E. (2008) “Ni-struvite” - a new biomineral formed by a nickel resistant *Streptomyces acidiscabies*. *Chemosphere*, 72, 517–523, DOI: <https://doi.org/10.1016/j.chemosphere.2008.02.050>.
- Hall, S. R. and Westbrook, J. D. (2006) Introduction. *International Tables for Crystallography*, 20, available at: <https://onlinelibrary.wiley.com/iucr/itc/ga/ch2o2v0001/sec2o2o1/>.
- Hancock, J. D. and Sharp, J. H. (1972) Method of Comparing Solid-State Kinetic Data and Its Application to the Decomposition of Kaolinite, Brucite, and BaCO_3 , *Journal of the American Ceramic Society*, 55, 74–77, DOI: <https://doi.org/10.1111/j.1151-2916.1972.tb11213.x>.
- Hanhoun, M., Montastruc, L., Azzaro-Pantel, C., Biscans, B., Frèche, M., and Pibouleau, L. (2011) Temperature impact assessment on struvite solubility product: A thermodynamic modeling approach. *Chemical Engineering Journal*, 167, 50–58, <https://doi.org/10.1016/j.cej.2010.12.001>.
- Hassel, D. M., Schiffman, P. S., and Snyder, J. R. (2001) Petrographic and geochemic evaluation of equine enteroliths. *American journal of veterinary research*, 62, 350–358, DOI: <https://doi.org/10.2460/ajvr.2001.62.350>.
- House, W. A. (1984) The kinetics of calcite precipitation and related processes. In: *Fifty-second annual report for the year ended 31st March 1984*, Freshwater Biological Association; Ambleside, UK, 75–90, URI: <http://hdl.handle.net/1834/22718>.

References

- Hövelmann, J., Stawski, T. M., Freeman, H. M., Besselink, R., Mayanna, S., Perez, J. P. H., Hondow, N. S., and Benning, L. G. (2019a) Struvite crystallisation and the effect of Co^{2+} ions. *Minerals*, 9, 503, DOI: <https://doi.org/10.3390/min9090503>.
- Hövelmann, J., Stawski, T. M., Besselink, R., Freeman, H. M., Dietmann, K. M., Mayanna, S., Pauw, B. R., and Benning, L. G. (2019b) A template-free and low temperature method for the synthesis of mesoporous magnesium phosphate with uniform pore structure and high surface area. *Nanoscale*, 11, 6939–6951, DOI: <https://doi.org/10.1039/c8nr09205b>.
- Huang, H., Li, B., Li, J., Zhang, P., Yu, W., Zhao, N., Guo, G., and Young, B. (2019) Influence of process parameters on the heavy metal (Zn^{2+} , Cu^{2+} and Cr^{3+}) content of struvite obtained from synthetic swine wastewater. *Environmental pollution* (Barking, Essex 1987), 245, 658–665, DOI: <https://doi.org/10.1016/j.envpol.2018.11.046>.
- Huang, H., Xiao, D., Liu, J., Hou, L., and Ding, L. (2015) Recovery and removal of nutrients from swine wastewater by using a novel integrated reactor for struvite decomposition and recycling. *Scientific Reports*, 5, 10183, DOI: <https://doi.org/10.1038/srep10183>.
- Hulbert, S. F. (1969) Models for solid-state reactions in powdered compacts: a review. *Journal of the British Ceramics Society*, 11–20, CRID: 1570291224443626496.
- Jeffrey, G. A. (1997) An introduction to hydrogen bonding, *Topics in physical chemistry*, Oxford University Press, New York, Oxford, 303 pp, ISBN: 9780195095494.
- Johnson, R. G. (1959) The Solubility of Magnesium Ammonium Phosphate Hexa-hydrate at 38 °C. With Considerations Pertaining to the Urine and the Formation of Urinary Calculi. *The Journal of urology*, 81, 681–690, DOI: [https://doi.org/10.1016/S0022-5347\(17\)66092-0](https://doi.org/10.1016/S0022-5347(17)66092-0).
- Johnson, W. A. and Mehl, R. F. (1939) Reaction Kinetics in Process of Nucleation and Growth. *Transactions of Transactions of the American Institute of Mining and Metallurgical Engineers*, 135, 416–458, available at: <https://cir.nii.ac.jp/crid/1571417125323686912>.
- Jordaan, E. M., Ackerman, J., and Cicek, N. (2010) Phosphorus removal from anaerobically digested swine wastewater through struvite precipitation. *Water science and technology*, 61, 3228–3234, DOI: <https://doi.org/10.2166/wst.2010.232>.
- Jun, Y.-S., Zhu, Y., Wang, Y., Ghim, D., Wu, X., Kim, D., and Jung, H. (2022) Classical and Nonclassical Nucleation and Growth Mechanisms for Nanoparticle Formation. *Annual review of physical chemistry*, 73, 453–477, DOI: <https://doi.org/10.1146/annurev-physchem-082720-100947>.
- K+S Minerals and Agriculture GmbH (2023) The right mixture works, *K+S Minerals and Agriculture GmbH*, <https://www.ks-iberia.com/es-es/agricultura/kali-academy/conocimientos/es-the-right-mixture-works/>, last access: 25 March 2024.
- Kabdaşlı, I., Parsons, S. A., and Tünay, O. (2006) Effect of major ions on induction time of struvite precipitation. *Croatica Chemica Acta*, 79, 243–251, ISSN-0011-1643.
- Karafiludis, S., Kochovski, Z., Scoppola, E., Retzmann, A., Hodoroaba, V.-D., Elshof, J. E. ten, Emmerling, F., and Stawski, T. M. (2023a) Nonclassical Crystallization Pathway of Transition Metal Phosphate Compounds. *Chemistry of Materials*, 35, 10645–10657, DOI: <https://doi.org/10.1021/acs.chemmater.3c02346>.

References

- Karafiludis, S., Scoppola, E., Wolf, S. E., Kochovski, Z., Matzdorff, D., van Driessche, A. E. S., Hövelmann, J., Emmerling, F., and Stawski, T. M. (2023b) Evidence for liquid-liquid phase separation during the early stages of Mg-struvite formation. *The Journal of Chemical Physics*, 159, DOI: <https://doi.org/10.1063/5.0166278>.
- Karpiński, P. H. and Bałdyga, J. (2019) Precipitation Processes, in: Handbook of industrial crystallization, Third edition, edited by: Myerson, A. S., Erdemir, D., and Lee, A. Y., Cambridge University Press, Cambridge, 216–265, DOI: <https://doi.org/10.1017/9781139026949.008>.
- Kasioptas, A., Geisler, T., Putnis, C. V., Perdikouri, C., and Putnis, A. (2010) Crystal growth of apatite by replacement of an aragonite precursor. *Journal of Crystal Growth*, 312, 2431–2440, DOI: <https://doi.org/10.1016/j.jcrysro.2010.05.014>.
- Kataki, S., West, H., Clarke, M., and Baruah, D. C. (2016a) Phosphorus recovery as struvite from farm, municipal and industrial waste: Feedstock suitability, methods and pre-treatments. *Waste management* (New York, N.Y.), 49, 437–454, DOI: <https://doi.org/10.1016/j.wasman.2016.01.003>.
- Kataki, S., West, H., Clarke, M., and Baruah, D. C. (2016b) Phosphorus recovery as struvite: Recent concerns for use of seed, alternative Mg source, nitrogen conservation and fertilizer potential. *Resources, Conservation and Recycling*, 107, 142–156, DOI: <https://doi.org/10.1016/j.resconrec.2015.12.009>.
- Kirsch, B. L., Richman, E. K., Riley, A. E., and Tolbert, S. H. (2004) In-Situ X-ray Diffraction Study of the Crystallization Kinetics of Mesoporous Titania Films. *Journal of Physical Chemistry B*, 12698–12706, DOI: 10.1021/jp036442p .
- Kofina, A. N. and Koutsoukos, P. G. (2005) Spontaneous Precipitation of Struvite from Synthetic Wastewater Solutions. *Crystal Growth & Design*, 5, 489–496, DOI: <https://doi.org/10.1021/cg049803e>.
- Kolmogorov, A. N. (1937) K statisticheskoy teorii kristallizatsii metallov [On the statistical theory of crystallization of metals]. *Bulletin of the Academy of Sciences of the USSR, Mathematics Series 1*, 355–359.
- Kumar, R. and Pal, P. (2015) Assessing the feasibility of N and P recovery by struvite precipitation from nutrient-rich wastewater: A review. *Environmental science and pollution research international*, 22, 17453–17464, DOI: <https://doi.org/10.1007/s11356-015-5450-2>.
- Landwirtschaftskammer Niedersachsen (2021) Struvit im Praxiseinsatz - Projekttreffen am 15.12.2021, Landwirtschaftskammer Niedersachsen, https://www.lwk-niedersachsen.de/lwk/news/38767_Struvit_im_Praxiseinsatz_-_Projekttreffen_am_15.12.2021, last access: 25 March 2024.
- Lasaga, A. C., Ed. (1998) Kinetic Theory in the Earth Sciences, Course Book, *Princeton Series in Geochemistry*, 402, Princeton University Press, Princeton, New Jersey, 822 pp., ISBN: 0-691-03748-5.
- Le Corre, K. S., Valsami-Jones, E., Hobbs, P., and Parsons, S. A. (2009) Phosphorus Recovery from Wastewater by Struvite Crystallization: A Review. *Critical Reviews in Environmental Science and Technology*, 39, 433–477, DOI: <https://doi.org/10.1080/10643380701640573>.

References

- Le Corre, K. S., Valsami-Jones, E., Hobbs, P., and Parsons, S. A. (2007a) Kinetics of struvite precipitation: effect of the magnesium dose on induction times and precipitation rates. *Environmental technology*, 28, 1317–1324, DOI: <https://doi.org/10.1080/09593332808618891>.
- Le Corre, K. S., Valsami-Jones, E., Hobbs, P., Jefferson, B., and Parsons, S. A. (2007b) Struvite crystallisation and recovery using a stainless steel structure as a seed material. *Water research*, 41, 2449–2456, DOI: <https://doi.org/10.1016/j.watres.2007.03.002>.
- Lee, A. Y., Erdemir, D., and Myerson, A. S.: Crystals and Crystal Growth, in: Handbook of industrial crystallization, Third edition, edited by: Myerson, A. S., Erdemir, D., and Lee, A. Y., Cambridge University Press, Cambridge, 32–75, DOI: <https://doi.org/10.1017/9781139026949.002>.
- Li, B., Huang, H. M., Boiarkina, I., Yu, W., Huang, Y. F., Wang, G. Q., and Young, B. R. (2019) Phosphorus recovery through struvite crystallisation: Recent developments in the understanding of operational factors. *Journal of environmental management*, 248, 109254, DOI: <https://doi.org/10.1016/j.jenvman.2019.07.025>.
- Li, D., Nielsen, M. H., Lee, J. R. I., Frandsen, C., Banfield, J. F., and Yoreo, J. J. de (2012) Direction-specific interactions control crystal growth by oriented attachment. *Science (New York, N.Y.)*, 336, 1014–1018, DOI: <https://doi.org/10.1126/science.1219643>.
- Li, H., Yao, Q.-Z., Wang, Y.-Y., Li, Y.-L., and Zhou, G.-T. (2015) Biomimetic synthesis of struvite with biogenic morphology and implication for pathological biomineralization. *Scientific Reports*, 5, 7718, DOI: <https://doi.org/10.1038/srep07718>.
- Lifshitz, I. M. and Slyozov, V. V. (1961) The kinetics of precipitation from supersaturated solid solutions. *Journal of Physics and Chemistry of Solids*, 19, 35–50, DOI: [https://doi.org/10.1016/0022-3697\(61\)90054-3](https://doi.org/10.1016/0022-3697(61)90054-3).
- Lin, J., Wang, Y., Pan, Y., Wang, S., Zhao, X., Qu, S., She, Z., Cao, K., Yuan, Z., Ma, X., Deevsalar, R., and Jia, Y. (2023) Arsenic effects and behavior during the transformation of struvite to newberyite: Implications for applications of green fertilizers. *Chemical Engineering Journal*, 458, 141396, <https://doi.org/10.1016/j.cej.2023.141396>.
- Lin, J., Chen, N., and Pan, Y.: Arsenic incorporation in synthetic struvite (NH₄MgPO₄·6H₂O): a synchrotron XAS and single-crystal EPR study. *Environmental science & technology*, 47, 12728–12735, DOI: <https://doi.org/10.1021/es402710y>.
- Lonsdale, K. and Sutor, D. J. (1966) Newberyite in ancient and modern urinary calculi: identification and space group. *Science (New York, N.Y.)*, 154, 1353–1354, DOI: <https://doi.org/10.1126/science.154.3754.1353>.
- MacAdam, J. and Jarvis, P. (2015) Water-Formed Scales and Deposits, in: Mineral scales and deposits: Scientific and technological approaches, edited by: Amjad, Z. and Demadis, K., Elsevier, Amsterdam, 3–23, DOI: <https://doi.org/10.1016/B978-0-444-63228-9.00001-2>.
- MacIvor, R. (1887) On Australian bat guano and some minerals occurring therein. *The Chemical News*, 215–216.
- Manning, D. A. C. (2008) Phosphate minerals, environmental pollution and sustainable agriculture. *Elements*, 4, 105–108, DOI: <https://doi.org/10.2113/GSELEMENTS.4.2.105>.

References

- Manzoor, M. A. P., Singh, B., Agrawal, A. K., Arun, A. B., Mujeeburahiman, M., and Rekha, P.-D. (2018a) Morphological and micro-tomographic study on evolution of struvite in synthetic urine infected with bacteria and investigation of its pathological biomineralization. *PLoS one*, 13, e0202306, DOI: <https://doi.org/10.1371/journal.pone.0202306>.
- Manzoor, M. A. P., Duwal, S. R., Mujeeburahiman, M., and Rekha, P.-D. (2018b) Vitamin C inhibits crystallization of struvite from artificial urine in the presence of *Pseudomonas aeruginosa*. *International Brazilian Journal of Urology*, official journal of the Brazilian Society of Urology, 44, 1234–1242, DOI: <https://doi.org/10.1590/S1677-5538.IBJU.2017.0656>.
- Matynia, A., Koralewska, J., Wierzbowska, B., and Piotrowski, K. (2006) The Influence of Process Parameters on Struvite Continuous Crystallization Kinetics. *Chemical Engineering Communications*, 193, 160–176, DOI: <https://doi.org/10.1080/009864490949008>.
- Matzdorff, D. C. N. (2020) Up-cycling Urinary Stones: A study on the potential of the waste material struvite ($\text{NH}_4\text{MgPO}_4 \cdot 6\text{H}_2\text{O}$) through the production of mesoporous, high surface metal phosphates and the effect of transition metals., Master's thesis, Mathematisch-Naturwissenschaftliche Fakultät Institut für Geowissenschaften, University Potsdam, Potsdam, 87 pp.
- Mehta, C. M. and Batstone, D. J. (2013) Nucleation and growth kinetics of struvite crystallization. *Water research*, 47, 2890–2900, DOI: <https://doi.org/10.1016/j.watres.2013.03.007>.
- Milke, R., Neusser, G., Kolzer, K., and Wunder, B. (2013) Very little water is necessary to make a dry solid silicate system wet. *Geology*, 41, 247–250, DOI: <https://doi.org/10.1130/G33674.1>.
- Mohajit, Bhattarai, K. K., Taiganides, E., and Yap, B. C. (1989) Struvite deposits in pipes and aerators. *Biological Wastes*, 30, 133–147, DOI: [https://doi.org/10.1016/0269-7483\(89\)90067-0](https://doi.org/10.1016/0269-7483(89)90067-0).
- Moragaspiya, C., Rajapakse, J., and Millar, G. J. (2019) Effect of Ca:Mg ratio and high ammoniacal nitrogen on characteristics of struvite precipitated from waste activated sludge digester effluent. *Journal of environmental sciences (China)*, 86, 65–77, DOI: <https://doi.org/10.1016/j.jes.2019.04.023>.
- Mulders, J. J., Tobler, D. J., and Oelkers, E. H. (2021) Siderite nucleation pathways as a function of aqueous solution saturation state at 25 °C. *Chemical Geology*, 559, 119947, DOI: <https://doi.org/10.1016/j.chemgeo.2020.119947>.
- Mullin, J. W. (2001) Crystallization, 4th ed., *Elsevier Science*, Jordan Hill, 611 pp., ISBN: 9780080530116.
- Münch, E. V. and Barr, K. (2001) Controlled struvite crystallisation for removing phosphorus from anaerobic digester sidestreams. *Water research*, 35, 151–159, DOI: [https://doi.org/10.1016/S0043-1354\(00\)00236-0](https://doi.org/10.1016/S0043-1354(00)00236-0).
- Nelson, N. O., Mikkelsen, R. L., and Hesterberg, D. L. (2003) Struvite precipitation in anaerobic swine lagoon liquid: effect of pH and Mg:P ratio and determination of rate constant. *Bioresour. Technol.*, 89, 229–236, DOI: [https://doi.org/10.1016/S0960-8524\(03\)00076-2](https://doi.org/10.1016/S0960-8524(03)00076-2).
- Novotny, C. (2011) Ammonia removal and recovery using heated struvite as an adsorbent, M.Sc. thesis, University of British Columbia, Vancouver, 179 pp.
- Oelkers, E. H. and Valsami-Jones, E. (2008) Phosphate mineral reactivity and global sustainability. *Elements*, 4, 83–88, DOI: <https://doi.org/10.2113/GSELEMENTS.4.2.83>.

References

- Ohlinger, K. N., Young, T. M., and Schroeder, E. D. (1998) Predicting struvite formation in digestion. *Water research*, 32, 3607–3614, DOI: [https://doi.org/10.1016/S0043-1354\(98\)00123-7](https://doi.org/10.1016/S0043-1354(98)00123-7).
- Ohlinger, K. N., E, P., Young, T. M., and Schroeder, E. D. (1999) Kinetics Effects on Preferential Struvite Accumulation in Wastewater. *Journal of Environmental Engineering*, 125, 730–737, DOI: [https://doi.org/10.1061/\(ASCE\)0733-9372\(1999\)125:8\(730\)](https://doi.org/10.1061/(ASCE)0733-9372(1999)125:8(730)).
- OriginLab Corporation (1991–2023) Origin. Version 2023b. Northampton, Massachusetts, USA.
- Palmer, D. (2014) CrystalMaker. CrystalMaker Software Ltd, Oxfordshire, England, UK.
- Parsons, S., Flack, H. D., and Wagner, T. (2013) Use of intensity quotients and differences in absolute structure refinement. *Acta crystallographica Section B, Structural science, crystal engineering and materials*, 69, 249–259, DOI: <https://doi.org/10.1107/S2052519213010014>.
- Pasteris, J. D., Wopenka, B., and Valsami-Jones, E. (2008) Bone and tooth mineralization: why apatite?, *Elements*, 4, 97–103, DOI: <https://doi.org/10.2113/GSELEMENTS.4.2.97>.
- Paul, I., Varghese, G., and Ittyachen, M. A. (2002) Thermal decomposition studies of struvites, *Indian Journal of Pure & Applied Physics*, 40, 664–669, ISSN: 0975-1041.
- Penn, R. L. and Banfield, J. F. (1998) Imperfect oriented attachment: dislocation generation in defect-free nanocrystals. *Science (New York, N.Y.)*, 281, 969–971, DOI: <https://doi.org/10.1126/science.281.5379.969>.
- Pérez-García, I., Rivadeneyra, M. A., and Ramos-Cormenzana (1989) The influence of pH on struvite formation by bacteria. *Chemosphere*, 18, 1633–1638, DOI: [https://doi.org/10.1016/0045-6535\(89\)90053-2](https://doi.org/10.1016/0045-6535(89)90053-2).
- Perwitasari, D. S., Muryanto, S., Jamari, J., and Bayuseno, A. P. (2018) Kinetics and morphology analysis of struvite precipitated from aqueous solution under the influence of heavy metals: Cu²⁺, Pb²⁺, Zn²⁺. *Journal of Environmental Chemical Engineering*, 6, 37–43, DOI: <https://doi.org/10.1016/j.jece.2017.11.052>.
- Polat, S. and Sayan, P. (2020) Preparation, characterization and kinetic evaluation of struvite in various carboxylic acids. *Journal of Crystal Growth*, 531, 125339, DOI: <https://doi.org/10.1016/j.jcrysgro.2019.125339>.
- Pöml, P., Menneken, M., Stephan, T., Niedermeier, D., Geisler, T., and Putnis, A. (2007) Mechanism of hydrothermal alteration of natural self-irradiated and synthetic crystalline titanate-based pyrochlore. *Geochimica et Cosmochimica Acta*, 71, 3311–3322, DOI: <https://doi.org/10.1016/j.gca.2007.03.031>.
- Prywer, J. and Olszynski, M. (2013) Influence of disodium EDTA on the nucleation and growth of struvite and carbonate apatite. *Journal of Crystal Growth*, 375, 108–114, <https://doi.org/10.1016/j.jcrysgro.2013.04.027>.
- Prywer, J., Sieroń, L., and Czyłkowska, A. (2019) Struvite Grown in Gel, Its Crystal Structure at 90 K and Thermoanalytical Study. *Crystals*, 9, 89, DOI: <https://doi.org/10.3390/cryst9020089>.
- Putnis, A. (2009) Mineral Replacement Reactions, *Reviews in Mineralogy and Geochemistry*, 70, 87–124, DOI: <https://doi.org/10.2138/rmg.2009.70.3>.
- Putnis, A. (2021) Fluid–mineral interactions: controlling coupled mechanisms of reaction, mass transfer and deformation. *Journal of Petrology*, 62, DOI: <https://doi.org/10.1093/petrology/egab092>.

References

- Putnis, C. V., Geisler, T., Schmid-Beurmann, P., Stephan, T., and Giampaolo, C. (2007) An experimental study of the replacement of leucite by analcime. *American Mineralogist*, 92, 19–26, DOI: <https://doi.org/10.2138/am.2007.2249>.
- Quintana, M., Sánchez, E., Colmenarejo, M. F., Barrera, J., García, G., and Borja, R. (2005) Kinetics of phosphorus removal and struvite formation by the utilization of by-product of magnesium oxide production. *Chemical Engineering Journal*, 111, 45–52, DOI: <https://doi.org/10.1016/j.cej.2005.05.005>.
- Rahaman, M. S., Ellis, N., and Mavinic, D. S. (2008) Effects of various process parameters on struvite precipitation kinetics and subsequent determination of rate constants. *Water science and technology*, 57, 647–654, DOI: <https://doi.org/10.2166/wst.2008.022>.
- Rahaman, M.S., Mavinic, D.S., Meikleham, A., Ellis, N. (2014) Modeling phosphorus removal and recovery from anaerobic digester supernatant through struvite crystallization in a fluidized bed reactor. *Water Research* 51, 1–10, DOI: 10.1016/j.watres.2013.11.048.
- Ramlogan, M. V. and Rouff, A. A. (2016) An investigation of the thermal behavior of magnesium ammonium phosphate hexahydrate. *Journal of Thermal Analysis and Calorimetry*, 123, 145–152, DOI: <https://doi.org/10.1007/s10973-015-4860-1>.
- Rawn, A. M., Banta, A., and Pomeroy, R. (1939) Multiple stage sewage digestion. *Transactions of the American Society of Agricultural Engineers*, 105, 93–132, DOI: <https://doi.org/10.1061/TACEAT.0005148>.
- Rigaku Oxford Diffraction (2021) CrysAlis PRO. Rigaku Oxford Diffraction, Yarnton, Oxfordshire, England, UK.
- Rodrigues, D. M., do Amaral Fragoso, R., Carvalho, A. P., Hein, T., and Guerreiro de Brito, A. (2019) Recovery of phosphates as struvite from urine-diverting toilets: optimization of pH, Mg:PO₄ ratio and contact time to improve precipitation yield and crystal morphology. *Water science and technology*, 80, 1276–1286, DOI: <https://doi.org/10.2166/wst.2019.371>.
- Rodriguez-Blanco, J. D., Shaw, S., and Benning, L. G. (2011) The kinetics and mechanisms of amorphous calcium carbonate (ACC) crystallization to calcite, via vaterite. *Nanoscale*, 3, 265–271, DOI: <https://doi.org/10.1039/c0nr00589d>.
- Ronteltap, M. (2009) Phosphorus recovery from source-separated urine through the precipitation of struvite. Doctoral Thesis, Swiss Federal Institute of Technology, Zurich, Switzerland, 101 pp.
- Ronteltap, M., Maurer, M., Hausherr, R., and Gujer, W. (2010) Struvite precipitation from urine - Influencing factors on particle size. *Water research*, 44, 2038–2046, DOI: <https://doi.org/10.1016/j.watres.2009.12.015>.
- Rouff, A. A., Ma, N., and Kustka, A. B. (2016) Adsorption of arsenic with struvite and hydroxylapatite in phosphate-bearing solutions. *Chemosphere*, 146, 574–581, DOI: <https://doi.org/10.1016/j.chemosphere.2015.12.061>.
- Roza-Llera, A., Jiménez, A., and Fernández-Díaz, L. (2023) Mechanism and kinetics of the pseudomorphic replacement of anhydrite by calcium phosphate phases at hydrothermal conditions. *American Mineralogist*, 108, 1708–1719, DOI: <https://doi.org/10.2138/am-2022-8592>.

References

- Ruiz-Agudo, E., Putnis, C. V., and Putnis, A. (2014) Coupled dissolution and precipitation at mineral–fluid interfaces. *Chemical Geology*, 383, 132–146, DOI: <https://doi.org/10.1016/j.chemgeo.2014.06.007>.
- Ruiz-Agudo, E., Kudłacz, K., Putnis, C. V., Putnis, A., and Rodriguez-Navarro, C. (2013) Dissolution and carbonation of portlandite $\text{Ca}(\text{OH})_2$ single crystals. *Environmental science & technology*, 47, 11342–11349, DOI: <https://doi.org/10.1021/es402061c>.
- S. E. Aguiar (2019) Kinetics based characterization of struvite dissolution. Master Thesis, Civil Engineering, University of Illinois, Urbana, Illinois, USA, 72 pp.
- Sánchez-Pastor, N., Oehlerich, M., Astilleros, J. M., Kaliwoda, M., Mayr, C. C., Fernández-Díaz, L., and Schmahl, W. W. (2016) Crystallization of ikaite and its pseudomorphic transformation into calcite: Raman spectroscopy evidence. *Geochimica et Cosmochimica Acta*, 175, 271–281, <https://doi.org/10.1016/j.gca.2015.12.006>.
- Sarkar, A. K. (1991) Hydration/dehydration characteristics of struvite and dittmarite pertaining to magnesium ammonium phosphate cement systems. *Journal of Materials Science*, 26, 2514–2518, DOI: <https://doi.org/10.1007/BF01130204>.
- Shaddel, S., Grini, T., Andreassen, J.-P., Østerhus, S. W., and Ucar, S. (2020) Crystallization kinetics and growth of struvite crystals by seawater versus magnesium chloride as magnesium source: towards enhancing sustainability and economics of struvite crystallization. *Chemosphere*, 256, 126968, DOI: <https://doi.org/10.1016/j.chemosphere.2020.126968>.
- Sheldrick, G. M. (2015) Crystal structure refinement with SHELXL. *Acta Crystallographica C*, 71, 3–8, DOI: <https://doi.org/10.1107/S2053229614024218>.
- Sinha, A., Singh, A., Kumar, S., Khare, S. K., and Ramanan, A. (2014) Microbial mineralization of struvite: a promising process to overcome phosphate sequestering crisis. *Water research*, 54, 33–43, DOI: <https://doi.org/10.1016/j.watres.2014.01.039>.
- Snow, M. R., Pring, A., and Allen, N. (2014) Minerals of the Wooltana Cave, Flinders Ranges, South Australia. *Transactions of the Royal Society of South Australia*, 138, 214–230, DOI: <https://doi.org/10.1080/03721426.2014.11649009>.
- Söhnle, O. and Mullin, J. W. (1988) Interpretation of crystallization induction periods. *Journal of Colloid and Interface Science*, 123, 43–50, DOI: [https://doi.org/10.1016/0021-9797\(88\)90219-6](https://doi.org/10.1016/0021-9797(88)90219-6).
- Stefov, V., Šoptrajanov, B., Kuzmanovski, I., Lutz, H. D., and Engelen, B. (2005) Infrared and Raman spectra of magnesium ammonium phosphate hexahydrate (struvite) and its isomorphous analogues. III. Spectra of protiated and partially deuterated magnesium ammonium phosphate hexahydrate. *Journal of Molecular Structure*, 752, 60–67, DOI: <https://doi.org/10.1016/j.molstruc.2005.05.040>.
- Stefov, V., Šoptrajanov, B., Spirovski, F., Kuzmanovski, I., Lutz, H., and Engelen, B. (2004) Infrared and Raman spectra of magnesium ammonium phosphate hexahydrate (struvite) and its isomorphous analogues. I. Spectra of protiated and partially deuterated magnesium potassium phosphate hexahydrate. *Journal of Molecular Structure*, 689, 1–10, DOI: <https://doi.org/10.1016/j.molstruc.2003.08.019>.
- Stranski, I. N. and Krastanow, L. (1937) Zur Theorie der orientierten Ausscheidung von Ionenkristallen aufeinander. *Monatshefte fuer Chemie*, 71, 351–364, DOI: <https://doi.org/10.1007/BF01798103>.

References

- Stratful, I., Scrimshaw, M., and Lester, J. (2001) Conditions influencing the precipitation of magnesium ammonium phosphate. *Water research*, 35, 4191–4199, DOI: [https://doi.org/10.1016/S0043-1354\(01\)00143-9](https://doi.org/10.1016/S0043-1354(01)00143-9).
- Sutor, D. J. (1968) Newberyite-its formation in human urinary calculi. *Nature*, 218, 295, DOI: <https://doi.org/10.1038/218295a0>.
- Taddeo, R., Honkanen, M., Kolppo, K., and Lepistö, R. (2018) Nutrient management via struvite precipitation and recovery from various agroindustrial wastewaters: Process feasibility and struvite quality. *Journal of environmental management*, 212, 433–439, DOI: <https://doi.org/10.1016/j.jenvman.2018.02.027>.
- Tamimi, F., Le Nihouannen, D., Bassett, D. C., Ibasco, S., Gbureck, U., Knowles, J., Wright, A., Flynn, A., Komarova, S. V., and Barralet, J. E. (2011) Biocompatibility of magnesium phosphate minerals and their stability under physiological conditions, *Acta biomaterialia*, 7, 2678–2685, DOI: <https://doi.org/10.1016/j.actbio.2011.02.007>.
- Tansel, B., Lunn, G., and Monje, O. (2018) Struvite formation and decomposition characteristics for ammonia and phosphorus recovery: A review of magnesium-ammonia-phosphate interactions. *Chemosphere*, 194, 504–514, DOI: <https://doi.org/10.1016/j.chemosphere.2017.12.004>.
- Tendler, L. (2021) Erfahrungsaustausch Struvit im Ackerbau: digitales Treffen der Pilotbetriebe, *Landwirtschaftskammer Niedersachsen*, last access: 25 March 2024, from: https://www.lwk-niedersachsen.de/lwk/news/38767_Struvit_im_Praxiseinsatz_-_Projekttreffen_am_15.12.2021.
- Teschemacher, E. F. (1846) An account of various substances found in the guano deposits and in their vicinity. *The London, Edinburgh, and Dublin Philosophical Magazine and Journal of Science*, 28, 546–550, DOI: <https://doi.org/10.1080/14786444608645468>.
- Tilley, E., Atwater, J., and Mavinic, D. (2008) Recovery of struvite from stored human urine. *Environmental technology*, 29, 797–806, DOI: <https://doi.org/10.1080/09593330801987129>.
- Toby, B. H. (2006) R factors in Rietveld analysis: How good is good enough?, *Powder Diffraction*, 21, 67–70, DOI: <https://doi.org/10.1154/1.2179804>.
- Türker, M. and Celen, I. (2007) Removal of ammonia as struvite from anaerobic digester effluents and recycling of magnesium and phosphate. *Bioresource technology*, 98, 1529–1534, DOI: <https://doi.org/10.1016/j.biortech.2006.06.026>.
- Ulex, G. L. (1845) On Struvite, a new Mineral. *Memoirs and proceedings of the Chemical society*, 3, 106–111, DOI: <https://doi.org/10.1039/MP8450300106>.
- Uysal, A., Yilmazel, Y. D., and Demirer, G. N. (2010) The determination of fertilizer quality of the formed struvite from effluent of a sewage sludge anaerobic digester. *Journal of hazardous materials*, 181, 248–254, DOI: <https://doi.org/10.1016/j.jhazmat.2010.05.004>.
- Vogel, T., Nelles, M., and Eichler-Löbermann, B. (2015) Phosphorus application with recycled products from municipal waste water to different crop species. *Ecological Engineering*, 83, 466–475, DOI: <https://doi.org/10.1016/j.ecoleng.2015.06.044>.
- Volkman, R., Münchhalphen, M., and Benning, L. G. (2024) A new structure determination of the magnesium phosphate mineral struvite (MgNH₄PO₄·6H₂O) at 100 K. *EarthArXiv*, DOI: <https://doi.org/10.31223/X5KQ4F>.

References

- Volmer, M. and Weber, A. (1926) Keimbildung in übersättigten Gebilden. *Zeitschrift für Physikalische Chemie*, 119U, 277–301, DOI: <https://doi.org/10.1515/zpch-1926-11927>.
- Volmer, M. (1939) Kinetik der Phasenbildung. *Die chemische Reaktion*, 4, Verlag Theodor Steinkopff, Dresden, 220 pp, DOI: 10.1002/ange.19390523006.
- Voorhees, P. W. (1985) The theory of Ostwald ripening. *Journal of Statistical Physics*, 38, 231–252, DOI: <https://doi.org/10.1007/BF01017860>.
- Wagner, C. (1961) Theorie der Alterung von Niederschlägen durch Umlösen (Ostwald-Reifung). *Zeitschrift für Elektrochemie*, 65, 581–591, DOI: <https://doi.org/10.1002/bbpc.19610650704>.
- Wang, Z., Zhang, Y., Zhang, J., Deng, Q., and Liang, H. (2021) Recent advances on the mechanisms of kidney stone formation (Review). *International Journal of Molecular Medicine*, 48, 1–10, DOI: <https://doi.org/10.3892/ijmm.2021.4982>.
- Warr, L. N. (2021) IMA–CNMNC approved mineral symbols, *Mineralogical magazine*, 85, 291–320, DOI: <https://doi.org/10.1180/mgm.2021.43>.
- WaveMetrics, Inc. (1988–2019) Igor Pro 8. Version 8.04, WaveMetrics, Inc., Lake Oswego, Oregon, USA.
- Weil, M. (2008) The struvite-type compounds $M [Mg(H_2O)_6](XO_4)_2$, where $M = Rb, Tl$ and $X = P, As$. *Crystal Research and Technology*, 43, 1286–1291, DOI: <https://doi.org/10.1002/crat.200800403>.
- Weiner, S., Sagi, I., and Addadi, L. (2005) Structural biology. Choosing the crystallization path less traveled. *Science (New York, N.Y.)*, 309, 1027–1028, DOI: <https://doi.org/10.1126/science.1114920>.
- Whitaker, A. (1968) The decomposition of struvite. *Mineralogical magazine* 36, 820–824, DOI: <https://doi.org/10.1180/minmag.1968.036.282.09>.
- Whitaker, A. and Jeffery, J. W. (1970a) The crystal structure of struvite, $MgNH_4PO_4 \cdot 6H_2O$. *Acta Crystallographica B Structural Science*, 26, 1429–1440, DOI: <https://doi.org/10.1107/S0567740870004284>.
- Whitaker, A. and Jeffery, J. W. (1970b) X-ray evidence for a single-bonded rotating ammonium ion in struvite. *Acta Crystallographica B Structural Science*, 26, 1440–1444, DOI: <https://doi.org/10.1107/S0567740870004296>.
- Wilsenach, J. A., Schuurbijs, C. A. H., and van Loosdrecht, M. C. M. (2007) Phosphate and potassium recovery from source separated urine through struvite precipitation. *Water research*, 41, 458–466, DOI: <https://doi.org/10.1016/j.watres.2006.10.014>.
- Wilsenach, J. A., Maurer, M., Larsen, T. A., and van Loosdrecht, M. C. M. (2003) From waste treatment to integrated resource management. *Water science and technology*, 48, 1–9, DOI: <https://doi.org/10.2166/wst.2003.0002>.
- Xu, K., Li, J., Zheng, M., Zhang, C., Xie, T., and Wang, C. (2015) The precipitation of magnesium potassium phosphate hexahydrate for P and K recovery from synthetic urine. *Water research*, 80, 71–79, DOI: <https://doi.org/10.1016/j.watres.2015.05.026>.
- Yetilmezsoy, K., Kocak, E., Akbin, H. M., and Özçimen, D. (2018) Utilization of struvite recovered from high-strength ammonium-containing simulated wastewater as slow-release fertilizer and fire-retardant barrier. *Environmental technology*, 41, 153–170, DOI: <https://doi.org/10.1080/09593330.2018.1491642>.

References

- Yetilmezsoy, K., Ilhan, F., Kocak, E., and Akbin, H. M. (2017) Feasibility of struvite recovery process for fertilizer industry: a study of financial and economic analysis. *Journal of Cleaner Production*, 152, 88–102, DOI: <https://doi.org/10.1016/j.jclepro.2017.03.106>.
- Yoreo, J. J. de, Gilbert, P. U. P. A., Sommerdijk, N. A. J. M., Penn, R. L., Whitelam, S., Joester, D., Zhang, H., Rimer, J. D., Navrotsky, A., Banfield, J. F., Wallace, A. F., Michel, F. M., Meldrum, F. C., Cölfen, H., and Dove, P. M. (2015) Crystal Growth. Crystallization by particle attachment in synthetic, biogenic, and geologic environments. *Science* (New York, N.Y.), 349, aaa6760, DOI: <https://doi.org/10.1126/science.aaa6760>.

Appendix A Supplementary information to Chapter 3

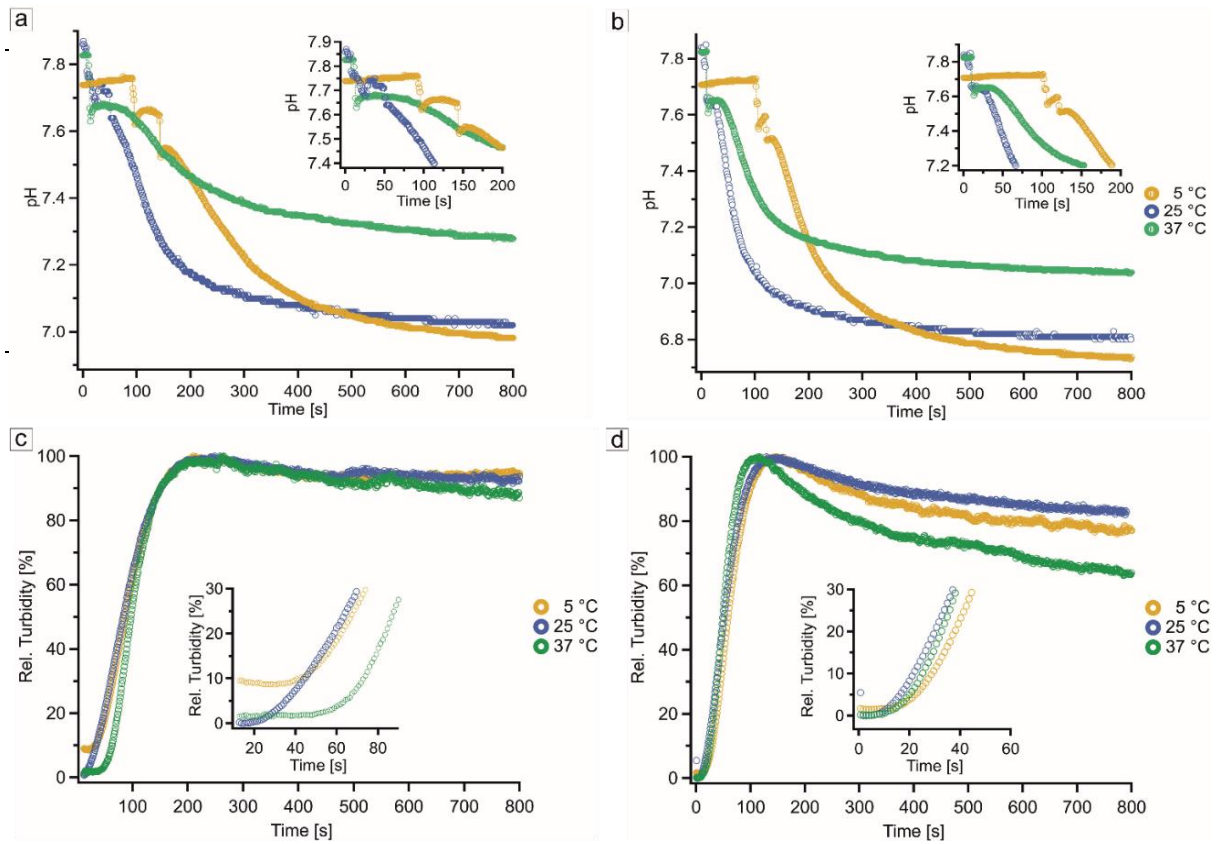


Fig. A1 a) pH curves at a solution concentration of 6 mM. b) pH curves at a solution concentration of 8 mM. c) Turbidity curves at a solution concentration of 6 mM. d) Turbidity curves at a solution concentration of 8 mM.

Tab. A1 Induction times and rate constants k for the crystallisation of struvite from pure salt solutions at different temperatures from the literature. Note that all induction times were converted into units of min and k values into units of s^{-1} for better comparability.

| Reference | Solution concentration/supersaturation ratio (SSR) | Experimental temperature [°C] | Induction time [min] | Rate constant k |
|--------------------------|--|-------------------------------|---------------------------------|-------------------|
| This study | 5 mM | 5 | 0.63 | $0.25 s^{-1}$ |
| | 6 mM | | 0.53 | |
| | 8 mM | | 0.30 | |
| | 15 mM | | 0.16 | |
| | 30 mM | | 0.42* | |
| | 30 mM | 15 | 0.43* | $0.30 s^{-1}$ |
| | 5 mM | 25 | 0.70 | $0.26 s^{-1}$ |
| | 6 mM | | 0.23 | |
| | 8 mM | | 0.08 | |
| | 15 mM | | 0.18 | |
| | 30 mM | | 0.16, 0.45* | |
| | 5 mM | 37 | 1.50 | $0.78 s^{-1}$ |
| | 6 mM | | 0.73 | |
| | 8 mM | | 0.33 | |
| | 15 mM | | 0.32 | |
| 30 mM | 0.42* | | | |
| 15mM | 37 | 0.32 | $4.1 (mmol/l)^{-1} s^{-1}^{**}$ | |
| 30 mM | 50 | 0.43* | – | |
| Hövelmann et al. (2019a) | 3.05 mM | 25 | 3.50 | – |
| | 6.10 mM | | 0.30 | |

| Reference | Solution concentration/supersaturation ratio (SSR) | Experimental temperature [°C] | Induction time [min] | Rate constant k |
|--------------------------------|---|-------------------------------|----------------------|---|
| Crutchik and Garrido (2016)*** | 6.0 mM NH ₄ ⁺ , 2.2 mM Mg ²⁺ , 2.0 mM PO ₄ ³⁻ , N:Mg:P = 3:1:1 | 25 | 20.00 | 6.18·10 ⁻³ mol m ⁻² s ⁻¹ |
| | N:Mg:P = 3:1:1 | 30 | – | 7.50·10 ⁻³ mol m ⁻² s ⁻¹ |
| | N:Mg:P = 3:1:1 | 35 | 45.00 | 9.24·10 ⁻³ mol m ⁻² s ⁻¹ |
| Rahaman et al. (2008) | SSR = 9.64 | | - | 7322.4 s ⁻¹ |
| | SSR = 4.83 | 20 | - | 6177.6 s ⁻¹ |
| | SSR = 2.44 | | - | 2484.0 s ⁻¹ |
| Le Corre et al. (2007a) | Mg: 1.20 mM, Mg:N:P = 1:2:2 | | 5.00 | 33840 s ⁻¹ |
| | Mg: 1.35 mM, Mg:N:P = 1:2:2 | | – | 38520 s ⁻¹ |
| | Mg: 1.52 mM, Mg:N:P = 1:2:2 | | – | 43920 s ⁻¹ |
| | Mg: 1.64 mM, Mg:N:P = 1:2:2 | | 1.80 | 45000 s ⁻¹ |
| | Mg: 1.76 mM, Mg:N:P = 1:2:2 | 25 | – | 47160 s ⁻¹ |
| | Mg: 1.96 mM, Mg:N:P = 1:2:2 | | 0.80 | 45720 s ⁻¹ |
| | Mg: 2.30 mM, Mg:N:P = 1:2:2 | | 0.50 | 48240 s ⁻¹ |
| | Mg: 3.5 mM, Mg:N:P = 1:2:2 | | – | 56520 s ⁻¹ |

| Reference | Solution concentration/supersaturation ratio (SSR) | Experimental temperature [°C] | Induction time [min] | Rate constant k |
|--|--|-------------------------------|----------------------|-----------------|
| Bouropoulos and Koutsoukos (2000) | SSR = 3.33 | 25 | 6.00 | – |
| | SSR = 3.33 | | 6.00 | |
| | SSR = 3.04 | | 14.00 | |
| | SSR = 2.76 | | 19.00 | |
| | SSR = 2.51 | | 27.00 | |
| | SSR = 2.27 | | 42.00 | |
| | SSR = 2.05 | | 51.00 | |
| | SSR = 1.84 | | 71.00 | |
| | SSR = 1.49 | | 90.00 | |
| | SSR = 1.13 | 125.00 | | |
| Ohlinger et al. (1999) | 4-20 mM, SSR = 1.6-3.1 | 22 | 0.20-38.00 | – |

*Value derived from WAXS measurements.

**Value derived from Monte Carlo simulation for this specific dataset.

***Rate constants were derived for the heterogeneous crystallisation of struvite using seeding.

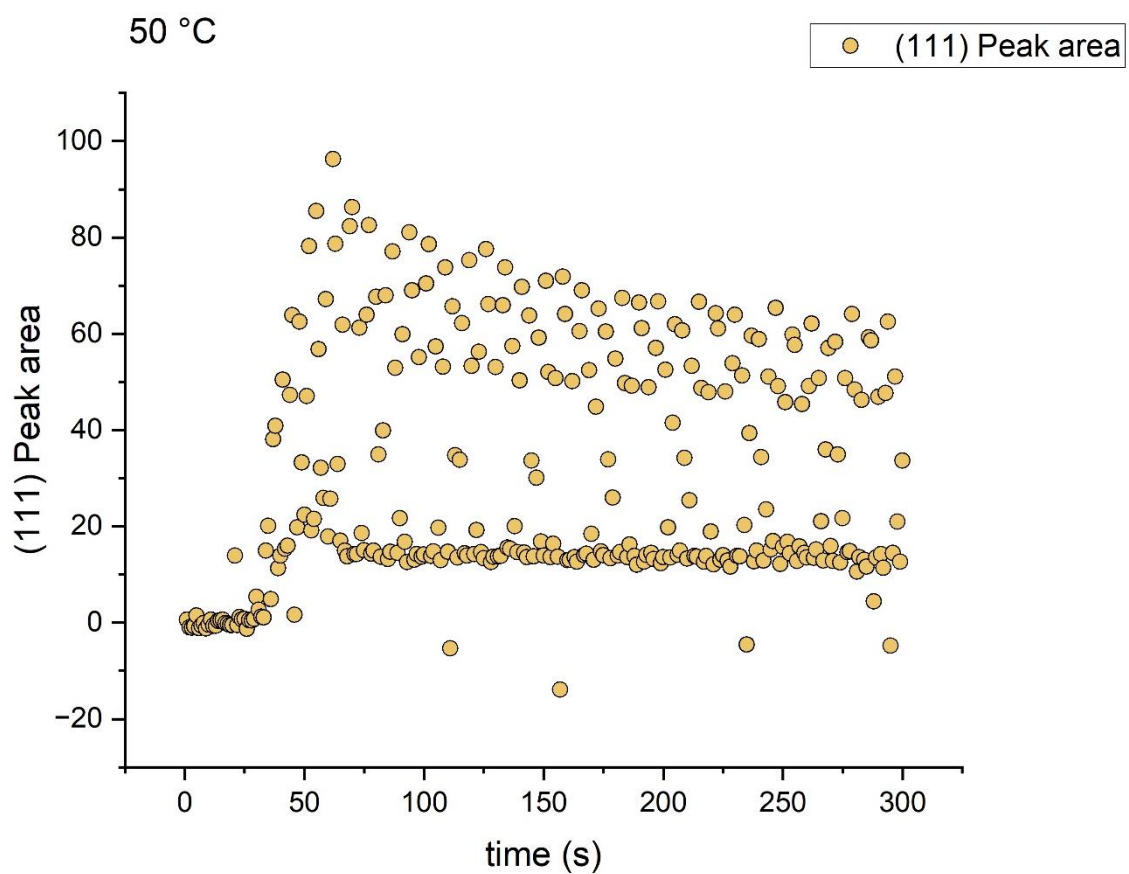


Fig. A2 Reaction progress plot derived from the (111) peak area WAXS data for the crystallisation of struvite at 50 °C.

Appendix B Supplementary information to Chapter 5

Table B1 All transformation experiments including reaction temperatures and durations. Sample type abbreviations: PWD: powder, SC: single crystals, TS: thin sections.

| Sample name | Sample type | Transformation temperature [°C] | Transformation duration [weeks] |
|----------------------|-------------|---------------------------------|---------------------------------|
| Stru_New_22_1h_op | PWD | 22 | 0.006 |
| Stru_New_22_1d_op | PWD | 22 | 0.14 |
| Stru_New_22_3d_op | PWD | 22 | 0.43 |
| Stru_New_22_1w_op | PWD, SC | 22 | 1 |
| Stru_New_22_1mo_op | PWD, SC | 22 | 4 |
| Stru_New_22_2mo_op | PWD | 22 | 8 |
| Stru_New_22_3mo_op | PWD, SC, TS | 22 | 12 |
| Stru_New_22_4-5mo_op | PWD | 22 | 18 |
| Stru_New_22_6mo_op | PWD, SC | 22 | 24 |
| Stru_New_22_8mo_op | PWD | 22 | 32 |
| Stru_New_22_10mo_op | PWD, SC | 22 | 40 |
| Stru_New_37_1h_op | PWD | 37 | 0.006 |
| Stru_New_37_1d_op | PWD | 37 | 0.14 |
| Stru_New_37_3d_op | PWD | 37 | 0.43 |
| Stru_New_37_1w_op | PWD | 37 | 1 |
| Stru_New_37_1mo_op | PWD, SC, TS | 37 | 4 |
| Stru_New_37_3mo_op | PWD, SC, TS | 37 | 12 |
| Stru_New_37_6mo_op | PWD, SC | 37 | 24 |
| Stru_New_37_8mo_op | PWD | 37 | 32 |
| Stru_New_37_10mo_op | PWD, SC | 37 | 40 |
| Stru_New_60_1h_op | PWD | 60 | 0.006 |
| Stru_New_60_16h_op | PWD | 60 | 0.10 |
| Stru_New_60_20h_op | PWD | 60 | 0.12 |

| Sample name | Sample type | Transformation temperature [°C] | Transformation duration [weeks] |
|--------------------|-------------|------------------------------------|------------------------------------|
| Stru_New_60_1d_op | PWD, SC, TS | 60 | 0.14 |
| Stru_New_60_3d_op | PWD, SC | 60 | 0.43 |
| Stru_New_60_4d_op | PWD | 60 | 0.57 |
| Stru_New_60_5d_op | PWD | 60 | 0.71 |
| Stru_New_60_1w_op | PWD, SC | 60 | 1 |
| Stru_New_60_2w_op | PWD | 60 | 2 |
| Stru_New_60_1mo_op | PWD, SC, TS | 60 | 4 |
| Stru_New_60_2mo_op | PWD | 60 | 8 |
| Stru_New_60_3mo_op | PWD, SC | 60 | 12 |
| Stru_New_60_6mo_op | PWD, SC | 60 | 24 |

Table B2 XRD instrument parameters and statistic indicators for Rietveld refinements as suggested by Toby (2006).

| | |
|---|--|
| Instrument | STOE STADI P |
| X-ray tube | Cu anode, 40 kV, 40 mA |
| Incident beam optic | Curved 111-cut Ge monochromator |
| Diffraction geometry | Modified Debye-Scherrer ("STOE Transmission geometry") |
| Detector | DECTRIS MYTHEN R HPC |
| 2 theta range (°) | 0–83.985 |
| 2 theta step size (°) | 6 |
| Counting time/step/repetition (s) | 32/18 repetitions |
| Rietveld analysis software | GSAS-II Version 5361 |
| GOF (\emptyset) | 0.040–0.090 |
| Rwp (\emptyset) | 3.561–7.003 |
| Durbin-Watson statistic (\emptyset) | 0.200–0.766 |

Table B3 FTIR and Raman spectroscopy instrument and measurement parameters.

| <i>Fourier-transform IR</i> | | <i>Raman</i> | | |
|-----------------------------|-----------------------|-------------------|--|------------|
| Instrument | Thermo Fisher Nicolet | Instrument | Horiba | Jobin Yvon |
| | iS5 FTIR | | LabRAM HR800 VIS | |
| Accessory | iD7 Diamond-ATR | Microscope | Olympus BXFM/ Olympus BX41 | |
| Window type | KBr | Detector | CCD Detector 2048×512 pixel/1024×256 pixel | |
| Spectral resolution | 4 cm ⁻¹ | Laser | Cobolt Blues™ 50 mW/25 mW | |
| | | Wavelength | 473 nm | |
| | | Grating | 1800 lines/mm | |

Table B4 List of atom bands detected and assigned using Raman spectroscopy.

| Phase | Wavenumbers [cm ⁻¹] | Assignments |
|------------|---------------------------------|-----------------------|
| | 275 | MgO |
| | 300 | MgO |
| Struvite | 413 | HPO ₄ |
| | 448 | HPO ₄ |
| | 570 | HPO ₄ |
| | 945 | PO ₃ , POH |
| | 2800–3000 | NH ₄ |
| | 3000–3400 | OH, H ₂ O |
| | 393 | HPO ₄ |
| Newberyite | 514 | HPO ₄ |
| | 541 | HPO ₄ |
| | 866 | HPO ₄ |
| | 980 | HPO ₄ |
| | 3200–3500 | OH, H ₂ O |
| | 413 | HPO ₄ |
| Dittmarite | 448 | HPO ₄ |
| | 570 | HPO ₄ |
| | 950 | PO ₃ , POH |
| | 2800–3000 | NH ₄ |
| | 3000–3400 | OH, H ₂ O |

Table B5 List of atom bands detected and assigned using IR spectroscopy.

| Phase | Wavenumbers [cm ⁻¹] | Assignments |
|----------------------------------|---------------------------------|------------------------|
| | 470 | MgO or PO ₄ |
| | 1060, 1000, 940, 525 | PO ₄ |
| Struvite reacted at 60 °C for 24 | 1440 | NH ₄ |
| weeks | 1500 | HOH |
| | 2600–3300 | OH, H ₂ O |

Table B6 Results of Rietveld refinements of powder samples transformed in the open system at 22 °C.

| Time [weeks] | Suv [wt%] | New [wt%] | Dmr [wt%] | NH ₄ Cl [wt%] | wR | GOF | Durbin- Watson-Factor |
|-----------------|-----------|-----------|-----------|--------------------------|-------|------|--------------------------|
| 0.006 | 99.3 | 0.6 | 0 | 0.1 | 6.551 | 0.09 | 0.588 |
| 0.14 | 99.3 | 0.5 | 0 | 0.2 | 4.301 | 0.06 | 0.544 |
| 0.43 | 94.6 | 5.2 | 0 | 0.1 | 3.648 | 0.04 | 0.653 |
| 1 | 93.8 | 6.0 | 0 | 0.2 | 3.958 | 0.05 | 0.580 |
| 4 | 99.1 | 0.9 | 0 | 0 | 3.936 | 0.04 | 0.641 |
| 8 | 92.2 | 7.7 | 0 | 0.2 | 4.686 | 0.06 | 0.512 |
| 12 | 89.2 | 10.6 | 0 | 0.2 | 4.663 | 0.06 | 0.437 |
| 18 | 89.4 | 10.4 | 0 | 0.2 | 5.001 | 0.06 | 0.381 |
| 24 | 87.5 | 12.3 | 0 | 0.2 | 3.561 | 0.04 | 0.762 |
| 32 | 91.7 | 8.1 | 0 | 0.2 | 4.629 | 0.05 | 0.517 |
| 40 | 86.1 | 13.9 | 0 | 0 | 3.867 | 0.05 | 0.562 |

Table B7 Results of Rietveld refinements of powder samples transformed in the open system at 37 °C.

| Time [weeks] | Suv [wt%] | New [wt%] | Dmr [wt%] | NH ₄ Cl [wt%] | wR | GOF | Durbin- Watson-Factor |
|-----------------|-----------|-----------|-----------|--------------------------|-------|------|--------------------------|
| 0.006 | 0 | 0 | 0 | 0 | 4.683 | 0.07 | 0.469 |
| 0.14 | 99.8 | 0.2 | 0 | 0 | 3.677 | 0.05 | 0.503 |
| 0.43 | 99.8 | 0.2 | 0 | 0 | 4.867 | 0.06 | 0.461 |
| 1 | 99.4 | 0.6 | 0 | 0 | 6.059 | 0.08 | 0.470 |
| 4 | 94.6 | 5.3 | 0.1 | 0.1 | 4.544 | 0.06 | 0.542 |
| 12 | 65.2 | 4.5 | 30.3 | 0 | 4.147 | 0.06 | 0.405 |
| 24 | n.d. | n.d. | n.d. | n.d. | n.d. | n.d. | n.d. |
| 32 | 1.0 | 10.0 | 89.0 | 0 | 7.003 | 0.07 | 0.200 |
| 40 | 10.1 | 11.9 | 77.9 | 0 | 4.796 | 0.05 | 0.314 |

Table B8 Results of Rietveld refinements of powder samples transformed in the open system at 60 °C.

| Time [weeks] | Suv [wt%] | New [wt%] | Dmr [wt%] | NH ₄ Cl [wt%] | wR | GOF | Durbin- Watson-Factor |
|-----------------|-----------|-----------|-----------|--------------------------|-------|------|--------------------------|
| 0.006 | 99.7 | 0.3 | 0 | 0 | 4.579 | 0.07 | 0.480 |
| 0.10 | 99.2 | 0.6 | 0.1 | 0.1 | 5.245 | 0.06 | 0.405 |
| 0.12 | n.d. | n.d. | n.d. | n.d. | n.d. | n.d. | n.d. |
| 0.14 | 65.9 | 2.3 | 31.8 | 0 | 4.133 | 0.06 | 0.393 |
| 0.43 | 47.8 | 26.9 | 25.2 | 0 | 3.819 | 0.05 | 0.449 |
| 0.57 | n.d. | n.d. | n.d. | n.d. | n.d. | n.d. | n.d. |
| 0.71 | 18.1 | 3.9 | 78.0 | 0 | 4.170 | 0.05 | 0.521 |
| 1 | 0.7 | 4.5 | 94.6 | 0 | 6.441 | 0.08 | 0.276 |
| 2 | 0.1 | 5.3 | 94.5 | 0 | 5.043 | 0.06 | 0.330 |
| 4 | 0.5 | 5.5 | 94.0 | 0.1 | 6.714 | 0.08 | 0.242 |
| 8 | 0.5 | 3.1 | 96.4 | 0 | 5.527 | 0.06 | 0.281 |

Text B1: Description of data fitting to derive kinetic parameters using the JMAK equation.

From the logarithmic form of the Avrami equation, the rate constant k and the reaction order n were derived by plotting $-\ln[-\ln(1-\alpha)]$ against $\ln(t)$ and calculating the linear fits in the form of $\ln[-\ln(1-\alpha)] = n \cdot \ln(t) + \ln(k)$. The value of n is comprised of two components: β , which accounts for the “number of steps involved in nucleus formation”, and λ , which represents the “number of dimensions in which the nuclei grow” (Bamford and Tipper, 1980). The same authors suggested replacing $t-t_0$ with t as the induction time, which is defined as the time until the reaction starts and can only be partially determined with ex-situ diffraction data. This recommendation was followed for every linear fit except for the data derived for the reaction of struvite to dittmarite, as an induction time was observed for forming the latter phase.

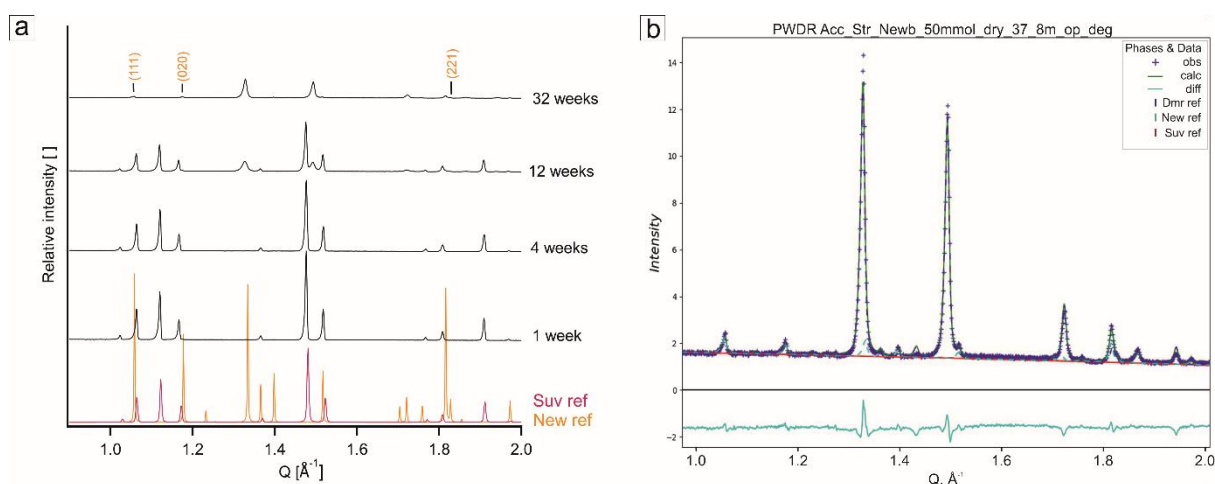


Fig. B1 a) Development of newberyite peaks in XRD patterns at 37°C. b) Computed partial phase contributions in the sample pattern of 37 °C, 32 weeks.

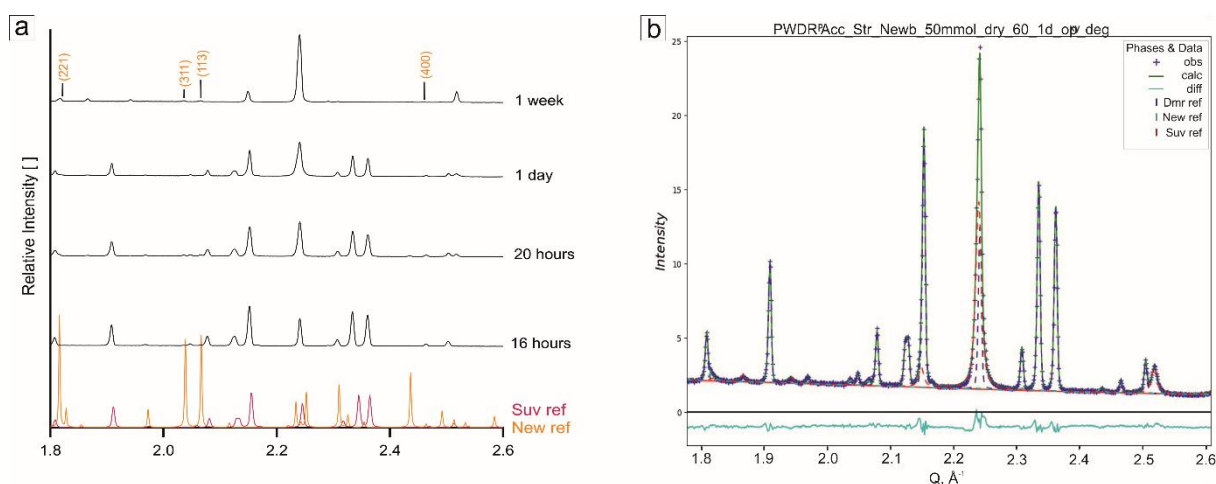


Fig. B2 a) Development of newberyite peaks in XRD patterns at 60 °C. b) Computed partial phase contributions in the sample pattern of 60 °C, 1 day.

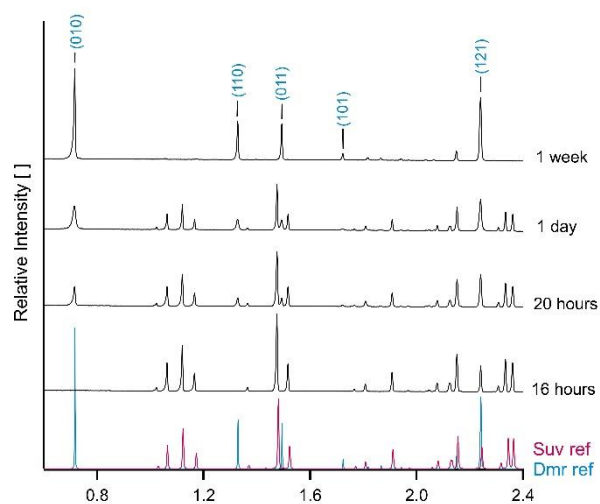


Fig. B3 a) Development of dittmarite peaks in XRD patterns at 60 °C.

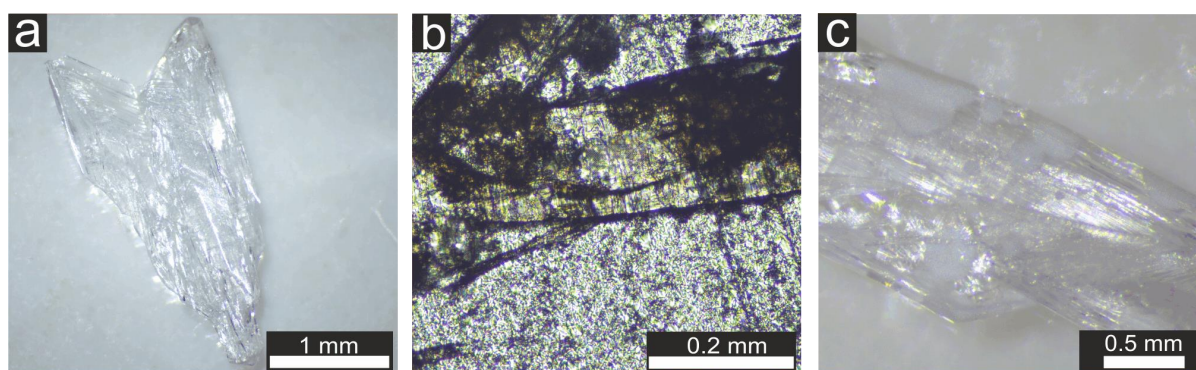


Fig. B4 a) Unaltered struvite crystal. b) 100 μm thin section of a struvite crystal altered at 22 °C for 12 weeks under LPL. c) Struvite crystal altered at 22 °C for 24 weeks.

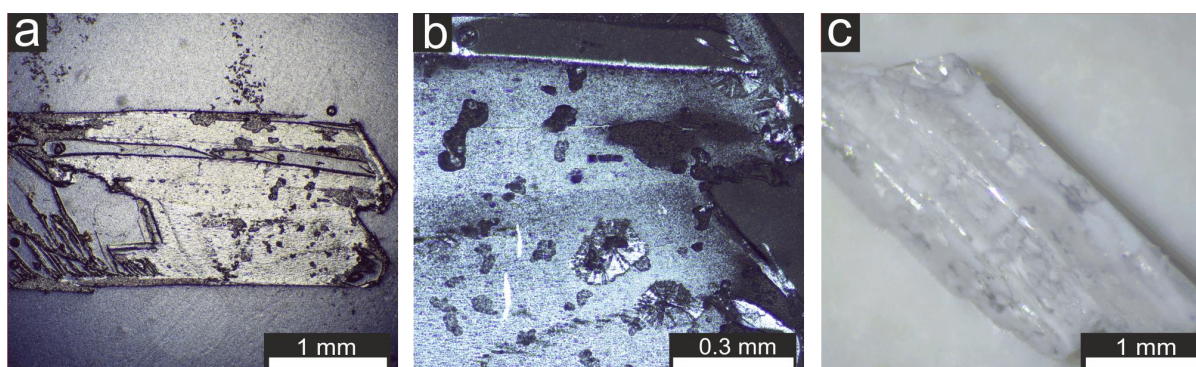


Fig. B5 a) 100 μm thin section of a struvite crystal altered at 37 °C for 4 weeks b) Close-up of a) under CPL showing radial crystals. c) Struvite crystal altered at 37 °C for 40 weeks.

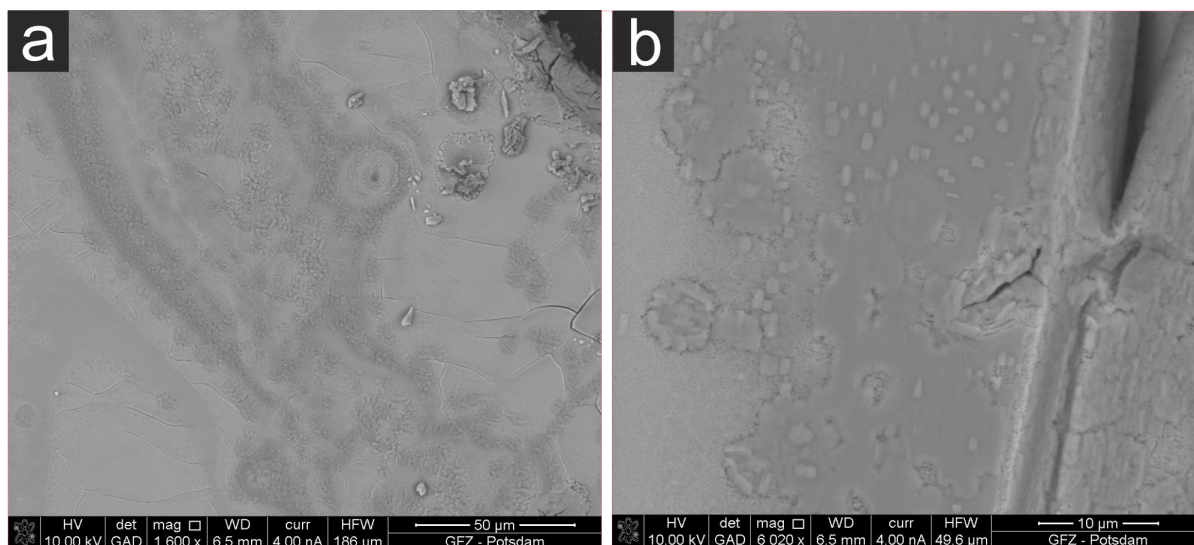


Fig. B6 a) SEM image of struvite crystal altered at 37 °C for 24 weeks showing transformation patterns in elemental contrast. b) SEM image of the same sample as in a) with rectangular patterns.

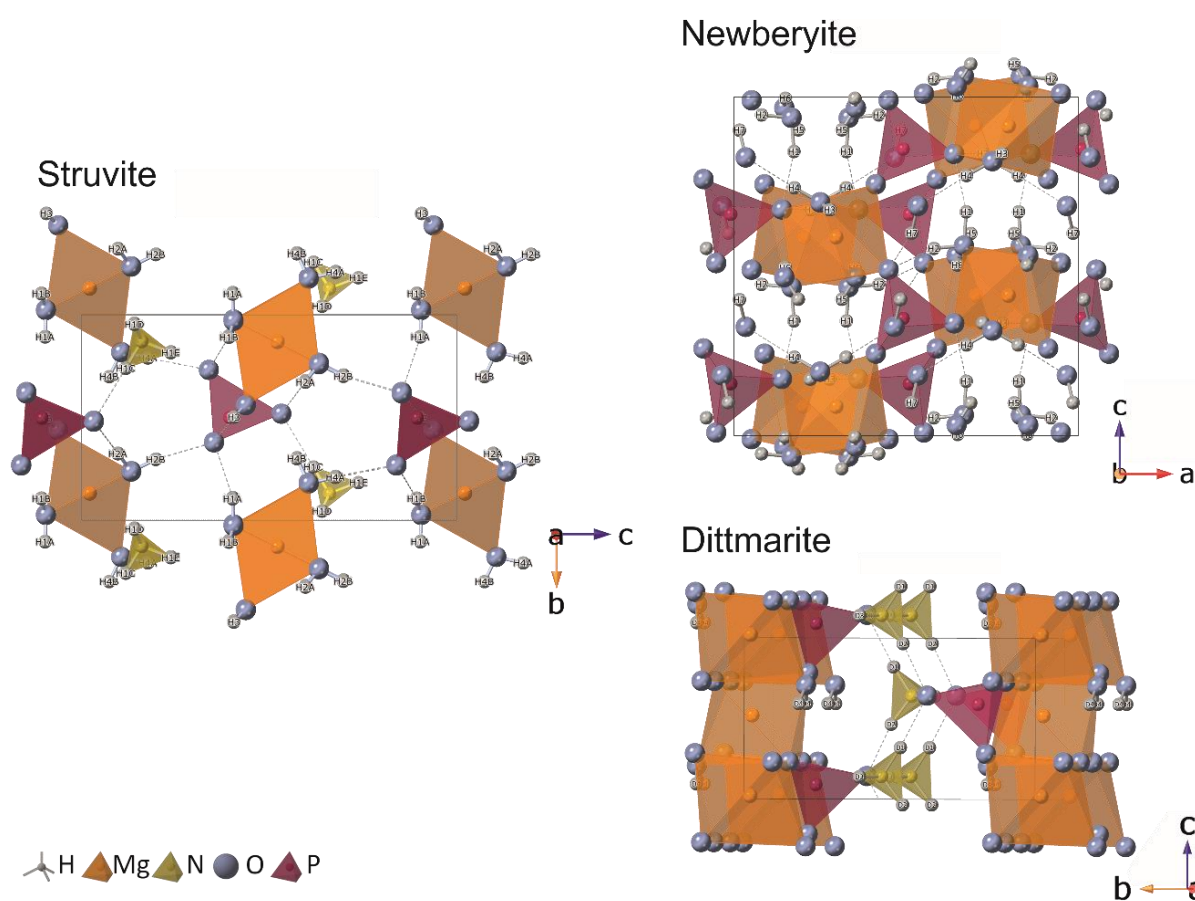


Fig. B7 Crystal-structural models of struvite ($Pmn2_1$) (Volkman et al., 2024), newberyite ($Pbca$) (Abbona et al., 1979) and dittmarite ($Pmn2_1$) (Frazier et al., 1966). Structure images were modelled from the corresponding CIF files using Crystal Maker (Palmer, 2014).

Appendix C List of publications and presentations

Manuscripts under review, submitted or in preparation

Volkman, R.; Blukis, R.; Benning, L.G. The temperature-dependence of nucleation and growth kinetics of the Mg phosphate mineral struvite. In preparation for submission to *European Journal of Mineralogy*.

Volkman, R.; Blukis, R.; Schmidt, C.; Forjanec, P.; Benning, L.G. The Transformation of Magnesium Phosphate Minerals at Atmospheric Conditions – A Kinetic and Mineralogical Study with Environmental Applications. submitted to *American Mineralogist*.

Publications in peer-reviewed journals

Schmitt, L; Kirnbauer, T.; Angerer, T.; **Volkman, R.;** Roddatis, V.; Wirth, R.; Klein, S. (2023) Genesis of Devonian volcanic-associated Lahn-Dill-type iron ores—part I: iron mobilisation and mineralisation style. *Mineralium Deposita*. <https://doi.org/10.1007/s00126-023-01218-3>

Data publications

Volkman, R.; Münchhalfen, M.; Benning, L.G. (2024). A new structure determination of the magnesium phosphate mineral struvite ($\text{MgNH}_4\text{PO}_4 \cdot 6\text{H}_2\text{O}$) at 100 K. *GFZ Data publication services*. <https://doi.org/10.5880/GFZ.3.5.2024.001>

Conference contributions

Volkman, R.; Blukis, R.; Schmidt, C.; Benning, L.G. Tracking transformation processes in the Mg phosphate mineral system. MinWien 2023, 18th–21st September 2023, oral presentation.

Volkman, R.; Blukis, R.; Schmidt, C.; Benning, L.G. Reactivity and Transformation Processes of Magnesium Phosphate Minerals. Helmholtz POF General Assembly 2023, 14th–16th May 2023, poster presentation.

Volkman, R.; Blukis, R.; Roddatis, V.; Schmidt, C.; Benning, L.G. Transformation Processes and Kinetics in the Magnesium Phosphate Mineral System. GeoMinKöln 2022, 12th–15th September 2022, poster presentation.

Appendix D List of awards and grants

09/2023

Paul-Ramdohr Award of 500 € given by the German Mineralogical Society for the best junior researcher contribution on the MinWien 2023 conference.

06/2022

Bursary Grant of CHF 500 given by the University of Zurich to participate in the Zurich School of Crystallography.

Appendix E Curriculum vitae

WORK EXPERIENCE

10/2020 – present

DOCTORAL CANDIDATE, Interface Geochemistry Section, GFZ German Research Centre for Geosciences Potsdam, Germany

Doctoral project in geochemistry and mineralogy about the magnesium phosphate mineral struvite. The thesis is divided into three sub-projects: (i) refinement of the crystal structure of struvite, (ii) defining the role of temperature in the nucleation and growth of struvite from aqueous solution, and (iii) understanding the temperature-related transformation kinetics of struvite to other magnesium phosphate minerals such as newberyite and dittmarite. Supervisor: Prof. Dr. Liane G. Benning

10/2017 – 10/2020

RESEARCH ASSISTANT (WHK), Department of Petrology and Geochemistry, Ruhr-University Bochum, Germany

Administration of the Petrology and Geochemistry Department website, tutor of various Bachelor's courses in the fields of chemistry, mineralogy and petrology, research assistance of Prof. Dr. Sumit Chakraborty

04/2017 – 10/2017

STUDENT ASSISTANT (SHK), Department of Petrology and Geochemistry, Ruhr-University Bochum, Germany

Administration of the Petrology and Geochemistry Department website, tutor of Bachelor's course in chemistry, research assistance of Prof. Dr. Sumit Chakraborty

EDUCATION

10/2017 – 10/2020

MASTER PROGRAM GEOSCIENCES majoring in petrology and geochemistry, Ruhr-University Bochum, Germany

Master of Science (05.10.2020) with final grade: 1,3

Master's thesis: „Carbonate minerals associated with the volcano-sedimentary iron-ores of the Lahn-Dill type: A petrographic, geochemical, and isotopic study“ (in English)

Supervisors: Prof. Dr. Sabine Klein, Prof. Dr. Thomas Kirnbauer

10/2013 - 09/2017

BACHELOR PROGRAM GEOSCIENCES, Ruhr-University Bochum, Germany

Bachelor of Science (25.09.2017) with final grade: 2,3

Bachelor's thesis: "Geochemie und Petrographie an Metapeliten der Buchan-Zone in Nordost-Schottland" (in German)

Supervisors: Dr. Thomas Fockenberger, Prof. Dr. Sumit Chakraborty

SCIENTIFIC COURSES AND TRAINING

04/2023 (3 days)

Stoe user & maintenance training, German GFZ Potsdam, Germany

Hands-on training for Stoe Stadi P diffractometer maintenance, supervision and usage

10/2022 (4 days)

Canadian Powder Diffraction Workshop, Online

Powder X-ray diffraction theory and exercises in Rietveld refinement

06/2022 (11 days)

Zurich School of Crystallography, University of Zurich, Switzerland

Passed certification in single crystal X-ray diffractometry and structure refinement

RESEARCH EXPERIENCE

12/2022 (7 days)

Funded Synchrotron Beamtime, Diamond Light Source, Didcot, UK

“Non-classical formation of vivianite and its role in Fe/P cycling in Neoproterozoic oceans” at the I22 Beamline

04/2016 - 03/2017 (1 year)

Interdisciplinary study project, Ruhr-University Bochum, Germany

Interdisciplinary study project including the fields of geosciences, biology and sociology: “Identity and nature consciousness of the island Helgoland”

INVITED TALKS

12.05.2023: MinPet Seminar, University of Potsdam, Germany

Talk: “Reactivity and Transformation Processes of the Phosphate Mineral Struvite”

PROFESSIONAL ENGAGEMENT

01/2023 – present

Co-founder of the Young Mineralogists (YoungMins) (sub-group of the German Mineralogical Society)

11/2021 – 11/2022

Doctoral students’ representative at the GFZ Potsdam

10/2021 – present

First-aid worker at the GFZ Potsdam

01/2018 – present

Member of the German Mineralogical Society